Electronic and Optical Properties of 2D Materials

Yasser Saleem

Supervisor: Prof. Pawel Hawrylak

Thesis submitted to
the University of Ottawa
in partial fulfilment of the requirements
for the Doctoral Degree in Physics

Department of Physics
Faculty of Sciences
University of Ottawa

Abstract

In this thesis, we contribute to the understanding of electronic and optical properties of 2-dimensional materials, with a strong focus on graphene-based nanostructures [1]. The thesis is structured into eight chapters, starting with an introduction and ending with a conclusion.

In chapter 2, we present the methods used throughout this thesis. We start by introducing the tight-binding model to understand the single-particle properties of graphene, bilayer graphene, and graphene quantum dots. We then introduce configuration interaction, the Hubbard model, the Bethe-Salpeter equation, and Hartree-Fock as tools for tackling the interacting problem and correlated electron systems. We also discuss numerical methods, including techniques for addressing the numerical complications that arise when working with the many-body problem such as the calculation of Coulomb matrix elements.

In chapter 3, we present a new approach to the energy spectra of p_z electrons in small hexagonal graphene quantum dots. This approach is analytical, and allows us to predict the dependence of the energy gap on size and edge type.

In chapter 4, we describe a proposal of a quantum simulator of an extended bipartite highly tunable Hubbard model with broken sublattice symmetry inspired by graphene. We predict the electronic and magnetic properties of a small simulator. The proposed simulator, allows us to study the ground state of the Hubbard Hamiltonian for a broad range of regimes accessible due to the high tunability of the simulator.

In chapter 5, we study the electronic properties of quasi 2-dimensional quantum dots made of topological insulators using HgTe. We show that in a square HgTe

quantum dot one set of material parameters defines the topologically nontrivial case, in which topologically protected edge states are found, and another set of parameters defines a topologically trivial regime corresponding to a trivial insulator without edge states.

In chapter 6, we examine excitons in AB-stacked gated bilayer graphene (BLG) quantum dots (QDs). We confine both electrons and holes using gates and demonstrate that excitons can exist in the BLG QD. We predict absorption to occur in the terahertz regime and find that low-energy excitons are dark.

In chapter 7, we determine the many-body states of massive Dirac Fermions confined in a bilayer graphene lateral gated quantum dot. Tuning the strength of Coulomb interactions versus the single-particle level spacing we predict the existence of spontaneously spin and valley symmetry-broken states of interacting massive Dirac Fermions.

Acknowledgements

I would like to thank Dr. Pawel Hawrylak for accepting me into his group and being more than just a supervisor, but also a friend throughout my PhD.

I would next like to thank my colleagues in my office, which was my second home during my PhD. A special thanks to Ludmila Szulakowska, who guided me early on during my PhD, as well as Eduard Dumitrescu for helping me with the numerical aspects of work early on when I was just beginning to learn. A special shoutout to Jake Manalo, who was almost following the same PhD trajectory as me, as we became close friends. It was nice to be able to talk about sports every once in a while with someone in the office.

To the younger students I mentored, Matthew Albert and Benjamin Puzantian, I know it's not always pleasant working with me, but I know you two can have a bright career in physics.

I would also like to thank the more advanced researchers in our group, the postdocs and collaborators in our group, mainly Dr. Moritz Cygorek and Dr. Alain Delgado Gran, and Dr. Marek Korkusinski. Their help and support when I was learning was much appreciated, and Mortiz became a good friend who I lost touch with because of the travels of a usual postdoc. They were always available to help.

I would like to thank my physics friends, Dilip, Ashish, Tuhin, Jake (again), Aldo, and probably the most important because of what we've been through, Jean-Luc Begin and Charlambos Kiolous. I spent my undergraduate degree with the former two, and wouldn't be here today if it wasn't for them. Especially Charms... you can be so hard to work with, but man you made me so much better at physics and math.

A special thanks to my friends Matt, Carmen, Mike, Aidan, Chad, Keith, Rusty, Katherine, Kyle, Bobbie, Justus. Being able to move away from work and hang out with friends, and to be able to get support from them if needed is always appreciated.

I would like to thank my family, my mom, my dad, and my three brothers for their support and friendship. I would not be who I am today if it wasn't for them.

I would also like to thank Katarzyna Sadecka who showed up as my biggest supporter in the last year of my PhD. The support she provided me during a very heavy year for me in 2022 meant alot. Infinity=Infinity.

Acronyms

1D	One-dimensional
2DES	two-dimensional electronic systems
2D	Two-dimensional
3D	Three-dimensional
CB	Conduction band
VB	Valence band
CI	Configuration interaction
DFT	Density functional theory
ATGQD	Artificial triangular graphene quantum dot
GQD	Graphene quantum dot
BLGQD	Bilayer Graphene quantum dot
BLG	Bilayer Graphene
GS	Ground state
HF	Hartree Fock
HO	Harmonic oscillator
NN	Nearest neighbor
NNN	Next nearest neighbor

QD	Quantum dot
TB	Tight-binding
VB	Valence band
AG	Artificial graphene
AF	Antiferromagnetic
BHZ	Bernevig-Hughes-Zhang
TI	Topological insulator
FIR	Far-infrared
TD-DFT	Time-dependent density functional theor

Contents

List of Figures

List of Tables

Chapter 1

Introduction

1.1 Graphene and bilayer graphene

Graphene is a two-dimensional (2D) material that is composed of a single layer of carbon atoms arranged in a hexagonal lattice. The hexagonal lattice can be described by two offset triangular sublattices: A, and B. A theoretical model of graphene was proposed in 1947 by P.R. Wallace at Chalk River NRC Laboratories. Wallace developed the first tight-binding description of graphene where he found graphene to be a semi-metal [2]. Furthermore, the low-energy electronic states of graphene are described by a massless Dirac equation [3–5]. The low-energy physics of graphene is fascinating due to the existence of two non-equivalent valleys, relativistic nature of quasiparticles, zero energy band gap, and sublattice pseudospin [2–4, 4–9].

Graphene was isolated and identified in 2004 by Andre Geim and Konstantin Novoselov [6], who were then working at the University of Manchester. The two scientists used a simple and elegant method to isolate a single layer of graphene from a chunk of graphite, which is a naturally-occurring form of carbon. The method they used involved placing a piece of scotch tape on a piece of graphite and then peeling it off. This process, which they repeated several times, allowed them to collect thin layers of graphene on the tape. They then transferred the graphene layers onto a silicon wafer, which allowed them to study their properties using optical and electronic methods.

Bilayer graphene (BLG) is a material that is composed of two layers of graphene stacked on top of each other. Bilayer graphene can be stacked in a variety of ways, depending on the orientation of the two layers relative to each other. The most common stacking configurations are called "AA" and "AB" stacking. In AA stacking, the two layers of graphene are aligned such that the carbon atoms in one layer are directly above the carbon atoms in the other layer. In AB stacking (also known as Bernal stacking), the two layers of graphene are not aligned in the same way. Instead, the carbon atoms in one layer are offset relative to the carbon atoms in the other layer such that the A atoms on one layer are stacked with the B atoms on the other layer. You can also stack and twist the layers relative to each. This is known as twisted bilayer graphene (TBLG).

There is currently significant interest in bilayer graphene (BLG) which has shown fascinating electrical and optical properties. While the low-energy electronic states of monolayer graphene are described by a massless Dirac Fermion model [3, 10–14], bilayer graphene can be described by massive chiral quasiparticles with parabolic dispersion at low energies [15–17]. It has been shown both theoretically and experimentally that BLG exhibits a continuously gate-tunable energy gap [17–26], allowing to study new physical effects originating from the gap-opening. Gate-tunable infrared phonon anomalies [27], gate-induced insulating state [28] or gate dependence of interband transitions [19] has been analyzed in the BLG systems. Moreover, BLG is characterized by a pseudospin winding number of 2 and a valley-dependent Berry phase with a magnitude of 2π [15–17, 29, 30], which provides a possibility to explore two-dimensional (2D) physics beyond conventional semiconductors. The possibility of opening the energy gap using an applied electric field caused high interest in the optical properties of BLG.

1.2 Quantum dots with a focus on graphene

A quantum dot is a small semiconductor structure that confines electrons in all three dimensions. The behavior of electrons and other particles within the quantum dot

is governed by the laws of quantum mechanics, rather than classical mechanics. As a result, quantum dots can exhibit unique electronic and optical properties, such as discrete energy levels and strong light-matter interactions [1].

Gate defined quantum dots in 2D materials have been studied intensively due to their potential of building quantum circuits using spin, valley or spin-valley states. The ability to confine carriers and manipulate their properties by tuning the size and shape of the system as well as the number of layers or the carrier density makes them a strong candidate for generating qubits [31–39]. This is because spin and valley states are robust to decoherence, and the tunability gives us control over the qubit. There is also a plethora of other applications such as lasers, transistors, and single and entangled photon sources as building blocks in quantum technologies [40–46].

There is currently significant interest in the electronic and optical properties of graphene quantum dots (GQDs) [1, 47–62]. Since graphene is a semi-metal [2–5, 7, 63], lateral size quantization opens up a gap inversely proportional to the size of the structure potentially allowing for the creation of a material with a continuously tunable bandgap with size that ranges from THz to UV.

Gated BLG QDs have been studied in recent years both experimentally and theoretically. It has been demonstrated that either electrons or holes can be confined in BLG QDs [31, 34]. Studies were carried out to understand the nature of the ground state as a function of the number of carriers, as well as understanding excited states in BLG QDs [31, 34–39, 64].

1.3 Artificial graphene

Artificial graphene (AG) is a material that is designed to mimic the properties of graphene. AG structures have been realized already using photonic lattices, nanopatterning, modulation doping, and scanning probe methods for atomic manipulation on metal surfaces [65–78]. Photonic lattices can be used to create AG by arranging nanoparticles in a periodic pattern, which can then be used to control the flow of light in a way that is similar to how graphene controls the flow of electrons. Similarly, nano-

patterning involves using lithography techniques to create patterns on the surface of a material. Overall, these techniques can be used to create materials with properties similar to graphene, which can be useful in a variety of applications.

There are several advantages of AG. These advantages include tunablity of the distance between the sites and depth of confining potential, programmable lattice symmetry and termination (i.e. edge type), tunable electron-electron interactions and interdot tunneling [69,75,76]. Further advantages of AG include the ability to control values of onsite Coulomb matrix element Hubbard U and tunnelling matrix element t and thus control the ratio U/t in a bipartite Hubbard model, which is not possible with graphene [79,80]. Such control would allow us to demonstrate different electronic phases, including transition from a semi-metallic phase to an antiferromagnetic insulator [81,82]. Additionally, triangular graphene quantum dots are susceptible to edge reconstruction as studied by Voznyy et. al. [83]. Edge reconstruction is responsible for smearing out the distinction between sublattices, and reduces the quantum dot symmetry. These combined features can destroy the magnetic properties of the system. The difficulty of edge reconstruction is overcome in an artificial system, where the edge is determined by the external gate. Another important advantage of AG is that, unlike in graphene, in AG a single electron can be placed in the system in order to probe the single-particle spectrum, directly demonstrating the existence of a zero energy shell and relating it to many-electron properties.

1.4 Thesis contributions.

I would like to emphasize that this thesis is heavily based on the papers I am listing below. Figures and content in this thesis are also contained in these papers which were constructed and generated during my PhD. I have, of course expanded and described the details and methods learned and used in order to generate the original results contained in these papers. The papers are listed as:

1. **Saleem, Y., Baldo, L. N., Delgado, A., Szulakowska L., Hawrylak, P.,**

Journal of Physics: Condensed Matter, 31(30), 305503 (2019)

"Oscillations of the Bandgap with Size in Armchair and Zigzag Graphene Quantum Dots" [84]

2. **Saleem, Y., Dusko, A., Cygorek, M., Korkusinski, M., Hawrylak, P. Physical Review B, 105(20), 205105 (2022)**

"Quantum Simulator of Extended Bipartite Hubbard Model with Broken Sublattice Symmetry: Magnetism, Correlations, and Phase Transitions" [85]

3. **Puzantian, B., Saleem, Y., Korkusinski, M., Hawrylak, P. Nanomaterials 2022, 12, 4283.**

"Edge States and Strain-Driven Topological Phase Transitions in Quantum Dots in Topological Insulators" [86]

4. **Korkusinski, M., Saleem, Y., Dusko, A., Miravet, D., Hawrylak, P., in preparation for Nature Physics (2023)**

"Spontaneous Spin and Valley Symmetry Broken States of Interacting Electrons in a Bilayer Graphene Quantum Dot"

5. **Saleem, Y., Sadecka, K., Korkusinski, M., Miravet, D., Dusko, A., Hawrylak, P., Nano Letters (2023)**

"Theory of Excitons in Gated Bilayer Graphene Quantum Dots" [87]

Throughout this thesis a lot of work was done in collaboration with coauthors in the above mentioned papers. I will try to make it clear at the beginning of each chapter which calculations are mine, and which calculations I did not perform.

1.5 Thesis outline.

This thesis is organized as follows: we begin with an introductory section (chapter 1) introducing motivation and current state of research in the field. Then chapter 2 focuses on various methodologies used in order to compute the electronic properties and optical properties of various 2D nanostructures.

Chapter 3 focuses on understanding the origin of the band gap for different size and edged hexagonal graphene quantum dots. We compare results with DFT and give insight into the opening of a gap in graphene due to finite size quantization.

In chapter 4 we introduce a triangular artificial graphene quantum dot (TAGQD), and develop a model to describe the single particle and many body properties of the system. We study the TAGQD for two different separations between sites, and show (at a mean field level) that there are two distinct phases that exist as a function of the ratio of onsite Coulomb matrix element called Hubbard U and the tunnelling matrix element t between nearest neighbour (NN) sites. We then include correlations to understand how they modify the properties of this ATGQD.

In Chapter 5 we discuss edge states in HgTe quantum dots. We focus on square and circular 2D geometries. We include strain in the calculations in order to control the topological phase of the HgTe QD. We find that for certain values of applied strain we can transition from a topologically trivial, to a topologically non-trivial system and as such we can transition from a system with edge states in the gap to a system without edge states.

In chapter 6 we study excitons in gated bilayer graphene quantum dots. This is done by constructing all one pair excitations from a fully occupied valence band and compute the excitonic spectrum. We then compute dipole matrix elements and absorption in order to see how our system responds to circulary polarized light.

Chapter 7 discusses the many body properties of gated BLG quantum dots containing N electrons. We begin with a tight-binding model for bulk BLG in the presence of an applied perpendicular electric field that is fitted to DFT calculations. Following this, we impose a confining potential in the center of our BLG sample in order to confine carriers and obtain SP confined states. We then include e-e interactions and discuss a rich phase diagram as a function of filling factor and strength of interactions.

Chapter 2

Methodology

In this chapter, we discuss the theoretical and numerical methods we have used throughout the thesis. Our focus is on three main topics: tight-binding (TB) model, many-body theory, and mean-field approximations.

The TB approach is a widely used method for studying the electronic properties of 2D materials, such as graphene. It can allow us to accurately model the behavior of electrons in a 2D system and calculate important properties such as the band structure.

The TB model ignores the effects of electron-electron interactions which play an important role in the electronic and optical properties of 2D systems and as such they must be included, and many-body calculations must be performed. This is done through configuration interaction (CI), or if we make an approximation of retaining only single electron-hole pair configurations, then we can solve the Bethe-Salpeter equation (BSE) instead.

Since the many-body Hamiltonian is difficult to solve, and sometimes exact diagonalization approaches cannot be implemented, we can use mean-field approximations such as Hartree-Fock to understand the role of interactions in determining the electronic and optical properties of 2D materials. In the later sections of this chapter, we will discuss the implementation of these theoretical methods using numerical techniques and their application to 2D materials.

2.1 Tight-binding model

The tight-binding model is a widely used approach for studying the electronic properties of materials, particularly those with a periodic or quasi-periodic structure. It is particularly well suited for studying the properties of graphene and other two-dimensional materials, as it can capture the essential physics of these systems while remaining computationally tractable.

One of the key advantages of the tight-binding model is its ability to accurately reproduce the band structure and density of states of a material, making it an important tool for understanding the electronic properties of graphene and other two-dimensional materials.

Let us consider the Hamiltonian for an electron moving in the potential of stationary atoms. The Hamiltonian can be written as

$$H = H_{at} + \Delta U, \tag{2.1}$$

where H_{at} is the Hamiltonian for a single atom and ΔU encodes the potential of the crystal minus the potential of the atom. We then consider the solution of a single isolated atom as

$$H_{at}\phi_\alpha = \epsilon_\alpha \phi_\alpha, \tag{2.2}$$

where ϵ_α is the energy of the orbital alpha in the isolated atom, and ϕ_α is the corresponding wavefunction. For the full crystal, we then expand our wavefunction as a linear combination of atomic orbitals centered at each atom i as

$$\psi_n = \sum_{i,\alpha} A^n_{i\alpha} \phi_\alpha \left(\vec{r} - \vec{R}_i\right). \tag{2.3}$$

In general this expansion in the basis of atomic orbitals is an expansion in a non-orthogonal basis. But, the idea is that the single atom solution has localized orbitals that decay rapidly away from the center of the atom and as such the overlap between atoms is small and so this basis is approximately orthogonal. To better understand

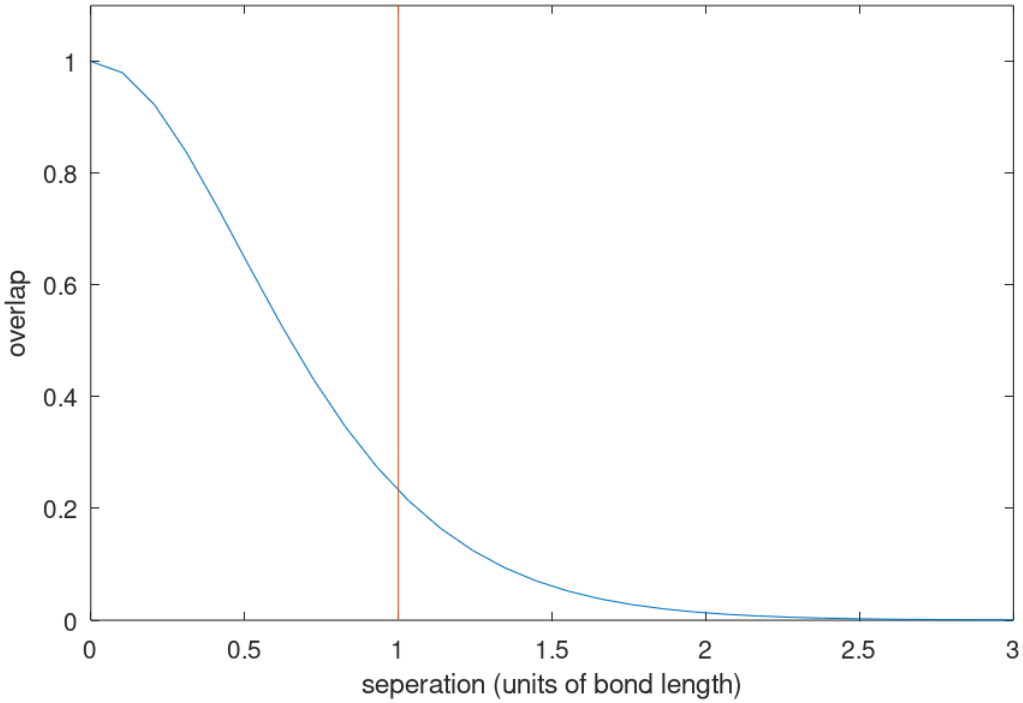

Figure 2.1: a) The overlap between p_z orbitals in carbon as a function of the separation between sites. The red line occurs at exactly the bond length

the overlap between two localized orbitals, let us use the example of p_z orbitals in graphene. The explicit form is given by [1]

$$\phi_i(\vec{r}) = \left(\frac{\xi^5}{32\pi}\right)^{\frac{1}{2}} (z - z_i)\, e^{-\frac{\xi}{2}|\vec{r}-\vec{r}_i|}, \tag{2.4}$$

where ξ is the Slater parameter which we take to be $\xi = 3.25$ [88] in units of bohrs and z is the coordinate out of plane of the graphene sheet, while z_i is the z coordinate of the carbon atom. The overlap between two of these orbitals is given by

$$S_{ij} = \int d\vec{r}\phi_i^*(\vec{r})\phi_j(\vec{r}) \tag{2.5}$$

Fig. 2.1 shows the overlap between two p_z orbitals as a function of the separation between sites i and j. The separation is in units of the bond length of graphene $a = 1.43$Å. We see a rapid decay in the overlap as the separation between sites grows. The red line shows the bond length in graphene. It is worth noting there are methods to orthogonalize the atomic orbitals for example using Wannier functions.

In the next few subsections, we will demonstrate the use of the TB model for graphene, bilayer graphene, and graphene quantum dots to give us a foundational understanding for the rest of the thesis.

2.1.1 Tight-binding model for bulk graphene

In this section, we describe the electronic properties of bulk graphene, following the famous paper by Wallace in 1946 [2].

Graphene is a single layer of carbon atoms arranged in a hexagonal lattice. For convenience, we orient the graphene sheet in the x-y plane, with the z-direction perpendicular to the sheet. The unit cell of the hexagonal lattice contains two carbon atoms, one belonging to the A sublattice and the other belonging to the B sublattice, as shown in Fig.2.2(a). The unit vectors $\vec{a}_1$ and $\vec{a}_2$ are given as

$$\vec{a}_1 = \left(0, \sqrt{3}a\right), \tag{2.6a}$$

$$\vec{a}_2 = \left(\frac{3a}{2}, \frac{-\sqrt{3}a}{2}\right), \tag{2.6b}$$

where $a = 1.43$Å is the nearest neighbour (NN) distance for graphene. The position of atoms A and B is given by

$$\vec{R}_A = n_1\vec{a}_1 + n_2\vec{a}_2, \tag{2.7a}$$

$$\vec{R}_B = n_1\vec{a}_1 + n_2\vec{a}_2 + \vec{b}, \tag{2.7b}$$

where n_1 and n_2 are integers and $\vec{b} = \left(\frac{1}{2}a, \frac{\sqrt{3}a}{2}\right)$ is shown in Fig. 2.2(a). We also have reciprocal lattice vectors as

$$\vec{b}_1 = \frac{2\pi}{a}\left(\frac{1}{3}, \frac{\sqrt{3}}{3}\right), \tag{2.8a}$$

$$\vec{b}_2 = \frac{2\pi}{a}\left(\frac{2}{3}, 0\right). \tag{2.8b}$$

Our Hamiltonian for a single electron moving in the potential of A and B carbon

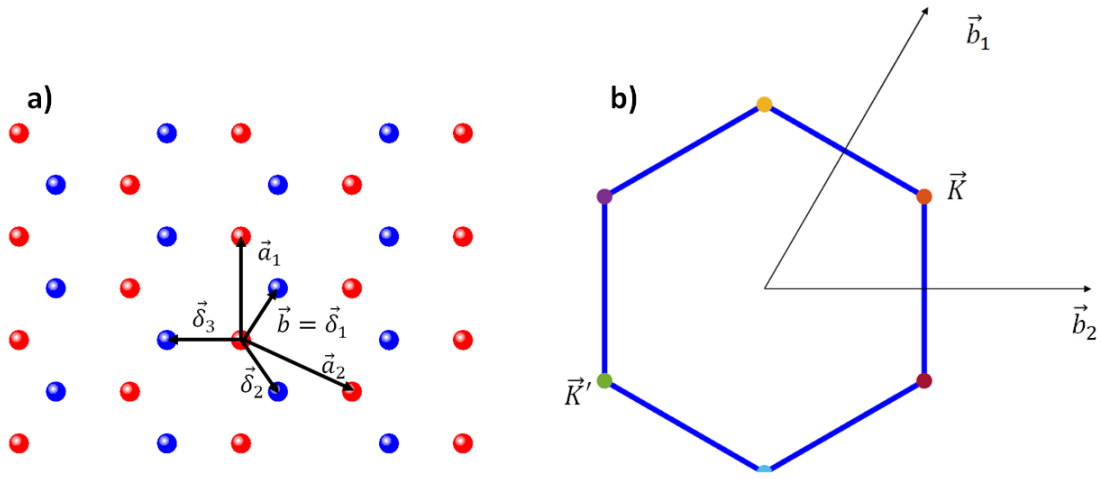

Figure 2.2: a) Geometric structure of graphene showing the A (red) and B (blue) atoms. The primitive lattice vectors $\vec{a}_1$, $\vec{a}_2$ are shown as well as the vectors $\vec{\delta}_1$, $\vec{\delta}_2$, $\vec{\delta}_3$ which connect atom A to its 3 NNs. b) Brillouin zone of graphene structure. The two inequivalent K points are labelled and the vectors $\vec{b}_1$, $\vec{b}_2$ are the reciprocal lattice vectors.

atoms is given by

$$\hat{H} = \frac{\hat{p}^2}{2m} + \sum_{\vec{R}_A} \hat{V}_A\left(\vec{r} - \vec{R}_A\right) + \sum_{\vec{R}_B} \hat{V}_B\left(\vec{r} - \vec{R}_B\right). \tag{2.9}$$

We apply the TB approximation to solve this Hamiltonian. As shown in Fig.2.2(a), each carbon atom in graphene has three nearest neighbors, and the $2s, 2p_x, 2p_y$ orbitals of these atoms hybridize to form sp^2 hybridized levels. This gives rise to strong σ bonds between the carbon atoms and determines the unique mechanical properties of graphene. The remaining p_z orbital, which is oriented out of the plane of the graphene sheet, forms π bonds and dominates the electronic and optical properties of graphene.

To account for the periodic nature of each graphene sublattice A and B, we expand the electron wavefunction as a linear combination of p_z orbitals localized on each sublattice A and B. This allows us to describe the behavior of electrons in the graphene lattice using the lattice vectors defined in Eq. 2.25. The wavefunctions explicitly are

given as

$$\psi_{\vec{k}}^{A}(\vec{r}) = \frac{1}{\sqrt{N}} \sum_{\vec{R}_A} e^{i\vec{k}\cdot\vec{R}_A} \phi_{p_z}\left(\vec{r} - \vec{R}_A\right), \tag{2.10a}$$

$$\psi_{\vec{k}}^{B}(\vec{r}) = \frac{1}{\sqrt{N}} \sum_{\vec{R}_B} e^{i\vec{k}\cdot\vec{R}_B} \phi_{p_z}\left(\vec{r} - \vec{R}_B\right), \tag{2.10b}$$

where N is the number of unit cells. Now our total wavefunction is

$$\psi_{\vec{k}}(\vec{r}) = A_{\vec{k}}\psi_{\vec{k}}^{A}(\vec{r}) + B_{\vec{k}}\psi_{\vec{k}}^{B}(\vec{r}), \tag{2.11}$$

where $A_{\vec{k}}$, $B_{\vec{k}}$ are expansion coefficients. We then proceed to solve the Schrödinger equation. Our Schrödinger equation is

$$\hat{H}\psi_{\vec{k}}(\vec{r}) = E_k\psi_{\vec{k}}(\vec{r}). \tag{2.12}$$

Using Eq. 2.9 and Eq. 2.11 we have

$$\hat{H}\left[A_{\vec{k}}\psi_{\vec{k}}^{A}(\vec{r}) + B_{\vec{k}}\psi_{\vec{k}}^{B}(\vec{r})\right] = E_k\left[A_{\vec{k}}\psi_{\vec{k}}^{A}(\vec{r}) + B_{\vec{k}}\psi_{\vec{k}}^{B}(\vec{r})\right]. \tag{2.13}$$

Multiplying by $\left(\psi_{\vec{k}}^{A}(\vec{r})\right)^*$ and integrating over all of space we have

$$A_{\vec{k}}\left\langle\psi_{\vec{k}}^{A}\right|\hat{H}\left|\psi_{\vec{k}}^{A}\right\rangle + B_{\vec{k}}\left\langle\psi_{\vec{k}}^{A}\right|\hat{H}\left|\psi_{\vec{k}}^{B}\right\rangle = E_k\left[\langle\psi_{\vec{k}}^{A}|\psi_{\vec{k}}^{A}\rangle + \langle\psi_{\vec{k}}^{A}|\psi_{\vec{k}}^{B}\rangle\right]. \tag{2.14}$$

Assuming no overlap between $\psi_{\vec{k}}^{A}$ and $\psi_{\vec{k}}^{B}$ we have

$$A_{\vec{k}}\left\langle\psi_{\vec{k}}^{A}\right|\hat{H}\left|\psi_{\vec{k}}^{A}\right\rangle + B_{\vec{k}}\left\langle\psi_{\vec{k}}^{A}\right|\hat{H}\left|\psi_{\vec{k}}^{B}\right\rangle = E_k. \tag{2.15}$$

Now projecting $\left(\psi_{\vec{k}}^{B}(\vec{r})\right)^*$ and following the same procedure we have

$$A_{\vec{k}}\left\langle\psi_{\vec{k}}^{B}\right|\hat{H}\left|\psi_{\vec{k}}^{A}\right\rangle + B_{\vec{k}}\left\langle\psi_{\vec{k}}^{B}\right|\hat{H}\left|\psi_{\vec{k}}^{B}\right\rangle = E_k. \tag{2.16}$$

Eq. 2.15 and Eq. 2.16 give a system of equations which, in matrix form, can be written

as

$$\begin{pmatrix} \langle\psi^A_{\vec{k}}|\,\hat{H}\,|\psi^A_{\vec{k}}\rangle & \langle\psi^A_{\vec{k}}|\,\hat{H}\,|\psi^B_{\vec{k}}\rangle \\ \langle\psi^B_{\vec{k}}|\,\hat{H}\,|\psi^A_{\vec{k}}\rangle & \langle\psi^B_{\vec{k}}|\,\hat{H}\,|\psi^B_{\vec{k}}\rangle\,. \end{pmatrix} \begin{pmatrix} A_{\vec{k}} \\ B_{\vec{k}} \end{pmatrix} = E_{\vec{k}} \begin{pmatrix} A_{\vec{k}} \\ B_{\vec{k}} \end{pmatrix} \tag{2.17}$$

We now proceed to compute a diagonal matrix element:

$$\begin{aligned} \langle\psi^A_{\vec{k}}|\,\hat{H}\,|\psi^A_{\vec{k}}\rangle &= \langle\psi^A_{\vec{k}}|\,\frac{\hat{p}^2}{2m} + \sum_{\vec{R}_A}\hat{V}_A\left(\vec{r}-\vec{R}_A\right) + \sum_{\vec{R}_B}\hat{V}_B\left(\vec{r}-\vec{R}_B\right)|\psi^A_{\vec{k}}\rangle \\ &= \langle\psi^A_{\vec{k}}|\,\frac{\hat{p}^2}{2m} + \sum_{\vec{R}_A}\hat{V}_A\left(\vec{r}-\vec{R}_A\right)|\psi^A_{\vec{k}}\rangle + \langle\psi^A_{\vec{k}}|\sum_{\vec{R}_B}\hat{V}_B\left(\vec{r}-\vec{R}_B\right)|\psi^A_{\vec{k}}\rangle\,. \end{aligned} \tag{2.18}$$

The second term $\langle\psi^A_{\vec{k}}|\sum_{\vec{R}_B}\hat{V}_B\left(\vec{r}-\vec{R}_B\right)|\psi^A_{\vec{k}}\rangle$ can be expanded and corresponds to a combination of three-center integrals, and integrals which correspond to an electron on sublattice A feeling the potential of all B sublattice potentials. A three-center integral is the overlap integral between three atomic orbitals, typically involving two hydrogen atoms and a central atom in a molecule. Both of these are assumed small and are neglected. The first term $\langle\psi^A_{\vec{k}}|\,\frac{\hat{p}^2}{2m}+\sum_{\vec{R}_A}\hat{V}_A\left(\vec{r}-\vec{R}_A\right)|\psi^A_{\vec{k}}\rangle = \epsilon_A$, we set equal to a constant. This leaves us with

$$\langle\psi^A_{\vec{k}}|\,\hat{H}\,|\psi^A_{\vec{k}}\rangle = \langle\psi^B_{\vec{k}}|\,\hat{H}\,|\psi^B_{\vec{k}}\rangle = \epsilon_A = \epsilon. \tag{2.19}$$

Now computing the off-diagonal element $\langle\psi^A_{\vec{k}}|\,\hat{H}\,|\psi^B_{\vec{k}}\rangle$ we have

$$\begin{aligned} \langle\psi^A_{\vec{k}}|\,\hat{H}\,|\psi^B_{\vec{k}}\rangle &= \langle\psi^A_{\vec{k}}|\,\frac{\hat{p}^2}{2m} + \sum_{\vec{R}_A}\hat{V}_A\left(\vec{r}-\vec{R}_A\right)|\psi^B_{\vec{k}}\rangle + \langle\psi^A_{\vec{k}}|\sum_{\vec{R}_B}\hat{V}_B\left(\vec{r}-\vec{R}_B\right)|\psi^B_{\vec{k}}\rangle \\ &= \epsilon\,\langle\psi^A_{\vec{k}}|\psi^B_{\vec{k}}\rangle + \langle\psi^A_{\vec{k}}|\sum_{\vec{R}_B}\hat{V}_B\left(\vec{r}-\vec{R}_B\right)|\psi^B_{\vec{k}}\rangle \\ &= \frac{1}{N}\sum_{<\vec{R}_B,\vec{R}_A>} e^{i\vec{k}\cdot(\vec{R}_B-\vec{R}_A)}\,\langle\phi_{p_z}\left(\vec{r}-\vec{R}_A\right)|\,\hat{V}_B\left(\vec{r}-\vec{R}_B\right)|\phi_{p_z}\left(\vec{r}-\vec{R}_B\right)\rangle \\ &= t\left(e^{i\vec{k}\cdot\vec{\delta}_1}+e^{i\vec{k}\cdot\vec{\delta}_2}+e^{i\vec{k}\cdot\vec{\delta}_3}\right), \end{aligned} \tag{2.20}$$

where we have again ignored three-center integrals, and $t = \langle\psi^A_{\vec{k}}|\sum_{\vec{R}_B}\hat{V}_B\left(\vec{r}-\vec{R}_B\right)|\psi^B_{\vec{k}}\rangle$

is the hopping integral. $\vec{\delta}_1$, $\vec{\delta}_2$, $\vec{\delta}_3$ are vectors connecting a carbon atom to its 3 NNs as shown in Fig. 2.2(a). They are given explicitly by

$$\vec{\delta}_1 = \vec{b}, \tag{2.21a}$$

$$\vec{\delta}_2 = \vec{b} - \vec{a}_1, \tag{2.21b}$$

$$\vec{\delta}_3 = \vec{b} - \vec{a}_2. \tag{2.21c}$$

We can now define $f(\vec{k}) = e^{i\vec{k}\cdot\vec{\delta}_1} + e^{i\vec{k}\cdot\vec{\delta}_2} + e^{i\vec{k}\cdot\vec{\delta}_3}$ and set $\epsilon = 0$ since, this corresponds only to an overall shift in energy. So, Eq. 2.17 becomes

$$\begin{pmatrix} 0 & tf(\vec{k}) \\ tf^*(\vec{k}) & 0 \end{pmatrix} \begin{pmatrix} A_{\vec{k}} \\ B_{\vec{k}} \end{pmatrix} = E_{\vec{k}} \begin{pmatrix} A_{\vec{k}} \\ B_{\vec{k}} \end{pmatrix}. \tag{2.22}$$

Diagonalizing this Hamiltonian we get energies

$$E^{\pm}_{\vec{k}} = \pm t|f(\vec{k})|, \tag{2.23}$$

and eigenvectors for the energies $E^{\pm}_{\vec{k}}$ are given by

$$\begin{pmatrix} A_{\vec{k}} \\ B_{\vec{k}} \end{pmatrix} = \begin{pmatrix} 1 \\ \pm e^{-i\theta_{\vec{k}}}. \end{pmatrix}, \tag{2.24}$$

where $e^{i\theta_{\vec{k}}} = \frac{f(\vec{k})}{|f(\vec{k})|}$. Fig.2.3 shows the band structure of graphene. Notice that at special points, the gap between the valence band and conduction band closes. This indicates that graphene is a semimetal. The closing of the gap occurs at the $\vec{K}$ and $\vec{K}'$ (shown in Fig. 2.2(b)) points in the Brillouin zone. We now proceed to analyze the dispersion around where $E^{\pm} = 0$, in other words where $f(\vec{k}) = 0$. With some simple algebra one finds that

$$\vec{K} = \left(0, -\tfrac{4\pi}{3\sqrt{3}a}\right), \tag{2.25a}$$

$$\vec{K}' = \left(0, \tfrac{4\pi}{3\sqrt{3}a}\right), \tag{2.25b}$$

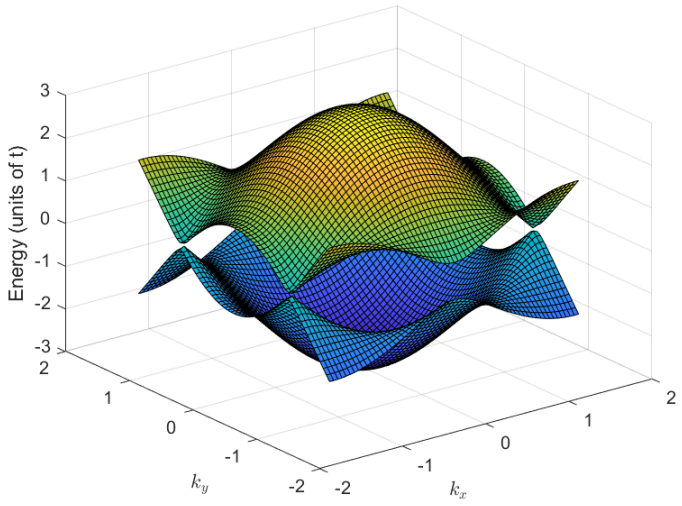

Figure 2.3: Graphene band structure in the NN approximation with energy measured in units of the hopping element t. At special points the gap between the valence band and conduction band closes.

Now let us Taylor expand our Hamiltonian defined in Eq. 2.22 around $\vec{K}$ by expanding $f(\vec{k})$ as

$$\begin{aligned}
f(\vec{K}+\vec{q}) &\approx f(\vec{K}) + f'(\vec{K})\cdot\vec{q} = f'(\vec{K})\cdot\vec{q} \\
&= i\vec{q}\cdot\vec{\delta}_1 e^{i\vec{K}\cdot\vec{\delta}_1} + i\vec{q}\cdot\vec{\delta}_2 e^{i\vec{K}\cdot\vec{\delta}_2} + i\vec{q}\cdot\vec{\delta}_3 e^{i\vec{K}\cdot\vec{\delta}_3} \\
&= i\vec{q}\cdot\vec{b}e^{i\vec{K}\cdot\vec{b}} + i\vec{q}\cdot(\vec{b}-\vec{a}_1)e^{i\vec{K}\cdot(\vec{b}-\vec{a}_1)} + i\vec{q}\cdot(\vec{b}-\vec{a}_2)e^{i\vec{K}\cdot(\vec{b}-\vec{a}_2)} \\
&= i\vec{q}\cdot\vec{b}\left(-\frac{1}{2}+\frac{\sqrt{3}}{2}i\right) + i\vec{q}\cdot(\vec{b}-\vec{a}_1)\left(-\frac{1}{2}-\frac{\sqrt{3}}{2}i\right) + i\vec{q}\cdot(\vec{b}-\vec{a}_2) \\
&= -\frac{1}{2}i\vec{q}\cdot(2\vec{b}-\vec{a}_1) - \frac{\sqrt{3}}{2}\vec{q}\cdot\vec{a}_1 + i\vec{q}\cdot(\vec{b}-\vec{a}_2) \\
&= -\frac{1}{2}iq_x a - \frac{3}{2}q_y a - iq_x a \\
&= -\frac{3}{2}a\left(q_y + iq_x\right),
\end{aligned} \tag{2.26}$$

where we have used the fact that $f(\vec{K}) = 0$ and retained only linear terms of $\vec{q}$ in the expansion. Now if we interchange q_x and q_y by relabelling the axis, we have

$$f(\vec{K}+\vec{q}) \approx -\frac{3a}{2}\left(q_x + iq_y\right), \tag{2.27}$$

which is in agreement with Refs. 1, 10, 89, 90. So we can write the Hamiltonian in

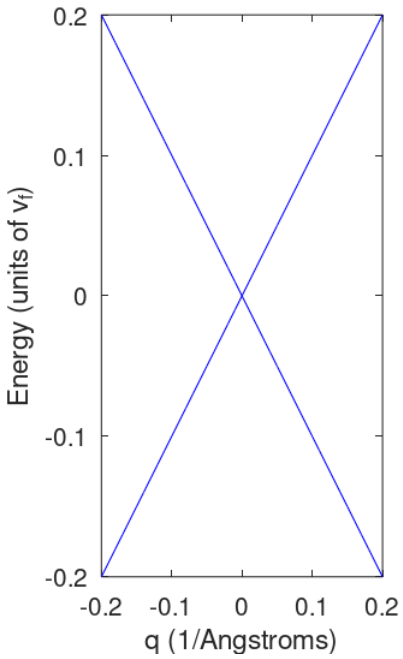

Figure 2.4: Graphene dispersion around $\vec{K}$ point in the NN approximation.

Eq. 2.22 around the $\vec{K}$ point that lies along the y-direction as

$$\mathbf{H}(q) = \frac{3ta}{2}\begin{pmatrix} 0 & (-q_x - iq_y) \\ (-q_x + iq_y) & 0 \end{pmatrix}. \tag{2.28}$$

We note that this Hamiltonian mimics that of a massless Dirac Fermion Hamiltonian, it can be written as $\mathbf{H}(q) = -v_f\vec{\sigma}^* \cdot \vec{q}$, where $v_f = \frac{3ta}{2}$. Where $\vec{\sigma}$ are the Pauli spin matrices. Note in the other valley, this Hamiltonian doesn't contain the conjugation on the Pauli spin matrices. Diagonalizing this Hamiltonian we get

$$E^{\pm}_{\vec{q}} = \pm v_f|\vec{q}|. \tag{2.29}$$

Figure. 2.4 shows the energy around the $\vec{K}$ point. We observe linear dispersion which is characteristic of massless Dirac Fermions.

2.1.2 Tight-binding model for bulk bilayer graphene

In this section we expand what we learned in the previous section on graphene by studying BLG. The idea here is we have solved the problem for an individual layer of bulk graphene, and we can now consider two layers, and turn on coupling between the layers to understand the band structure of BLG. There are a number of ways to stack the layers, such as AA stacked layers, where the layers are perfectly aligned, or Bernal stacked (AB-stacked) as seen in Fig. 2.5. The AB stacking is more energetically favorable compared to AA stacking, and is the focus of this section. One can also twist one layer with respect to another leading to moire patterns [91–96] which is a topic of further research beyond what is shown in this thesis. We will show that for bulk Bernal stacked BLG the dispersion is parabolic and gapless, but the application of a perpendicular electric field opens the gap in BLG.

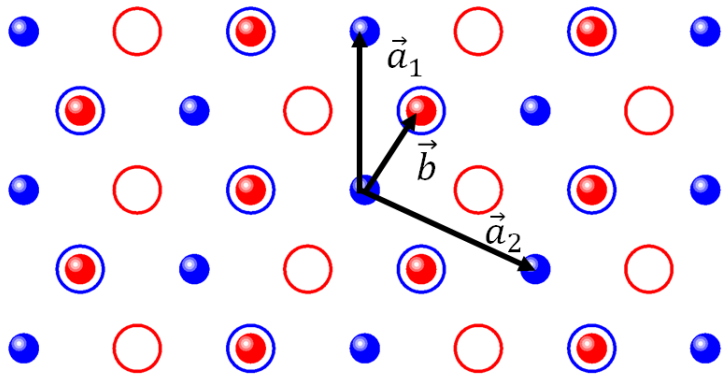

Figure 2.5: BLG AB-stacked geometry where the upper layer (layer 1) is denoted with solid balls, while the lower layer (layer 2) are the open circles. Blue corresponds to sublattice A, while red corresponds to sublattice B.

We start with our Hamiltonian for bulk BLG given by

$$\hat{H} = \frac{\hat{p}^2}{2m} + \sum_{\vec{R}_{A1}} \hat{V}_{A1}\left(\vec{r} - \vec{R}_{A1}\right) + \sum_{\vec{R}_{B1}} \hat{V}_{B1}\left(\vec{r} - \vec{R}_{B1}\right) + \sum_{\vec{R}_{A2}} \hat{V}_{A2}\left(\vec{r} - \vec{R}_{A2}\right) + \sum_{\vec{R}_{B2}} \hat{V}_{B2}\left(\vec{r} - \vec{R}_{B2}\right), \tag{2.30}$$

where $A1$, $B1$, $A2$, $B2$ correspond to sublattices A and B for layers 1 and 2 respectively, and are shown in Fig. 2.5. We can then expand our wavefunction similar to

Eq. 2.11 but including the fact that we have sublattices from both layers and we have

$$\psi_{\vec{k}}(\vec{r}) = A_{1\vec{k}}\psi_{\vec{k}}^{A1}(\vec{r}) + B_{1\vec{k}}\psi_{\vec{k}}^{B1}(\vec{r}) + A_{2\vec{k}}\psi_{\vec{k}}^{A2}(\vec{r}) + B_{2\vec{k}}\psi_{\vec{k}}^{B2}(\vec{r}). \tag{2.31}$$

Now following the same procedure as outlined for a single layer we can write our Hamiltonian in the basis of sublattices $A1, B1, A2, B2$ as [17]

$$\mathbf{H}(\vec{k}) = \begin{pmatrix} 0 & \gamma_0 f\left(\vec{k}\right) & \gamma_4 f\left(\vec{k}\right) & -\gamma_3 f^*\left(\vec{k}\right) \\ \gamma_0 f^*\left(\vec{k}\right) & 0 & \gamma_1 & \gamma_4 f\left(\vec{k}\right) \\ \gamma_4 f^*\left(\vec{k}\right) & \gamma_1 & 0 & \gamma_0 f\left(\vec{k}\right) \\ -\gamma_3 f^*\left(\vec{k}\right) & \gamma_4 f^*\left(\vec{k}\right) & \gamma_0 f^*\left(\vec{k}\right) & 0 \end{pmatrix}, \tag{2.32}$$

where $\gamma_0 = t$ is the intralayer NN hopping, $\gamma_1 = \langle \psi_{\vec{k}}^{B1} | \hat{H} | \psi_{\vec{k}}^{A2} \rangle$ is the interlayer hopping between sublattice B1 and sublattice A2 stacked directly on top of each other as seen in Fig. 2.5. γ_3 is the hopping from sublattice A1 to B2 and is known as the trigonal warping term, and γ_4 is the hopping from sublattice A1 to A2 or B1 to B2. For simplicity, we ignore γ_3, γ_4, further discussion of γ_3 will arise in chapter 7. The Hamiltonian ignoring these terms is then

$$\mathbf{H}(\vec{k}) = \begin{pmatrix} 0 & \gamma_0 f\left(\vec{k}\right) & 0 & 0 \\ \gamma_0 f^*\left(\vec{k}\right) & 0 & \gamma_1 & 0 \\ 0 & \gamma_1 & 0 & \gamma_0 f\left(\vec{k}\right) \\ 0 & 0 & \gamma_0 f^*\left(\vec{k}\right) & 0 \end{pmatrix}, \tag{2.33}$$

Diagonalizing Eq. 2.33 we get

$$E\left(\vec{k}\right) = \pm\frac{1}{\sqrt{2}}\sqrt{2\gamma_0^2\left|f\left(\vec{k}\right)\right|^2 + \gamma_1^2 \pm \sqrt{\left(2\gamma_0^2\left|f\left(\vec{k}\right)\right|^2 + \gamma_1^2\right)^2 - 4\gamma_0^4\left|f\left(\vec{k}\right)\right|^4}}. \tag{2.34}$$

Figure. 2.6 shows the band structure of bilayer graphene. We observe a zero band gap at the $\vec{K}$ points similar to graphene but with a different dispersion. This zero band gap makes bulk BLG a semimetal. We now proceed to study the low-energy

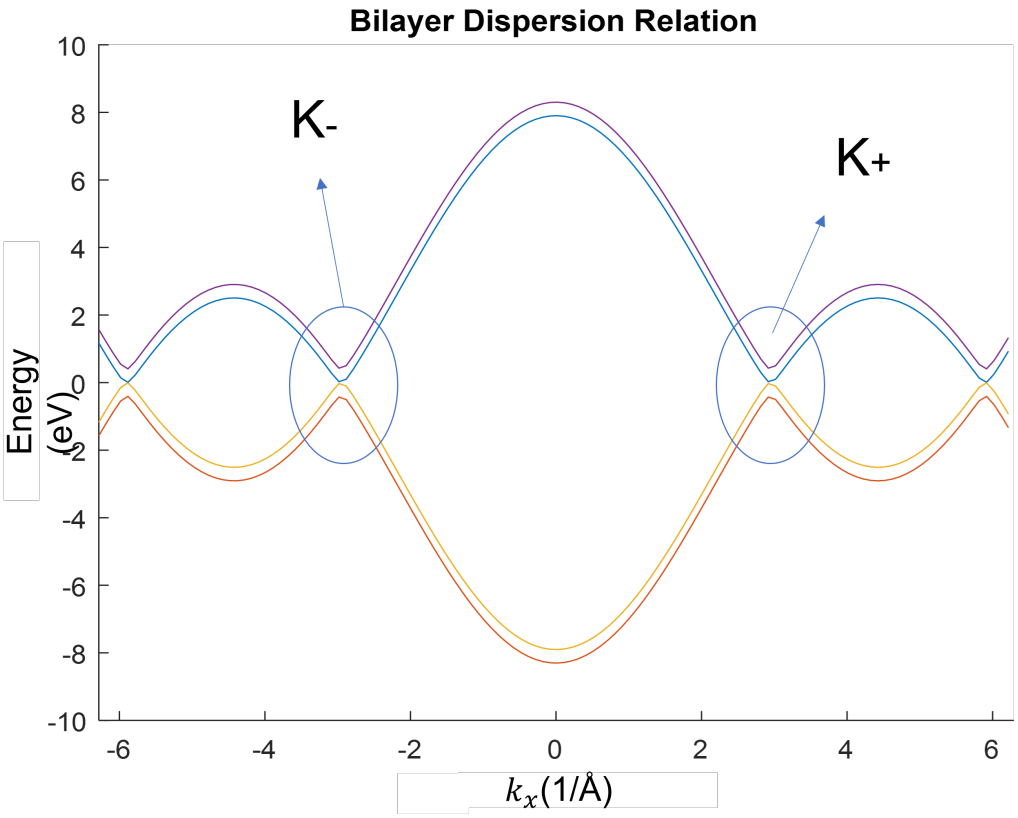

Figure 2.6: Band structure for bulk BLG. At the K-points the gap closes making bilayer graphene a semimetal.

dispersion around the $\vec{K}$ points as we did in the previous section for a single layer. Expanding our function $f\left(\vec{k}\right)$ around the $\vec{K}$ point using Eq. 2.27 transforms our Hamiltonian to

$$\mathbf{H}(\vec{q}) = \begin{pmatrix} 0 & v_f\left(-q_x - iq_y\right) & 0 & 0 \\ v_f\left(-q_x + iq_y\right) & 0 & \gamma_1 & 0 \\ 0 & \gamma_1 & 0 & v_f\left(-q_x - iq_y\right) \\ 0 & 0 & v_f\left(-q_x + iq_y\right) & 0 \end{pmatrix}, \quad (2.35)$$

where we used our previous definition of the Fermi velocity $v_f = \frac{3\gamma_0 a}{2}$. We can simplify this Hamiltonian to make it easier to diagonalize. Let's start by reorganizing the basis

as B1, A2, B2, A1 and we get

$$\mathbf{H}(\vec{q}) = \begin{pmatrix} 0 & \gamma_1 & 0 & v_f\left(-q_x + iq_y\right) \\ \gamma_1 & 0 & v_f\left(-q_x - iq_y\right) & 0 \\ 0 & v_f\left(-q_x + iq_y\right) & 0 & 0 \\ v_f\left(-q_x - iq_y\right) & 0 & 0 & 0 \end{pmatrix}. \quad (2.36)$$

Now define the following

$$\mathbf{V} = \begin{pmatrix} 0 & \gamma_1 \\ \gamma_1 & 0 \end{pmatrix}, \quad (2.37)$$

$$\mathbf{h} = \begin{pmatrix} 0 & v_f\left(-q_x + iq_y\right) \\ v_f\left(-q_x - iq_y\right) & 0 \end{pmatrix}, \quad (2.38)$$

$$\theta = \begin{pmatrix} B_{1\vec{k}} \\ A_{2\vec{k}} \end{pmatrix}, \quad (2.39)$$

$$\chi = \begin{pmatrix} B_{2\vec{k}} \\ A_{1\vec{k}} \end{pmatrix}, \quad (2.40)$$

we can then write our Schrödinger equation as

$$\begin{pmatrix} \mathbf{V} & \mathbf{h} \\ \mathbf{h} & \mathbf{0} \end{pmatrix} \begin{pmatrix} \theta \\ \chi \end{pmatrix} = E \begin{pmatrix} \theta \\ \chi \end{pmatrix}, \quad (2.41)$$

where $\mathbf{0}$ is a 2x2 block of zeros. Expanding this yields two equations

$$\mathbf{V}\theta + \mathbf{h}\chi = E\theta, \quad (2.42a)$$

$$\mathbf{h}\theta = E\chi. \quad (2.42b)$$

Replacing χ in the first equation by using the second and multiplying by E we get

$$E\mathbf{V}\theta + \mathbf{h}\mathbf{h}\theta = E^2\theta. \quad (2.43)$$

Since we only focus on the low-energy states we ignore the term of order E^2 and we can obtain a Schrödinger like equation of the form

$$E\theta = \mathbf{H_{eff}}\theta. \tag{2.44}$$

where $\mathbf{H_{eff}} = -\mathbf{V}^{-1}\mathbf{hh}$. Inverting $\mathbf{V}$ and multiplying matrices we obtain

$$\mathbf{H_{eff}} = -v_f^2 \begin{pmatrix} 0 & \frac{|\vec{q}|^2}{\gamma_1} \\ \frac{|\vec{q}|^2}{\gamma_1} & 0 \end{pmatrix}. \tag{2.45}$$

Diagonalizing this matrix we obtain our energies

$$E\left(\vec{q}\right) = \pm\frac{v_f^2}{\gamma_1}\left|\vec{q}\right|^2, \tag{2.46}$$

and the eigenvectors

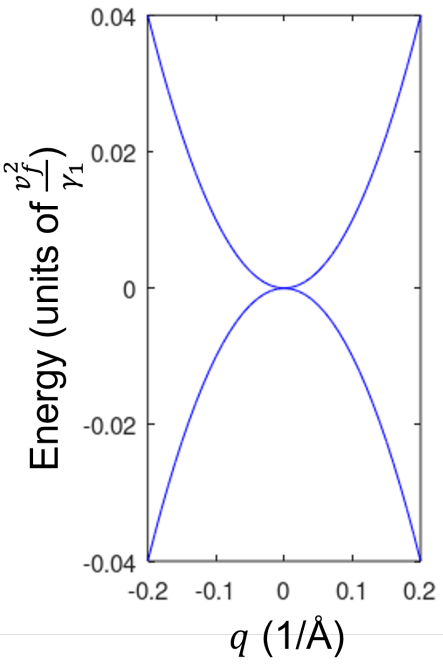

Figure 2.7: BLG gapless parabolic dispersion around K-point in dimensionless units.

$$\psi_+(\vec{q}) = \begin{pmatrix} \theta_+ \\ \chi_+ \end{pmatrix} = \frac{1}{\sqrt{N_q}} \begin{pmatrix} e^{-i\phi(\vec{q})} \\ -e^{-i\phi(\vec{q})} \\ \frac{\gamma_1 e^{-2i\phi(\vec{q})}}{v_f|\vec{q}|} \\ -\frac{\gamma_1}{v_f|\vec{q}|} \end{pmatrix}, \tag{2.47a}$$

$$\psi_-(\vec{q}) = \begin{pmatrix} \theta_- \\ \chi_- \end{pmatrix} = \frac{1}{\sqrt{N_q}} \begin{pmatrix} e^{-i\phi(\vec{q})} \\ e^{-i\phi(\vec{q})} \\ -\frac{\gamma_1 e^{-2i\phi(\vec{q})}}{v_f|\vec{q}|} \\ -\frac{\gamma_1}{v_f|\vec{q}|} \end{pmatrix}, \tag{2.47b}$$

where $q_x + iq_y = |\vec{q}|e^{i\phi(\vec{q})}$ and $N_q = \sqrt{2 + 2\frac{\gamma_1}{v_f|\vec{q}|}}$. The dispersion is parabolic and gapless around the $\vec{K}$ point as show in Fig. 2.7. If we focus on the two lowest energy bands the wavefunction is localized on the two uncoupled sublattices A_1 and B_2. The wavefunction around the K point can be written as

$$|+\rangle = \frac{1}{\sqrt{2}} \begin{pmatrix} 1 \\ e^{-2i\phi} \end{pmatrix} \tag{2.48}$$

Let's compute Berry's phase for bulk BLG in the CB. Berry's phase is given by

$$\gamma = i \oint_{\vec{k}} \vec{A} \cdot d\vec{k}. \tag{2.49}$$

The vector potential in the CB is given by

$$\vec{A} = \langle +|\nabla_{\vec{k}}|+\rangle . \tag{2.50}$$

Since our eigenvector only depends on the angle ϕ then there is only 1 component to the vector potential in the ϕ direction so we have

$$A_\phi = \frac{1}{2} \langle +|\frac{1}{k}\frac{\partial}{\partial\phi}|+\rangle = -2i \langle +|+\rangle = -i \tag{2.51}$$

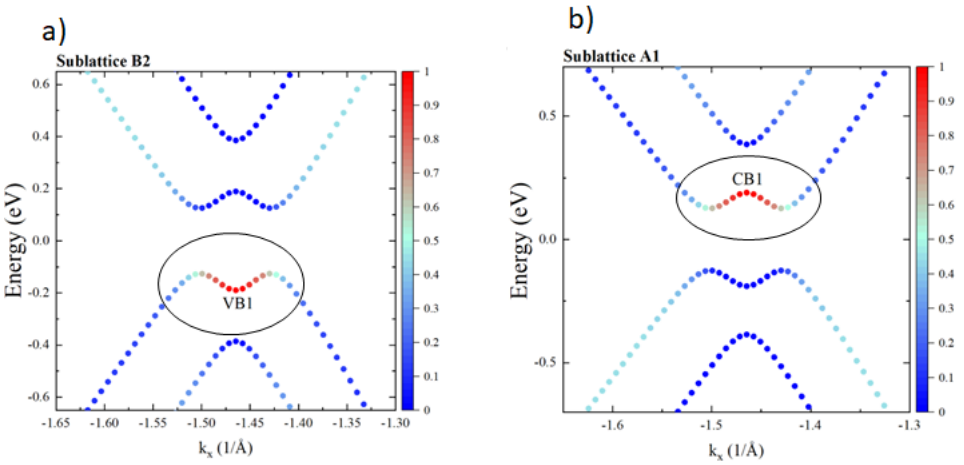

Figure 2.8: BLG dispersion around $\vec{K}$-point with an applied electric field for $V_E \approx 0.38$ eV, $\gamma_0 \approx -2.5$ eV and $\gamma_1 \approx 0.34$ eV. The color map shows the occupations of sublattice B2 (a) and sublattice A1 (b) around the $\vec{K}$-point. CB1 corresponds to the bottom of the CB, while VB1 corresponds to the top of the VB.

So then Berry's phase is just

$$\gamma = i \oint_{\vec{k}} \vec{A} \cdot d\vec{k} = \int_0^{2\pi} dk = 2\pi \tag{2.52}$$

We also observe a phase difference of $e^{2i\phi(\vec{q})}$ between the two uncoupled sublattices consistent with Ref. [17] and a Berry phase of 2π at the $\vec{K}$ point.

We now proceed to apply an electric field to BLG by biasing the two layers with respect to each other. We model this by placing layer 1 at a potential $V/2$ and the layer 2 at $-V/2$ so that the potential difference between the layers is V. Our Hamiltonian is given by [1]

$$\mathbf{H}(\vec{k}) = \begin{pmatrix} \frac{V}{2} & \gamma_0 f\left(\vec{k}\right) & 0 & 0 \\ \gamma_0 f^*\left(\vec{k}\right) & \frac{V}{2} & \gamma_1 & 0 \\ 0 & \gamma_1 & -\frac{V}{2} & \gamma_0 f\left(\vec{k}\right) \\ 0 & 0 & \gamma_0 f^*\left(\vec{k}\right) & -\frac{V}{2} \end{pmatrix}. \tag{2.53}$$

Fig. 2.8 shows the result of numerically diagonalizing this Hamiltonian at discretized $\vec{k}$ points around the $\vec{K}$ point. The result is the opening of a gap proportional to the applied field. The remarkable property is that this band gap is tunable with

electric field and large interest in the optical properties of BLG emerged for its potential application in optoelectronics. We also see the electrons at the bottom of the conduction band (CB) tend to localize on Sublattice A1, while the electrons at the top of the valence band (VB) tend to localize on sublattice B2 as seen in Fig. 2.8. These are the two uncoupled sublattices that have a relative phase difference of $e^{2i\phi}$. The pseudospin winding number n_w is then defined as the number of rotations that a pseudospin vector undergoes when the electronic wave vector rotates fully one time around the Dirac point. In BLG this phase difference gives a winding number of 2 and a Berry phase of 2π [15–17] and will have physical consequences in the optical properties discussed in chapter 6.

2.1.3 Tight-binding model for graphene quantum dots

Thus far we have discussed bulk graphene and BLG. We have found that for single layer graphene the energy gap between the VB and CB is zero, and at low energies (around the $\vec{K}$ or $\vec{K}'$ points) the dispersion is linear. BLG is as well gapless but exhibits parabolic dispersion around the $\vec{K}$ (or $\vec{K}'$) point. We found that in BLG an applied electric field opens a gap, the size of which can be tuned by changing the strength of the applied field.

In this section, we will study finite graphene flakes as well as introduce second quantization. In graphene, there are two edge types: armchair edges and zigzag edges. We will focus on mainly three types of geometries: triangular graphene quantum dots with zigzag edges, and hexagonal graphene quantum dots with armchair or zigzag edges as seen in Fig. 2.9.

We begin by defining our Hamiltonian for a single electron in our finite graphene flake as

$$\hat{H} = \frac{\hat{p}^2}{2m} + \sum_j \hat{V}_j \left(\vec{r} - \vec{R}_j\right), \tag{2.54}$$

where j runs over atomic positions. We then expand our wavefunction in the basis of

p_z atomic orbitals as

$$\psi\left(\vec{r}\right) = \sum_{j\sigma} c_{j\sigma}\phi_{p_z}\left(\vec{r} - \vec{R}_j\right). \tag{2.55}$$

We would now like to write our Hamiltonian in second quantization in order to pre-

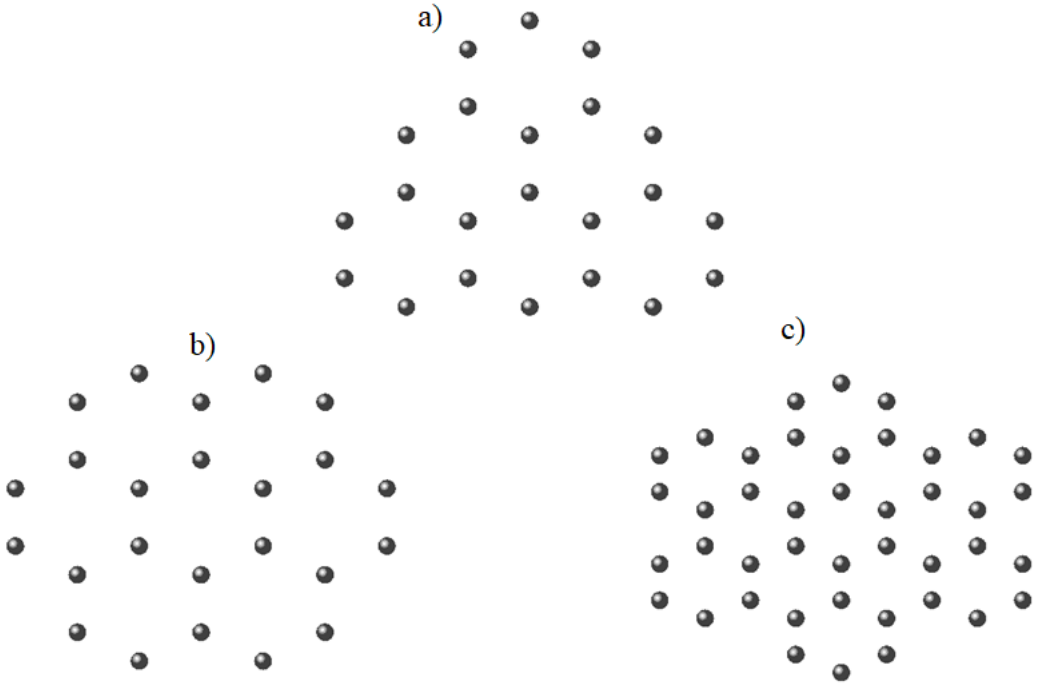

Figure 2.9: (a) $N = 22$ Triangular graphene quantum dot with zigzag edges. (b) $N = 24$ hexagonal graphene quantum dot with zigzag edges also known as coronene. (c) $N = 42$ Hexagonal graphene quantum dot with armchair edges.

pare for many-electron systems in later chapters. Let us introduce the field operators as

$$\psi\left(\vec{r}\right) = \sum_{j\sigma} c_{j\sigma}\phi_{p_z}\left(\vec{r} - \vec{R}_j\right). \tag{2.56a}$$

$$\psi^{\dagger}\left(\vec{r}\right) = \sum_{j\sigma} c^{\dagger}_{j\sigma}\phi^{*}_{p_z}\left(\vec{r} - \vec{R}_j\right), \tag{2.56b}$$

where $\psi\left(\vec{r}\right)$, $\psi^{\dagger}\left(\vec{r}\right)$ are now field operators which create electrons at a position $\vec{r}$. $c^{\dagger}_{j\sigma}(c_j)$ create (annihilate) an electron with spin σ on the p_z orbital on site j. They

act on vacuum and a filled state to create new occupation states

$$c_{j\sigma}\left|0\right\rangle \quad = 0, \tag{2.57a}$$

$$c_{j\sigma}^{\dagger}\left|0\right\rangle \quad = \left|j\sigma\right\rangle, \tag{2.57b}$$

where $|j\sigma\rangle$ tells us site j is occupied with an electron on the p_z orbital which has spin σ. Our creation and annihilation operators $c_{j\sigma}^{\dagger}$, $c_{j\sigma}$ satisfy the anti-commutator relations given by

$$\{c_{i\sigma}, c_{j\sigma}\} = \{c_{i\sigma}^{\dagger}, c_{j\sigma}^{\dagger}\} = 0, \tag{2.58a}$$

$$\{c_{i\sigma}^{\dagger}, c_{j\sigma}\} = \delta_{ij}. \tag{2.58b}$$

We now use the field operators introduced in Eq. 2.56 to derive the Hamiltonian in second quantization:

$$\begin{aligned}\mathbf{H} = \int d\vec{r}\psi^{\dagger}\left(\vec{r}\right)\hat{H}\psi\left(\vec{r}\right) &= \sum_{j,j'\sigma,\sigma'} c_{j\sigma}^{\dagger}c_{j'\sigma'}\int d\vec{r}\phi_{p_z}^{*}\left(\vec{r}-\vec{R}_j\right)\hat{H}\phi_{p_z}\left(\vec{r}-\vec{R}_{j'}\right) \\ &= \sum_{j,j'\sigma,\sigma'}\left\langle j\sigma|\hat{H}|j'\sigma'\right\rangle c_{j\sigma}^{\dagger}c_{j'\sigma'}.\end{aligned} \tag{2.59}$$

Now let us analyze the matrix element that need to be computed, we have

$$\begin{aligned}\left\langle j\sigma|\hat{H}|j'\sigma'\right\rangle &= \left\langle j\sigma\right|\left[\frac{\hat{p}^2}{2m}+\sum_{j''}\hat{V}_{j''}\left(\vec{r}-\vec{R}_{j''}\right)\right]\left|j'\sigma\right\rangle \\ &= \left\langle j\sigma\right|\left[\frac{\hat{p}^2}{2m}+\hat{V}_{j'}\left(\vec{r}-\vec{R}_{j'}\right)\right]\left|j'\sigma'\right\rangle + \left\langle j\sigma\right|\left[\sum_{j''\neq j'}\hat{V}_{j''}\left(\vec{r}-\vec{R}_{j''}\right)\right]\left|j'\sigma'\right\rangle \\ &= \underbrace{\epsilon_{j'}\delta_{jj'}\delta_{\sigma\sigma'}}_{=0} + \left\langle j\sigma\right|\left[\hat{V}_j\left(\vec{r}-\vec{R}_j\right)\right]\left|j'\sigma'\right\rangle \\ &= t_{jj'}\delta_{\sigma,\sigma'},\end{aligned} \tag{2.60}$$

where we have set the energy of all carbon atoms $\epsilon_j = 0$. Furthermore, we have ignored three-center integrals and set our hopping parameter $t_{jj'}\delta_{\sigma,\sigma'} = \left\langle j\sigma\right|\left[\hat{V}_j\left(\vec{r}-\vec{R}_j\right)\right]\left|j'\sigma'\right\rangle$.

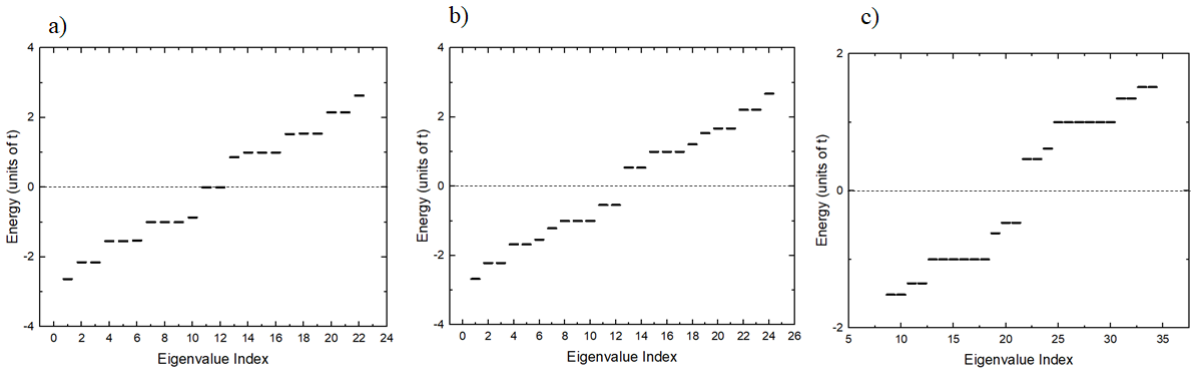

Figure 2.10: Corresponding single-particle spectrum in the NN approximation for the structures shown in Fig. 2.9. Energy is in units of the NN hopping parameter t. The dashed line denotes the Fermi level.

Finally, our Hamiltonian for our finite graphene flakes can be written as

$$\hat{\mathbf{H}} = \sum_{i,j,\sigma} t_{ij} c^{\dagger}_{i\sigma} c_{j\sigma}. \tag{2.61}$$

Now let us take a NN approximation in which we take only the hopping between atoms i, and j being nearest neighbours and assuming further hopping terms are negligible. We can then write our Hamiltonian as

$$\hat{\mathbf{H}} = t \sum_{\langle i,j\rangle,\sigma} c^{\dagger}_{i\sigma} c_{j\sigma}, \tag{2.62}$$

where t is the hopping between NN atoms. Fig. 2.10 shows the energy spectrum obtained by solving Eq. 2.62 for the GQDs in Fig. 2.9. We start by looking at the spectrum for the triangular dot Fig. 2.10(a). We observe two degenerate states at the Fermi level consistent with Ref. 97.

Meanwhile, in the structures which preserve sublattice symmetry where the number of A atoms is the same as the number of B atoms, the finite nature of the structure in Fig. 2.9(b) and (c) actually shows an opening of the energy gap, unlike in the bulk which has no gap. How the gap changes as a function of size is different depending on the edge and will be analyzed in greater detail in later chapters.

We note that how the gap changes as a function of size for a single layer and a

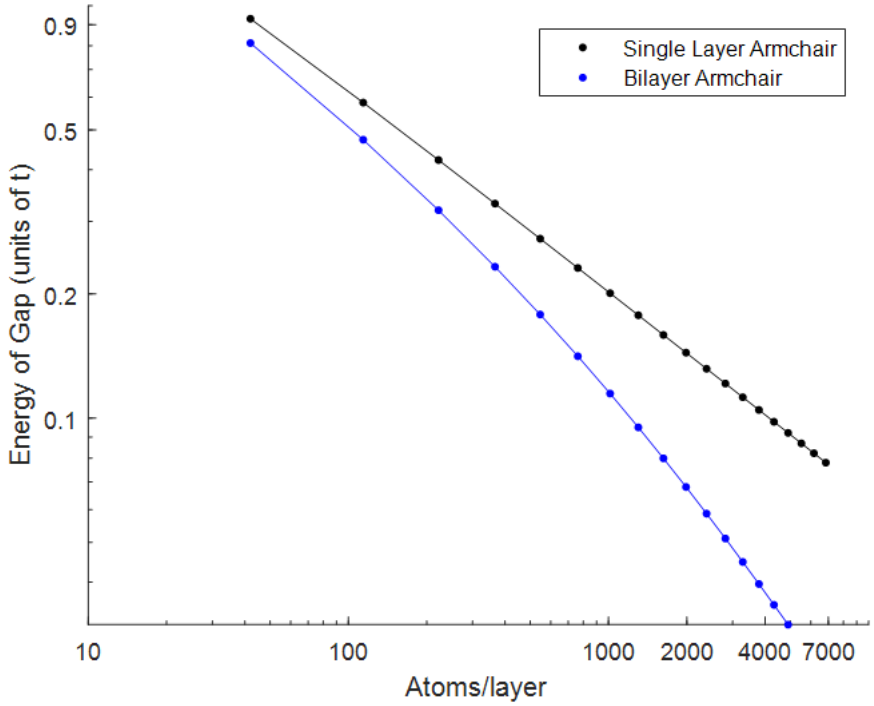

Figure 2.11: Energy gap for single and bilayer layer hexagonal graphene quantum dot with armchair edges as a function of the number of atoms per layer in logarithmic scale.

bilayer is also different. Fig. 2.11 shows how the energy gap changes as a function of size for a single layer and bilayer armchair hexagonal GQD. We would like to note this is in agreement with Ref. [98]. This difference can be understood in terms of the expectation that the largest wavelength to fit inside our quantum dot should be proportional to the radius of the quantum dot R. In other words $\lambda_{max} \propto R$. Since our structures are two dimensional, the number of atoms $N \propto R^2$, so that $\lambda_{max} \propto \sqrt{N}$. Since $\lambda_{max} = \frac{2\pi}{k_{min}}$, we have $k_{min} \propto \frac{1}{\sqrt{N}}$. Now in the case of a single layer we saw that in the bulk case around the $\vec{K}$ point, the dispersion was linear (Fig. 2.4) while, in the bilayer case, the dispersion was parabolic (Fig.2.7). In other words, for a single layer $k_{min} \propto E_{gap}$ and for a bilayer $k_{min}^2 \propto E_{gap}$, so that for a single layer we have $E_{gap} \propto \frac{1}{\sqrt{N}}$ while for a bilayer we have $E_{gap} \propto \frac{1}{N}$. It is worth noting that this is a limiting case and is more accurate for large structures where the dispersion starts to mimic that of bulk.

2.2 Many-body problem

Up until now we considered single-particle properties of 2D systems in which we ignored interactions among electrons. In other words, each electron was treated independently and identically. In order to get an accurate description of the electronic, optical and magnetic properties of a 2D system, electron-electron interactions must be included [33, 39, 75, 76, 95, 98–102]. The complications with dealing with many-body physics arises due to the rapidly exploding size of the Hilbert space. To give context; if we took a 1D chain with 50 sites and took one orbital per site and considered 50 electrons on these sites (half-filled), the Hilbert space dimension is on the order of 10^{29}, something clearly unmanageable. An approximation was already invoked here as well in which we took only one orbital per site. This demonstrates the rapidly growing Hilbert space that can exist in even small systems, and approximate approaches must be taken in order to compute the many-body ground and excited states of the system.

In this chapter, we will introduce the many-body problem, discuss the numerical complexity of computing Coulomb matrix elements and introduce the Hubbard model, configuration interaction, and the Bethe-Salpeter equation in order to help solve correlated electron problems. In section 2.3, we introduce mean-field methods to approximately solve the many-body problem and realize an optimized basis when including correlations in order to reduce the size of our Hilbert space which is described in detail in section 2.4.

2.2.1 Many-body Hamiltonian

Let us consider N_e interacting electrons subject to the potential of nuclei. Our Hamiltonian is given by

$$H = \sum_{i=1}^{N_e} \left[-\frac{\hbar^2}{2m^*}\nabla_i^2 + V(\vec{r_i}) \right] + \frac{1}{2}\sum_{i\neq j}^{N_e} \frac{e^2}{\kappa|\vec{r_i} - \vec{r_j}|}. \tag{2.63}$$

The first term in the Hamiltonian corresponds to the kinetic energy of electrons with effective mass m^*. The second term describes the potential these electrons are subject to. The final term describes Coulomb interaction among electrons. In section 2.1.3 we rewrote the Hamiltonian for GQDs in second quantization, we will write this Hamiltonian in second quantization but in the basis of itinerant states instead of the basis of localized orbitals (site representation). Let φ_p be the eigenstate of the single-particle Hamiltonian, in other words

$$\left[-\frac{\hbar^2}{2m^*}\nabla^2 + V(\vec{r})\right]\varphi_p(\vec{r}) = \epsilon_p\varphi_p(\vec{r}). \tag{2.64}$$

Then our field operators are

$$\psi(\vec{r}) = \sum_{p\sigma} c_{p\sigma}\varphi_p(\vec{r}), \tag{2.65a}$$

$$\psi^\dagger(\vec{r}) = \sum_{p\sigma} c^\dagger_{p\sigma}\varphi^*_p(\vec{r}), \tag{2.65b}$$

Then let's write the pairwise interaction $\frac{e^2}{\kappa|\vec{r_1}-\vec{r_2}|}$ in second quantization:

$$\begin{aligned}
&\int\int d\vec{r_1}d\vec{r_2}\psi^\dagger(\vec{r_1})\,\psi^\dagger(\vec{r_2})\,\frac{e^2}{\kappa|\vec{r_1}-\vec{r_2}|}\psi(\vec{r_2})\,\psi(\vec{r_1}) \\
&= \sum_{p,q,r,s,\sigma,\sigma'} c^\dagger_{p\sigma}c^\dagger_{q\sigma'}c_{r\sigma'}c_{s\sigma}\int d\vec{r}\varphi^*_p(\vec{r_1})\varphi^*_q(\vec{r_2})\frac{e^2}{\kappa|\vec{r_1}-\vec{r_2}|}\varphi_r(\vec{r_2})\varphi_s(\vec{r_1}) \\
&= \sum_{p,q,r,s,\sigma,\sigma'} \langle p\sigma, q\sigma'|V|r\sigma', s\sigma\rangle\, c^\dagger_{p\sigma}c^\dagger_{q\sigma'}c_{r\sigma'}c_{s\sigma}.
\end{aligned} \tag{2.66}$$

Note, we have used the fact that Coulomb interaction conserves the projection of the total spin operator S_z. We can write Eq. 2.63 in the basis of itinerant orbitals in second quantized form as

$$H = \sum_{p,\sigma}\epsilon_{p\sigma}c^\dagger_{p\sigma}c_{p\sigma} + \frac{1}{2}\sum_{p,q,r,s,\sigma,\sigma'}\langle pq|V|rs\rangle\, c^\dagger_{p\sigma}c^\dagger_{q\sigma'}c_{r\sigma'}c_{s\sigma}, \tag{2.67}$$

where we have dropped the spin indices in the Coulomb matrix elements by assuming the matrix elements do not depend on spin, and will continue to do so throughout

this thesis unless specified otherwise.

2.2.2 Coulomb matrix elements

The Hamiltonian in Eq. 2.67 requires the solution of the single-particle part of the Hamiltonian. Throughout this thesis, the TB model is the primary method used to obtain the single-particle solution. We also require the calculation of Coulomb matrix elements $\langle pq|V|rs\rangle$. They are given explicitly by

$$\langle pq|V|rs\rangle = R_y \int\int d\vec{r}_1 d\vec{r}_2 \psi_p^*(\vec{r}_1)\psi_q^*(\vec{r}_2)\frac{2}{|\vec{r}_1 - \vec{r}_2|}\psi_r(\vec{r}_2)\psi_s(\vec{r}_1), \tag{2.68}$$

where distances are in effective Bohr radius a_b, and $R_y = \frac{\hbar^2}{2m^* a_b^2} = \frac{1}{8\pi}\frac{e^2}{\kappa\epsilon_0 a_b}$ is the effective Rydberg constant. It is worth noting the computational complexity of Coulomb matrix elements. In general there are N^4 elements that need to be computed where N is the number of single-particle states taken, and each one of these calculations is an order N^6 procedure, requiring a 6-dimensional integral to be solved. In later chapters, we will discuss how we tackle this problem for specific systems.

It is convenient in general to compute Coulomb matrix elements in the site representation and rotate these matrix elements to the itinerant basis. Recall, the operators in Eq. 2.57 that create and annihilate electrons on sites. If we now assume a more general case where we have more than one orbital, we can consider Coulomb matrix elements $\langle i\alpha, j\beta|V|k\delta, l\gamma\rangle$, where i, j, k, l correspond to sites, and $\alpha, \beta, \delta, \gamma$ correspond to orbitals. We can obtain the matrix elements in the itinerant basis by the following rotation

$$\langle pq|V|rs\rangle = \sum_{i,j,k,l}\sum_{\alpha,\beta,\delta,\gamma} \left(C_{\alpha i}^p\right)^* \left(C_{\beta j}^q\right)^* C_{\delta k}^r C_{\gamma l}^s \langle i\alpha, j\beta|V|k\delta, l\gamma\rangle, \tag{2.69}$$

where $C_{\alpha i}^p$ is the probability amplitude in the localized basis for site i, and orbital α for itinerant state p. These need to be computed by rotating the eigenvectors obtained when solving the single-particle problem in the itinerant basis or by directly solving the single-particle problem in the localized basis. The convenience of comput-

ing matrix elements in the site representation is to take advantage of the short-range nature of quantum mechanical Coulomb matrix elements and make a long-range approximation allowing us to only need to compute a small number of the 6-dimensional integrals in Eq. 2.68. For specific systems, the details of the calculations are slightly different and in later chapters we'll discuss in further details how these calculations are done.

2.2.3 Hubbard model

As stated before, the Hamiltonian in Eq. 2.67 requires the calculation of N^4 6-dimensional integrals. The Hubbard model reduces this to retaining only a single Coulomb matrix element. To better understand the Hubbard model [103], let us rotate that Hamiltonian Eq. 2.67 to the site representation and assume only one orbital per site as described in section 2.1.3. Our Hamiltonian is given by

$$H = \sum_{i,\sigma} \epsilon_{i\sigma} c^\dagger_{i\sigma} c_{i\sigma} + \sum_{i,j,\sigma} t_{ij\sigma} c^\dagger_{i\sigma} c_{j\sigma} + \frac{1}{2} \sum_{i,j,k,l,\sigma,\sigma'} \langle ij|V|kl\rangle \, c^\dagger_{i\sigma} c^\dagger_{j\sigma'} c_{k\sigma'} c_{l\sigma}. \tag{2.70}$$

Now let us retain only the largest Coulomb matrix element defined as $U = \langle ii|V|ii\rangle$ which corresponds to the energy of placing two electrons on the same orbital on the same site. Then our Hamiltonian becomes

$$H = \sum_{i,\sigma} \epsilon_{i\sigma} c^\dagger_{i\sigma} c_{i\sigma} + \sum_{i,j,\sigma} t_{ij\sigma} c^\dagger_{i\sigma} c_{j\sigma} + \frac{1}{2} U \sum_{i,\sigma,\sigma'} c^\dagger_{i\sigma} c^\dagger_{i\sigma'} c_{i\sigma'} c_{i\sigma}. \tag{2.71}$$

Summing over spin indices and using the Pauli exclusion principle we get

$$H = \sum_{i,\sigma} \epsilon_{i\sigma} c^\dagger_{i\sigma} c_{i\sigma} + \sum_{i,j,\sigma} t_{ij\sigma} c^\dagger_{i\sigma} c_{j\sigma} + \frac{1}{2} U \sum_{i} \left(c^\dagger_{i\uparrow} c^\dagger_{i\downarrow} c_{i\downarrow} c_{i\uparrow} + c^\dagger_{i\downarrow} c^\dagger_{i\uparrow} c_{i\uparrow} c_{i\downarrow} \right). \tag{2.72}$$

Using Eq. 2.58 we can write

$$H = \sum_{i,\sigma} \epsilon_{i\sigma} c^\dagger_{i\sigma} c_{i\sigma} + \sum_{i,j,\sigma} t_{ij\sigma} c^\dagger_{i\sigma} c_{j\sigma} + U \sum_{i} c^\dagger_{i\uparrow} c^\dagger_{i\downarrow} c_{i\downarrow} c_{i\uparrow}, \tag{2.73}$$

which is the familiar Hubbard model. This Hubbard model has been used to understand metallic phases, and Mott insulating phases in 2D honeycomb lattices [81] and has been used to predict the spin of the ground state for bipartite lattices [104]. Both of which we will rely on in later chapters to guide the understanding of results.

2.2.4 Configuration interaction

The Hubbard model ignores scattering between electrons on different sites, and is a minimialistic model. In order to capture the full effects of Coulomb interaction a more exact approach is needed. In configuration interaction (CI) we begin with the full many-body Hamiltonian described in Eq. 2.67 and write our wavefunction as a linear combination of Slater determinants. In other words our wavefunction is given by

$$\Psi_{CI} = \sum_{\mu} d_{\mu} \Phi_{\mu}, \tag{2.74}$$

where Φ_{μ} is a Slater determinant (or configuration) defined as

$$\Phi_{\mu} = \prod_{q\downarrow \in Occ} c^{\dagger}_{q\uparrow} \prod_{q\uparrow \in Occ} c^{\dagger}_{q\downarrow} \left|0\right\rangle, \tag{2.75}$$

where we are taking a product over the states that are occupied for a specific configuration μ. In general, the number of configurations contained in Eq. 2.74 allows us to control the accuracy of results but rapidly grows with the number of single particle states, and number of electrons. Taking the most relevant configurations to understand the low-energy spectrum is required in order to be able to compute reasonably.

We will now demonstrate the use of CI on the problem of 2 degenerate levels and 2 electrons. Let $M = 2 \times 2$ be the number of single-particle states (and extra factor of two for spin) and N be the number of electrons, then the number of configurations is given by

$$N_{conf} = \binom{M}{N}. \tag{2.76}$$

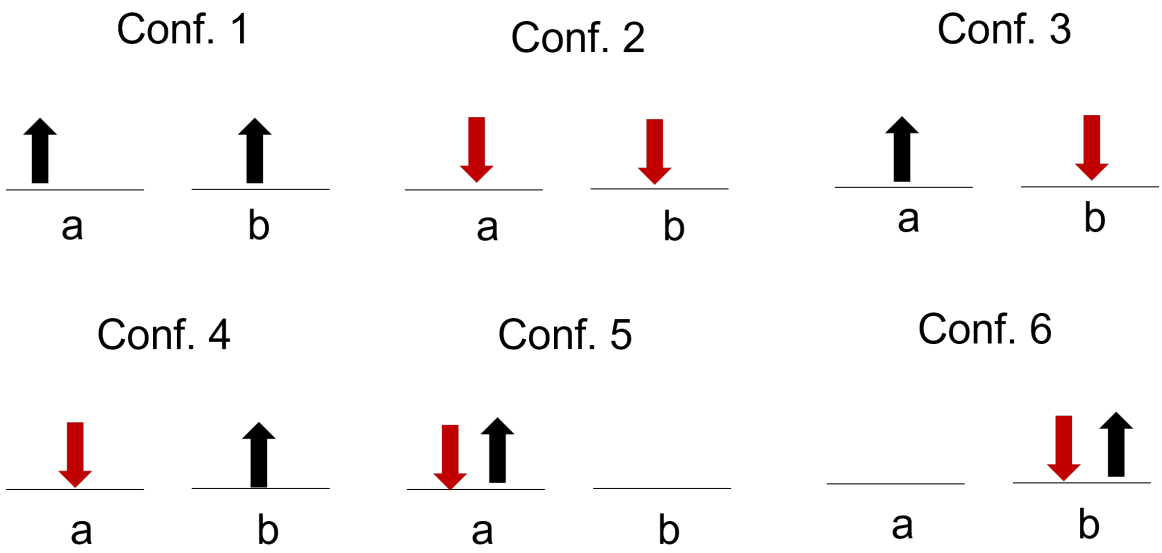

Figure 2.12: All possible configurations for two electrons on two degenerate levels. The configurations are ordered, and the levels are labelled "a" and "b".

The number of configurations in our problem is six. Fig. 2.12 shows all possible configurations. There is one state with total $s_z = 1$, four states with $s_z = 0$, and one state with $s_z = -1$. The configurations are labelled from 1 to 6, and can be written explicitly as

$$|1\rangle = c^\dagger_{b\uparrow} c^\dagger_{a\uparrow} |0\rangle \,, \tag{2.77a}$$

$$|2\rangle = c^\dagger_{b\downarrow} c^\dagger_{a\downarrow} |0\rangle \,, \tag{2.77b}$$

$$|3\rangle = c^\dagger_{a\uparrow} c^\dagger_{b\downarrow} |0\rangle \,, \tag{2.77c}$$

$$|4\rangle = c^\dagger_{b\uparrow} c^\dagger_{a\downarrow} |0\rangle \,, \tag{2.77d}$$

$$|5\rangle = c^\dagger_{a\uparrow} c^\dagger_{a\downarrow} |0\rangle \,, \tag{2.77e}$$

$$|6\rangle = c^\dagger_{b\uparrow} c^\dagger_{b\downarrow} |0\rangle \,, \tag{2.77f}$$

where $|0\rangle$ is the vacuum state. In the basis of configurations, we construct our Hamiltonian matrix. This is done by computing matrix elements of the Hamiltonian defined in Eq. 2.67. We will show an example calculation of one matrix element, let

us choose the element $\langle 1|\hat{H}|1\rangle$, so we have

$$\begin{aligned}\langle 1|\hat{H}|1\rangle &= \langle 0|\, c_{a\uparrow}c_{b\uparrow}\left[\sum_{p,\sigma}\epsilon_{p\sigma}c^\dagger_{p\sigma}c_{p\sigma}+\frac{1}{2}\sum_{p,q,r,s,\sigma,\sigma'}\langle pq|V|rs\rangle\, c^\dagger_{p\sigma}c^\dagger_{q\sigma'}c_{r\sigma'}c_{s\sigma}\right]c^\dagger_{b\uparrow}c^\dagger_{a\uparrow}\,|0\rangle \\ &= \sum_{p,\sigma}\epsilon_{p\sigma}\,\langle 0|\, c_{a\uparrow}c_{b\uparrow}c^\dagger_{p\sigma}c_{p\sigma}c^\dagger_{b\uparrow}c^\dagger_{a\uparrow}\,|0\rangle+\frac{1}{2}\sum_{p,q,r,s,\sigma,\sigma'}\langle pq|V|rs\rangle\,\langle 0|\, c_{a\uparrow}c_{b\uparrow}c^\dagger_{p\sigma}c^\dagger_{q\sigma'}c_{r\sigma'}c_{s\sigma}c^\dagger_{b\uparrow}c^\dagger_{a\uparrow}\,|0\rangle \\ &= \epsilon_{a\uparrow}+\epsilon_{b\uparrow}+\frac{1}{2}\left[\langle ab|V|ba\rangle+\langle ba|V|ab\rangle-\langle ab|V|ab\rangle-\langle ba|V|ba\rangle\right].\end{aligned} \tag{2.78}$$

Using the fact that $\langle ij|V|kl\rangle = \langle ji|V|lk\rangle$, and setting $\epsilon_{a\uparrow} = \epsilon_{b\uparrow} = 0$ we get

$$\langle 1|\hat{H}|1\rangle = \langle ab|V|ba\rangle - \langle ab|V|ab\rangle\,. \tag{2.79}$$

Computing the rest of the matrix elements, the CI Hamiltonian is then given by

$$H_{CI} = \begin{pmatrix} V_{abba}-V_{abab} & 0 & 0 & 0 & 0 & 0 \\ 0 & V_{abba}-V_{abab} & 0 & 0 & 0 & 0 \\ 0 & 0 & V_{abba} & V_{baba} & V_{aaab} & V_{bbba} \\ 0 & 0 & V_{baba} & V_{abba} & V_{aaab} & V_{bbba} \\ 0 & 0 & V_{aaab} & V_{aaab} & V_{aaaa} & V_{aabb} \\ 0 & 0 & V_{bbba} & V_{bbba} & V_{aabb} & V_{bbbb} \end{pmatrix}. \tag{2.80}$$

where I have assumed the matrix elements are all real for simplicity. Furthermore, I have used symmetries of the Coulomb matrix elements to reduce the number of "parameters" of the Hamiltonian, for example $V_{aaab} = V_{baaa}$. We see that the Hamiltonian is block diagonal. The first block corresponds to the $s_z = 1$ subspace and the size is 1×1, the second block is the $s_z = -1$ subspace and the size is 1×1, and finally the last block is a 4×4 block corresponding to the the $s_z = 0$ subspace. We see that we can separate our Hilbert space into subspaces organized by s_z since there is no terms in the Hamiltonian that couple configurations with different s_z. The challenges and utility of CI will be seen in later chapters when applied to other problems.

2.2.5 Bethe-Salpeter equation

Consider a system in which the ground state is given as a single Slater determinant with a fully occupied VB, and an energy gap separating the VB from the CB. If one shines light of the right energy, an electron will be excited from the VB to the conduction forming a one-pair excitation. These one-pair excitations can couple forming excitons. We will describe how to compute these excitons in this section.

One can start with CI and restrict configurations to only one-pair excitations in order to understand the optical properties. In this section, we will derive the Bethe-Salpeter Equation (BSE) by restricting the wavefunction to a linear combination of one-pair excitations. We first begin with our many-body Hamiltonian given by

$$\begin{aligned}\hat{H}_{MB} &= \sum_m E_m c_m^\dagger c_m + \frac{1}{2}\sum_{m_1,m_2,m_3,m_4} \langle m_1 m_2|V|m_3 m_4\rangle c_{m_1}^\dagger c_{m_2}^\dagger c_{m_3} c_{m_4} - \sum_{m_1,m_2} V^P_{m_1 m_2} c_{m_1}^\dagger c_{m_2} \\ &= \hat{H}^{(1)} + \hat{H}^{(2)} - \hat{H}^{(3)}.\end{aligned} \tag{2.81}$$

Here E_m are single-particle energies, $V^P_{m_1 m_2}$ corresponds to the positive background, and we hide spin indices in the state index to simplify calculations. The positive background is given explicitly as

$$V^P_{m_1 m_2} = \sum_m^{N_{occ}} \langle m_1 m|V|m m_2\rangle, \tag{2.82}$$

where N_{occ} corresponds to the number of occupied states. We have assumed that the positive charges occupy the orbitals that are the same as those of the electrons, with the exception that we assume the positive charges do not scatter. Let us first define our groundstate as

$$|GS\rangle = \prod_m^{N_{occ}} c_m^\dagger |0\rangle . \tag{2.83}$$

Now let us write our wavefunction for an excitonic state μ as

$$|\psi^\mu\rangle = \sum_{i,f} F^\mu_{i\neq f} c_f^\dagger c_i |GS\rangle = \sum_\nu F^\mu_\nu |X_\nu\rangle , \tag{2.84}$$

where c_i has removed an electron from state i in the GS leaving behind a "hole", and $c_f^\dagger$ places this electron in a state f. The sum over ν corresponds to a sum over all possible electron-hole pairs. If we act our Hamiltonian given by Eq. 2.81 on this wavefunction we generate a matrix equation known as the Bethe-Salpeter equation. There will be three terms we are concerned with: one which corresponds to the single-particle term in the Hamiltonian, one with Coulomb interactions, and one for the positive background. Let us focus on each term separately and compute the matrix elements. For the single-particle term we have

$$\langle X_{\nu_2}| \hat{H}^{(1)} |X_{\nu_1}\rangle = \sum_m E_m \langle GS| c_{i_2}^\dagger c_{f_2} c_m^\dagger c_m c_{f_1}^\dagger c_{i_1} |GS\rangle , \tag{2.85}$$

It can be very tedious to compute the expectation value $\langle GS| c_{i_2}^\dagger c_{f_2} c_m^\dagger c_m c_{f_1}^\dagger c_{i_1} |GS\rangle$ above. There are many different pairings of operators, however only a limited number of these are physically relevant. Using Wick's theorem [105] we can compute expectations values of this form. Let us do an example on the single-particle term: we can apply Wick's theorem, noting that $i \neq f$ we get

$$\begin{aligned}\langle GS| c_{i_2}^\dagger c_{f_2} c_m^\dagger c_m c_{f_1}^\dagger c_{i_1} |GS\rangle &= \langle GS| c_{i_2}^\dagger c_m |GS\rangle \langle GS| c_{f_2} c_m^\dagger c_{f_1}^\dagger c_{i_1} |GS\rangle \\ &\quad + \langle GS| c_{i_2}^\dagger c_{i_1} |GS\rangle \langle GS| c_{f_2} c_m^\dagger c_m c_{f_1}^\dagger |GS\rangle \\ &= \delta_{m,i_2} \langle GS| c_{f_2} c_m^\dagger c_{f_1}^\dagger c_{i_1} |GS\rangle + \delta_{i_1,i_2} \langle GS| c_{f_2} c_m^\dagger c_m c_{f_1}^\dagger |GS\rangle .\end{aligned} \tag{2.86}$$

We now analogously expand the terms $\langle GS| c_{f_2} c_m^\dagger c_{f_1}^\dagger c_{i_1} |GS\rangle$, and $\langle GS| c_{f_2} c_m^\dagger c_m c_{f_1}^\dagger |GS\rangle$

$$\langle GS| c_{f_2} c_m^\dagger c_{f_1}^\dagger c_{i_1} |GS\rangle = - \langle GS| c_{f_2} c_{f_1}^\dagger |GS\rangle \langle GS| c_m^\dagger c_{i_1} |GS\rangle = -\delta_{f_2,f_1}\delta_{i_1,m}, \tag{2.87}$$

similarly we have

$$\begin{aligned}\langle GS|\, c_{f_2} c_m^\dagger c_m c_{f_1}^\dagger \,|GS\rangle &= \langle GS|\, c_{f_2} c_m^\dagger \,|GS\rangle \,\langle GS|\, c_m^\dagger c_{f_1} \,|GS\rangle + \langle GS|\, c_{f_2} c_{f_1}^\dagger \,|GS\rangle \,\langle GS|\, c_m^\dagger c_m \,|GS\rangle \\ &= \delta_{f_2,m}\delta_{m,f_1} + \delta_{f_2,f_1}\delta_{m\leq N_{occ}},\end{aligned} \tag{2.88}$$

where $\delta_{m\leq N_{occ}}$ is there to ensure that m corresponds to an occupied state. Putting everything together we get

$$\langle GS|\, c_{i_2}^\dagger c_{f_2} c_m^\dagger c_m c_{f_1}^\dagger c_{i_1} \,|GS\rangle = -\delta_{m,i_2}\delta_{f_2,f_1}\delta_{i_1,m} + \delta_{i_1,i_2}\delta_{f_2,m}\delta_{m,f_1} + \delta_{i_1,i_2}\delta_{f_2,f_1}\delta_{m\leq N_{occ}}, \tag{2.89}$$

thus Eq. 2.85 becomes

$$\begin{aligned}\langle X_{\nu_2}|\, \hat{H}^{(1)} \,|X_{\nu_1}\rangle &= \sum_m E_m \left(-\delta_{m,i_2}\delta_{f_2,f_1}\delta_{i_1,m} + \delta_{i_1,i_2}\delta_{f_2,m}\delta_{m,f_1} + \delta_{i_1,i_2}\delta_{f_2,f_1}\delta_{m\leq N_{occ}}\right) \\ &= -E_{i_1}\delta_{i_1,i_2}\delta_{f_2,f_1} + E_{f_1}\delta_{i_1,i_2}\delta_{f_2,f_1} + \sum_m^{N_{occ}} E_m \delta_{i_1,i_2}\delta_{f_2,f_1} \\ &= \delta_{i_1,i_2}\delta_{f_2,f_1}\left[E_{f_1} - E_{i_1} + \sum_m^{N_{occ}} E_m\right].\end{aligned} \tag{2.90}$$

Now for the Coulomb part, we have

$$\begin{aligned}&\langle X_{\nu_2}|\, \hat{H}^{(2)} \,|X_{\nu_1}\rangle \\ &= \frac{1}{2}\sum_{m_1,m_2,m_3,m_4} \langle m_1 m_2|V|m_3 m_4\rangle \,\langle GS|\, c_{i_2}^\dagger c_{f_2} c_{m_1}^\dagger c_{m_2}^\dagger c_{m_3} c_{m_4} c_{f_1}^\dagger c_{i_1} \,|GS\rangle\,,\end{aligned} \tag{2.91}$$

and after some very laborious algebra using Wick's theorem one can obtain

$$\begin{aligned}\langle X_{\nu_2}|\,\hat{H}^{(2)}\,|X_{\nu_1}\rangle = &\langle i_1 f_2|V|i_2 f_1\rangle - \langle i_1 f_2|V|f_1 i_2\rangle \\ &- \delta_{f_1,f_2}\sum_{m}^{N_{occ}}\left[\langle i_1 m|V|m i_2\rangle - \langle m i_1|V|m i_2\rangle\right] \\ &+ \delta_{i_1,i_2}\sum_{m}^{N_{occ}}\left[\langle f_2 m|V|m f_1\rangle - \langle m f_2|V|m f_1\rangle\right] \\ &+ \delta_{i_1,i_2}\delta_{f_1,f_2}\sum_{m<m_1}^{N_{occ}}\left[\langle m_1 m|V|m m_1\rangle - \langle m_1 m|V|m_1 m\rangle\right].\end{aligned} \tag{2.92}$$

The first line in the expression corresponds to vertex correction or electron hole direct and exchange interaction in the case where $f_2 = f_1$ and $i_2 = i_1$. Otherwise it is a scattering term coupling different electron hole pairs. The second line is a scattering of a hole from a state i_2 to a state i_1 due to the presence of electrons in the VB. The third term is the same but the scattering of an electron. Finally, the last term corresponds to the energy of electrons interacting in the VB and is responsible only to an overall shift in energies.

The contribution from the positive background is derived as

$$\begin{aligned}\langle X_{\nu_2}|\,\hat{H}^{(3)}\,|X_{\nu_1}\rangle = &-\delta_{f_1,f_2}\sum_{m}^{N_{occ}}\langle i_1 m|V|m i_2\rangle \\ &+ \delta_{i_1,i_2}\sum_{m}^{N_{occ}}\langle f_2 m|V|m f_1\rangle \\ &+ \delta_{i_1,i_2}\delta_{f_1,f_2}\sum_{m,m_1}^{N_{occ}}\langle m_1 m|V|m m_1\rangle.\end{aligned} \tag{2.93}$$

The first term corresponds to the interaction of the hole with the positive background, the second term corresponds to the interaction of the electron with the positive background, and finally the last term corresponds to the interaction of the positive background with itself. It is very convenient to subtract the energy of the ground state from the matrix elements of the BSE equation. So we proceed now to compute the

GS energy. One can show that

$$\langle GS|\,\hat{H}\,|GS\rangle = \sum_{m}^{N_{occ}} E_m + \sum_{m<m_1}^{N_{occ}} \left[\langle m_1 m|V|m m_1\rangle - \langle m_1 m|V|m_1 m\rangle\right]. \tag{2.94}$$

Now combining expressions, the matrix elements of the BSE with energies measured by subtracting the ground state energy is given by

$$\begin{aligned}\langle X_{\nu_2}|\,\hat{H}\,|X_{\nu_1}\rangle - \delta_{\nu_2,\nu_1}\langle GS|\,\hat{H}\,|GS\rangle = \;& \delta_{i_1,i_2}\delta_{f_2,f_1}\left[E_{f_1} - E_{i_1}\right] \\ & + \langle i_1 f_2|V|i_2 f_1\rangle - \langle i_1 f_2|V|f_1 i_2\rangle \\ & + \delta_{f_1,f_2}\sum_{m}^{N_{occ}}\langle m i_1|V|m i_2\rangle \\ & - \delta_{i_1,i_2}\sum_{m}^{N_{occ}}\langle m f_2|V|m f_1\rangle.\end{aligned} \tag{2.95}$$

In general, these are the matrix elements of our BSE. This expression can be further simplified for a particular basis. For example, if we assume that our single-particle basis corresponds to a bulk 2D material in which wavevectors k are a good quantum number, then scattering elements of the form $\langle mi|V|mj\rangle$ for $i \neq j$ vanish in order to conserve momentum. A similar consequence occurs in a DFT basis or a HF basis. Thus, if we assume we are in such a basis, we can reduce the above expression to

$$\begin{aligned}\langle X_{\nu_2}|\,\hat{H}\,|X_{\nu_1}\rangle - \delta_{\nu_2,\nu_1}\langle GS|\,\hat{H}\,|GS\rangle = \;& \delta_{i_1,i_2}\delta_{f_2,f_1}\left[\left(E_{f_1} + \Sigma_{(f_1)}\right) - \left(E_{i_1} + \Sigma_{(i_1)}\right)\right] \\ & + \langle i_1 f_2|V|i_2 f_1\rangle - \langle i_1 f_2|V|f_1 i_2\rangle.\end{aligned} \tag{2.96}$$

Our Bethe-Salpeter equation is then:

$$\begin{aligned}&\sum_{q',p',\sigma'}\left[(E_{q'} + \Sigma_{q'}) - (E_{p'} + \Sigma_{p'})\right]\delta_{p,p'}\delta_{q,q'}\delta_{\sigma,\sigma'}F^{\mu}_{p',q',\sigma'} \\ &+ \sum_{q',p',\sigma'}\left[\langle p,q'|V_C|p',q\rangle - \langle p,q'|V_C|q,p'\rangle\,\delta_{\sigma\sigma'}\right]F^{\mu}_{p',q',\sigma'} = E_{\mu}F^{\mu}_{p,q,\sigma}.\end{aligned} \tag{2.97}$$

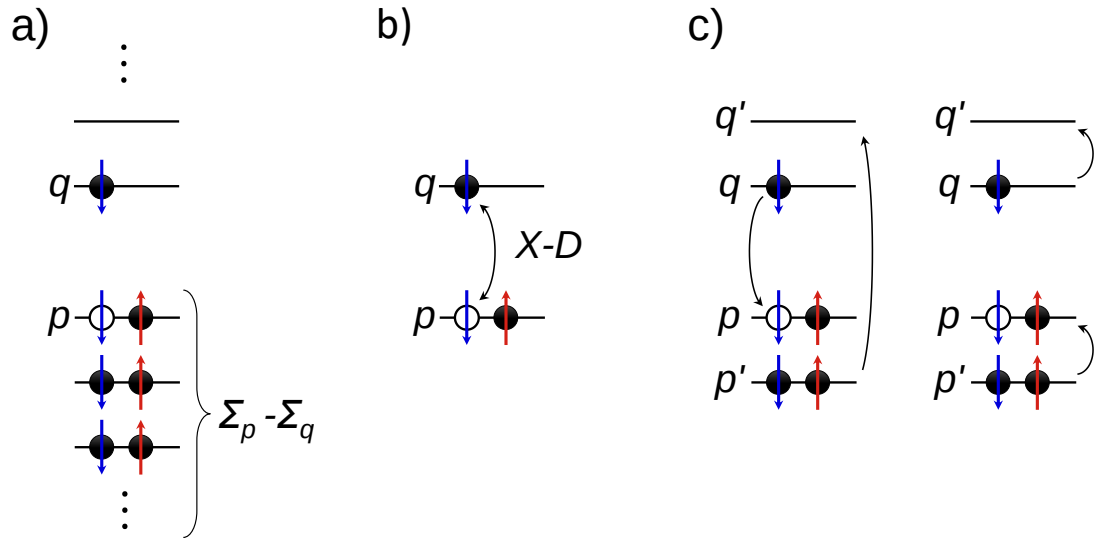

Figure 2.13: Schematic representation of different contributions to the BSE. In (a) is the self-energy contribution from the electron and hole. (b) shows the contribution of vertex correction where X represent electron-hole exchange interaction, while D represent e-h direct interaction. In (c) we show the two different ways electron-hole configurations can couple. The left side corresponds to a scattering due to a coulomb matrix element of the form $\langle p, q'|V_C|p', q\rangle$ while the right side of (c) corresponds to a scattering due to $\langle p, q'|V_C|q, p'\rangle$

We see that the electron-hole pair energy is renormalized by self-energy given by

$$\Sigma_p = -\sum_q \delta_{\sigma,\sigma'} \langle q, p|V_C|q, p\rangle \,, \tag{2.98}$$

where the sum over q runs over valence band states. Fig. 2.13(a) shows diagrammatically the contribution of self-energy to the energy of the electron-hole complex. The last two terms in Eq. 2.97 are our vertex corrections corresponding to electron-hole exchange, and direct interaction when $p = p'$ and $q = q'$. Vertex correction will also renormalize the electron-hole energy. Fig. 2.13(b) shows a diagram of the vertex correction contribution. When $p \neq p'$ and $q \neq q'$ then the last two terms in Eq. 2.97 correspond to scattering elements that couple different electron-hole configurations. Fig. 2.13(c) shows how these elements can scatter us from one electron-hole configuration to another.

2.3 Mean-field approximations

So far we have discussed non-interacting electron systems (single-particle), as well as full interacting many-body systems. In the previous section we outlined the computational complexity of the many-body problem as well as some approaches to solve these many-body problems mainly in a restricted basis. We now turn to an alternate method, mainly mean-field methods in order to try to understand the many-body ground state of the system.

2.3.1 Mean-field Hartree Fock

In this section we outline the Hartree-Fock (HF) method. We start with the many-body Hamiltonian defined in Eq. 2.67. We will move to a slightly different notation for convenience. Our Hamiltonian is given by

$$H = \sum_{p,\sigma} \epsilon_{p\sigma} c^\dagger_{p\sigma} c_{p\sigma} + \frac{1}{2} \sum_{p,q,r,s,\sigma,\sigma'} \langle p\sigma, q\sigma' | V | r\sigma', s\sigma \rangle \, c^\dagger_{p\sigma} c^\dagger_{q\sigma'} c_{r\sigma'} c_{s\sigma}, \tag{2.99}$$

where the indices p, q, r, s correspond to itinerant states. In the HF approximation, we assume that our wavefunction can be written as a single Slater determinant given by

$$|HF\rangle = \prod_\sigma \prod_\lambda^{\lambda^\sigma_F} \sum_p a_{\lambda,p,\sigma} c^\dagger_{p,\sigma} |0\rangle \,, \tag{2.100}$$

where λ are HF orbitals and λ^σ_F is the highest occupied state for spin σ. Since we may not have the same number of spin up and spin down electrons, we have a spin index included. Now let us define our HF operators as

$$b^\dagger_{\lambda,\sigma} = \sum_p a_{\lambda,p,\sigma} c^\dagger_{p,\sigma}. \tag{2.101}$$

The operators $b^{\dagger}_{\lambda,\sigma}$, $b^{\dagger}_{\lambda,\sigma}$ satisfy the Fermionic anticommutator relations defined in Eq. 2.58. Inverting the above expression, one obtains

$$c^{\dagger}_{p,\sigma} = \sum_{\lambda} a^{*}_{\lambda,p,\sigma} b^{\dagger}_{\lambda,\sigma}. \tag{2.102}$$

So, our HF ground state is

$$|HF\rangle = \prod_{\sigma} \prod_{\lambda}^{\lambda^{\sigma}_{F}} b^{\dagger}_{\lambda,\sigma} |0\rangle . \tag{2.103}$$

At this stage there are two ways to proceed. The formal way is by means of a Lagrange multiplier method in which we compute the energy of the HF state, and minimize the total energy with the constraint that we conserve the number of particles. This method is lengthy. For the sake of compactness we will proceed with a simplified method by starting with an ansatz which yields the same result [106]. This ansatz is what introduces the mean-field aspect of the approximation by replacing a two body operator by a one body operator. The ansatz is

$$\begin{aligned} c^{\dagger}_{p\sigma} c^{\dagger}_{q\sigma'} c_{r\sigma'} c_{s\sigma} \approx & \langle c^{\dagger}_{q\sigma'} c_{r\sigma'} \rangle c^{\dagger}_{p\sigma} c_{s\sigma} + \langle c^{\dagger}_{p\sigma} c_{s\sigma} \rangle c^{\dagger}_{q\sigma'} c_{r\sigma'} \\ & - \langle c^{\dagger}_{q\sigma'} c_{s\sigma} \rangle c^{\dagger}_{p\sigma} c_{r\sigma'} \delta_{\sigma\sigma'} - \langle c^{\dagger}_{p\sigma} c_{r\sigma'} \rangle c^{\dagger}_{q\sigma'} c_{s\sigma} \delta_{\sigma\sigma'}. \end{aligned} \tag{2.104}$$

Plugging this into Eq. 2.99 we get

$$\begin{aligned} H_{HF} = & \sum_{p,\sigma} \epsilon_{p\sigma} c^{\dagger}_{p\sigma} c_{p\sigma} \\ & + \frac{1}{2} \sum_{p,q,r,s,\sigma,\sigma'} \langle p\sigma, q\sigma' | V | r\sigma', s\sigma \rangle \langle c^{\dagger}_{q\sigma'} c_{r\sigma'} \rangle c^{\dagger}_{p\sigma} c_{s\sigma} \\ & + \frac{1}{2} \sum_{p,q,r,s,\sigma,\sigma'} \langle p\sigma, q\sigma' | V | r\sigma', s\sigma \rangle \langle c^{\dagger}_{p\sigma} c_{s\sigma} \rangle c^{\dagger}_{q\sigma'} c_{r\sigma'} \\ & - \frac{1}{2} \sum_{p,q,r,s,\sigma,\sigma'} \langle p\sigma, q\sigma' | V | r\sigma', s\sigma \rangle \langle c^{\dagger}_{q\sigma'} c_{s\sigma} \rangle c^{\dagger}_{p\sigma} c_{r\sigma'} \delta_{\sigma\sigma'} \\ & - \frac{1}{2} \sum_{p,q,r,s,\sigma,\sigma'} \langle p\sigma, q\sigma' | V | r\sigma', s\sigma \rangle \langle c^{\dagger}_{p\sigma} c_{r\sigma'} \rangle c^{\dagger}_{q\sigma'} c_{s\sigma} \delta_{\sigma\sigma'}. \end{aligned} \tag{2.105}$$

Relabelling indices and using symmetries of Coulomb matrix elements one obtains our HF equation:

$$H_{HF} = \sum_{p,\sigma} \epsilon_{p\sigma} c^{\dagger}_{p\sigma} c_{p\sigma} + \sum_{p,q,r,s,\sigma,\sigma'} \left[\langle p\sigma, q\sigma' | V | r\sigma', s\sigma \rangle - \langle p\sigma, q\sigma' | V | s\sigma, r\sigma' \rangle \, \delta_{\sigma\sigma'} \right] \langle c^{\dagger}_{q\sigma'} c_{r\sigma'} \rangle c^{\dagger}_{p\sigma} c_{s\sigma}, \tag{2.106}$$

where we note that this expression is in the itinerant basis. It is sometimes convenient to work in the localized basis. In this basis, the HF equation in the localized basis is:

$$\begin{aligned} H_{HF} = & \sum_{i,\sigma} \epsilon_{i\sigma} c^{\dagger}_{i\sigma} c_{i\sigma} - \sum_{i,j,\sigma} t_{il\sigma} c^{\dagger}_{i\sigma} c_{l\sigma} \\ & + \sum_{i,j,k,l,\sigma,\sigma'} \left[\langle i\sigma, j\sigma' | V | k\sigma', l\sigma \rangle - \langle i\sigma, j\sigma' | V | l\sigma, k\sigma' \rangle \, \delta_{\sigma\sigma'} \right] \langle c^{\dagger}_{j\sigma'} c_{k\sigma'} \rangle c^{\dagger}_{i\sigma} c_{l\sigma}, \end{aligned} \tag{2.107}$$

where the indices i, j, k,l now represent sites. This can be put in a simplified notation by defining

$$\tau_{il\sigma} = -t_{il\sigma} + \sum_{j,k,\sigma'} \left[\langle i\sigma, j\sigma' | V | k\sigma', l\sigma \rangle - \langle i\sigma, j\sigma' | V | l\sigma, k\sigma' \rangle \, \delta_{\sigma\sigma'} \right] \rho_{jk\sigma'}, \tag{2.108}$$

so that the HF equation becomes

$$H_{HF} = \sum_{i,\sigma} \epsilon_{i\sigma} c^{\dagger}_{i\sigma} c_{i\sigma} + \sum_{i,l,\sigma} \tau_{il\sigma} c^{\dagger}_{i\sigma} c_{l\sigma}. \tag{2.109}$$

$\rho_{jk\sigma'} = \langle c^{\dagger}_{j\sigma'} c_{k\sigma'} \rangle$ are called density matrix elements. Since our Hamiltonian must be diagonal in terms of operators $b_{\lambda,\sigma}$ we have

$$\sum_{i,\sigma} \epsilon_{i\sigma} c^{\dagger}_{i\sigma} c_{i\sigma} + \sum_{i,l,\sigma} \tau_{il\sigma} c^{\dagger}_{i\sigma} c_{l\sigma} = \sum_{\lambda,\sigma} \epsilon^{HF}_{\lambda,\sigma} b^{\dagger}_{\lambda,\sigma} b_{\lambda,\sigma}. \tag{2.110}$$

Averaging this expression over our HF GS we obtain

$$\sum_{i,\sigma} \epsilon_{i\sigma} \rho_{i,i,\sigma} + \sum_{i,l,\sigma} \tau_{il\sigma} \rho_{i,l,\sigma} = \sum_{\lambda,\sigma} \epsilon^{HF}_{\lambda,\sigma} n_{\lambda\sigma}. \tag{2.111}$$

We now proceed to compute these elements, we have

$$
\begin{aligned}
\rho_{jk\sigma'} &= \langle c^\dagger_{j\sigma'} c_{k\sigma'} \rangle = \langle HF | \, c^\dagger_{j\sigma'} c_{k\sigma'} \, | HF \rangle \\
&= \langle 0 | \prod_\sigma \prod_\lambda^{\lambda_F^\sigma} b_{\lambda,\sigma} c^\dagger_{j\sigma'} c_{k\sigma'} \prod_\sigma \prod_\lambda^{\lambda_F^\sigma} b^\dagger_{\lambda,\sigma} \, | 0 \rangle \\
&= \langle 0 | \prod_\sigma \prod_\lambda^{\lambda_F^\sigma} b_{\lambda,\sigma} \left(\sum_{\lambda'} a^*_{\lambda',j,\sigma'} b^\dagger_{\lambda',\sigma'} \right) \left(\sum_{\lambda''} a_{\lambda'',k,\sigma'} b_{\lambda'',\sigma'} \right) \prod_\sigma \prod_\lambda^{\lambda_F^\sigma} b^\dagger_{\lambda,\sigma} \, | 0 \rangle \\
&= \sum_{\lambda',\lambda''} a^*_{\lambda',j,\sigma'} a_{\lambda'',k,\sigma'} \prod_{\lambda,\sigma}^{\lambda_F^\sigma} \langle 0 | \, b_{\lambda,\sigma} b^\dagger_{\lambda',\sigma'} b_{\lambda'',\sigma'} b^\dagger_{\lambda,\sigma} \, | 0 \rangle \\
&= \sum_{\lambda',\lambda''} a^*_{\lambda',j,\sigma'} a_{\lambda'',k,\sigma'} \prod_{\lambda,\sigma}^{\lambda_F^\sigma} \delta_{\lambda'',\lambda'} \delta_{\lambda' \leq \lambda_F^\sigma} \\
&= \sum_\lambda a^*_{\lambda,j,\sigma'} a_{\lambda,k,\sigma'} n_{\lambda\sigma},
\end{aligned}
\tag{2.112}
$$

where $n_{\lambda\sigma}$ checks for occupation of state λ with spin σ. With the explicit form of the density matrix elements derived it becomes apparent that Eq. 2.109 must be solved self-consistently until we find an energy minimum. Thus, the last thing we need to compute is the HF energy, and track it at each iteration of our self-consistent calculation in order to ensure we found the minimum. We now proceed to compute

the HF energy. We have

$$
\begin{aligned}
E_{HF} &= \langle HF|\, H\, |HF\rangle = \sum_{i,\sigma} \epsilon_{i\sigma} \langle HF|\, c^\dagger_{i\sigma} c_{i\sigma}\, |HF\rangle \\
&+ \frac{1}{2} \sum_{i,j,k,l,\sigma,\sigma'} \langle i\sigma, j\sigma'|V|k\sigma', l\sigma\rangle \langle HF|\, c^\dagger_{i\sigma} c^\dagger_{j\sigma'} c_{k\sigma'} c_{l\sigma}\, |HF\rangle \\
&= \sum_{i,\sigma} \epsilon_{i\sigma} \langle HF|\, c^\dagger_{i\sigma} c_{i\sigma}\, |HF\rangle \\
&+ \frac{1}{2} \sum_{i,j,k,l,\sigma,\sigma'} \langle i\sigma, j\sigma'|V|k\sigma', l\sigma\rangle \langle HF|\, c^\dagger_{i\sigma} c_{l\sigma}\, |HF\rangle \langle HF|\, c^\dagger_{j\sigma'} c_{k\sigma'}\, |HF\rangle \\
&- \frac{1}{2} \sum_{i,j,k,l,\sigma,\sigma'} \langle i\sigma, j\sigma'|V|k\sigma', l\sigma\rangle \langle HF|\, c^\dagger_{i\sigma} c_{k\sigma'}\, |HF\rangle \langle HF|\, c^\dagger_{j\sigma'} c_{l\sigma}\, |HF\rangle \\
&= \sum_{i,\sigma} \epsilon_{i\sigma} \rho_{i,i,\sigma} \\
&+ \frac{1}{2} \sum_{i,j,k,l,\sigma,\sigma'} \left[\langle i\sigma, j\sigma'|V|k\sigma', l\sigma\rangle - \langle i\sigma, j\sigma'|V|l\sigma', k\sigma\rangle\right] \rho_{j,k,\sigma'} \rho_{i,l,\sigma} \\
&= \sum_{i,\sigma} \epsilon_{i\sigma} \rho_{i,i,\sigma} \\
&+ \sum_{i,j,k,l,\sigma,\sigma'} \left[\langle i\sigma, j\sigma'|V|k\sigma', l\sigma\rangle - \langle i\sigma, j\sigma'|V|l\sigma', k\sigma\rangle\right] \rho_{j,k,\sigma'} \rho_{i,l,\sigma} \\
&- \frac{1}{2} \sum_{i,j,k,l,\sigma,\sigma'} \left[\langle i\sigma, j\sigma'|V|k\sigma', l\sigma\rangle - \langle i\sigma, j\sigma'|V|l\sigma', k\sigma\rangle\right] \rho_{j,k,\sigma'} \rho_{i,l,\sigma},
\end{aligned}
\tag{2.113}
$$

where in the last equality we have added and subtracted the interaction term. Simplifying notation using Eq. 2.108 we get

$$
E_{HF} = \sum_{i,\sigma} \epsilon_{i\sigma} \rho_{i,i,\sigma} + \sum_{i,l,\sigma,} \tau_{il\sigma} \rho_{i,l,\sigma} - \frac{1}{2} \sum_{i,l,\sigma,} \tau_{il\sigma} \rho_{i,l,\sigma}. \tag{2.114}
$$

Using Eq. 2.111 this can be rewritten as

$$
E_{HF} = \sum_{\lambda,\sigma} \epsilon^{HF}_{\lambda\sigma} n_{\lambda\sigma} - \frac{1}{2} \sum_{i,l,\sigma} \tau_{il\sigma} \rho_{i,l,\sigma}. \tag{2.115}
$$

This is the HF energy. Notice that the HF energy is not only a sum over HF quasiparticle energies $\epsilon^{HF}_{\lambda\sigma}$, but also contains an extra term which arises due to the fact that interactions are contained in the HF quasiparticle levels. This energy must be

minimized in order for us to converge our HF GS self consistently.

2.3.2 Mean-field Hubbard model

The Mean-field HF Hamiltonian defined in Eq. 2.107 can be further reduced by making a Hubbard approximation described in 2.2.3. Retaining only onsite Hubbard U we obtain

$$H_{HF} = \sum_{i,\sigma} \epsilon_{i\sigma} c^{\dagger}_{i\sigma} c_{i\sigma} - \sum_{i,j,\sigma} t_{il\sigma} c^{\dagger}_{i\sigma} c_{l\sigma} + \sum_{i,\sigma,\sigma'} \left[\langle i\sigma, i\sigma' | V | i\sigma', i\sigma \rangle - \langle i\sigma, i\sigma' | V | i\sigma, i\sigma' \rangle \, \delta_{\sigma\sigma'} \right] \rho_{ii\sigma'} c^{\dagger}_{i\sigma} c_{l\sigma}. \tag{2.116}$$

Summing over spin indices in the interaction term we obtain

$$H_{HF} = \sum_{i,\sigma} \epsilon_{i\sigma} c^{\dagger}_{i\sigma} c_{i\sigma} - \sum_{i,j,\sigma} t_{il\sigma} c^{\dagger}_{i\sigma} c_{l\sigma} + U \sum_{i,\sigma,\sigma'} \left[\rho_{ii\downarrow} c^{\dagger}_{i\uparrow} c_{l\uparrow} + \rho_{ii\uparrow} c^{\dagger}_{i\downarrow} c_{l\downarrow} \right]. \tag{2.117}$$

Although the model is simplified, it can capture some essential physics. For example on a honeycomb lattice, this Hamiltonian can predict the phase of the GS as a function of U/t. When U/t is small we are in a metallic phase, when it is large we are in an AF phase [81] as we will show in chapter 4.

2.4 Tight-Binding - Hartree Fock - Configuration Interaction Method

In this section, we will combine the methodology of TB-HF-CI in order to solve correlated electron problems. Using HF allows us to start with an optimized basis to perform exact many-body calculations. We begin by solving the TB Hamiltonian as an initial guess into the self-consistent HF equation Eq. 2.109. Then by self consistently solving the HF equation we obtain a set of HF quasiparticle states. We then rotate our many-body Hamiltonian to the basis of HF states. Finally, we use CI to solve the many-body Hamiltonian thus accounting for correlations ignored at the

HF level. We have already covered the TB-HF part of this methodology. To complete it, we will rotate the many-body Hamiltonian in Eq. 2.67 to the basis of HF states. Rewriting our Hamiltonian defined in Eq. 2.67, we have

$$H = \sum_{i,\sigma} \epsilon_{i\sigma} c^\dagger_{i\sigma} c_{i\sigma} + \frac{1}{2} \sum_{i,j,k,l,\sigma,\sigma'} \langle ijV|kl\rangle \, c^\dagger_{i\sigma} c^\dagger_{j\sigma'} c_{k\sigma'} c_{l\sigma}, \tag{2.118}$$

where spin indices are hidden in the Coulomb matrix elements and the indices i, j, k, l now correspond to itinerant states. Starting with transforming only the single-particle part of the Hamiltonian and using Eq. 2.110 we get

$$\sum_{i,\sigma} \epsilon_{i\sigma} c^\dagger_{i\sigma} c_{i\sigma} = \sum_{p,\sigma} \epsilon^{HF}_{p,\sigma} b^\dagger_{p,\sigma} b_{p,\sigma} - \sum_{i,l,\sigma} \tau_{il\sigma} c^\dagger_{i\sigma} c_{l\sigma}. \tag{2.119}$$

Recalling Eq. 2.102 we have

$$\begin{aligned} \sum_{i,\sigma} \epsilon_{i\sigma} c^\dagger_{i\sigma} c_{i\sigma} &= \sum_{p,\sigma} \epsilon^{HF}_{p,\sigma} b^\dagger_{p,\sigma} b_{p,\sigma} - \sum_{p,q} \sum_{i,l,\sigma} a^*_{p,i,\sigma} a_{q,l,\sigma} \tau_{il\sigma} b^\dagger_{p,\sigma} b_{q,\sigma} \\ &= \sum_{p,\sigma} \epsilon^{HF}_{p,\sigma} b^\dagger_{p,\sigma} b_{p,\sigma} - \sum_{p,q,\sigma} t_{pq\sigma} b^\dagger_{p,\sigma} b_{q,\sigma}, \end{aligned} \tag{2.120}$$

where

$$t_{pq\sigma} = \sum_{i,l} a^*_{p,i,\sigma} a_{q,l,\sigma} \tau_{il\sigma}. \tag{2.121}$$

Its worth noting that $\tau_{il\sigma}$ does not contain the hopping term in its definition because we are in an itinerant basis. Now, let us transform the interaction part, let's call it V for simplicity. We have

$$\begin{aligned} V &= \frac{1}{2} \sum_{p,q,r,s} \sum_{i,j,k,l,\sigma,\sigma'} a^*_{p,i,\sigma} a^*_{q,j,\sigma'} a_{r,k,\sigma'} a_{s,l,\sigma} \, \langle ij|V|kl\rangle \, b^\dagger_{p\sigma} b^\dagger_{q\sigma'} b_{r\sigma'} b_{s\sigma} \\ &= \frac{1}{2} \sum_{p,q,r,s,\sigma,\sigma'} \langle pq|V|rs\rangle \, b^\dagger_{p\sigma} b^\dagger_{q\sigma'} b_{r\sigma'} b_{s\sigma}, \end{aligned} \tag{2.122}$$

where

$$\langle pq|V|rs\rangle = \sum_{i,j,k,l} a^*_{p,i,\sigma} a^*_{q,j,\sigma'} a_{r,k,\sigma'} a_{s,l,\sigma} \, \langle ij|V|kl\rangle \, . \tag{2.123}$$

Combining everything our many-body Hamiltonian in the basis of HF states is given by

$$H = \sum_{p,\sigma} \epsilon^{HF}_{p,\sigma} b^\dagger_{p,\sigma} b_{p,\sigma} - \sum_{p,q,\sigma} t_{pq\sigma} b^\dagger_{p,\sigma} b_{q,\sigma} + \frac{1}{2} \sum_{p,q,r,s,\sigma,\sigma'} \langle pq|V|rs\rangle \, b^\dagger_{p\sigma} b^\dagger_{q\sigma'} b_{r\sigma'} b_{s\sigma}. \quad (2.124)$$

It is worth noting the emergence of the term $t_{pq\sigma}$ which arises to ensure we are not over-counting interactions that were contained in the mean-field interactions.

2.5 Numerical methods

In this thesis, codes were developed using various programming languages, including C, C++, Python, and Matlab. C and C++ were primarily used, and Python or Matlab were used when it was more convenient for a particular task.

One of the challenges faced during tackling problems in this thesis were the numerical complexity of the many-body problem, which can grow factorially with the number of states and number of electrons. For example, the large Hilbert spaces often require the diagonalization of very large matrices, which can be computationally demanding. Additionally, the data organization in these calculations must be carefully managed to avoid overwhelming the memory of the computer.

To address these challenges, we used the SlepC library [107], which is a library that is being used inside of QNANO. QNANO is a package developed by researchers at the University of Ottawa. Through QNANO, I am able to use SlepC. This library allowed me to perform diagonalization of large matrices in a computationally efficient manner by using a compressed sparse row (CSR) format. SlepC uses projection methods which involve projecting the matrix onto a lower-dimensional subspace and iteratively computing approximations of its eigenvectors and eigenvalues.

Another important aspect of the work done in this thesis was the calculation of Coulomb matrix elements. In general, computing a single Coulomb matrix element requires solving a 6-dimensional integral, as seen in Eq. 2.68. There are N^4 of these matrix elements, which can be computationally demanding. To simplify the calcula-

tion, we exploited the fact that the wavefunctions were localized on sites and made a long-range approximation which replaces the electron density by delta functions effectively treating the charges as point charges. This approximation reduced the number of 6-dimensional Coulomb matrix elements that needed to be calculated, but we still needed a way to efficiently solve the remaining short-range Coulomb matrix elements.

In addition to the calculation of Coulomb matrix elements, we also needed to rotate these matrix elements from a site representation to a single-particle basis. This process is of $O(N^4)$ for each matrix element and required optimization to ensure that it was performed efficiently.

Overall, the development of these codes and the use of specialized libraries were essential for addressing the numerical complexity of many-body systems and performing the calculations required for the thesis.

2.5.1 VEGAS algorthim

The VEGAS algorithm is a Monte Carlo [108] method for numerical integration that can be used to compute integrals of the form:

$$I = \int_{\Omega} f(\mathbf{x}) d\mathbf{x} \tag{2.125}$$

where $f(\mathbf{x})$ is the function to be integrated and Ω is the domain of integration. The VEGAS algorithm is an adaptive algorithm, which means that it adjusts its behavior based on the results of previous iterations in order to improve the accuracy of the final result.

The VEGAS algorithm works by dividing the domain of integration Ω into a grid of bins, and then estimating the integral by randomly sampling points from each bin and evaluating the function at those points. The algorithm then uses the results of these samples to refine the grid and improve the accuracy of the final result.

The VEGAS algorithm can be generalized to higher dimensions, such as the

6-dimensional case. In this case, the domain of integration is divided into a 6-dimensional grid of bins, and the algorithm proceeds as before by sampling points from each bin and using the results to refine the grid.

One of the key advantages of the VEGAS algorithm is that it can handle highly oscillatory functions, which can be difficult for other numerical integration methods to accurately approximate. Additionally, the VEGAS algorithm is relatively easy to implement and can be parallelized, making it a useful tool for solving a wide range of integration problems.

For calculations in this thesis we use the VEGAS algorthim implemented in the gsl library [109].

2.5.2 Calculation of Coulomb matrix elements

In most of this thesis, we compute Coulomb matrix elements starting in the localized basis and rotate them to the itinerant basis. We compute Coulomb matrix elements in the localized basis using a VEGAS algorthim described above. This was used to compute matrix elements in the site representation for graphene, bilayer graphene and artificial graphene. For graphene, taking p_z Slater orbitals centered on atom i of the form

$$\phi_i(\vec{r}) = \left(\frac{\xi^5}{32\pi}\right)^{\frac{1}{2}} (z - z_i)\, e^{-\frac{\xi}{2}|\vec{r}-\vec{r}_i|} \tag{2.126}$$

where ξ is the Slater parameter which we take to be $\xi = 3.25$ [88], we then proceed to compute the Coulomb matrix elements defined in Eq. 2.68 using distances measured in units of Bohrs radii $a_b = 0.52917721092\ \mathring{A}$ with $R_y = 13.6056930$ eV. Table. 2.1 shows the Coulomb matrix elements for a single sheet of graphene. There is a comparison with the numbers contained in recent review [1], but we note that there is a difference in the choice of the Slater parameter ξ. The labelling of sites 1, 2, 3 means if numbers differ by 1 they are NN to each other, if they differ by 2 they are next nearest neighbours (NNNs) to each other. The table contains all scattering terms up to NNN.

It is worth noting that if we consider scattering terms that involve scatterings

Matrix Element	VEGAS (eV) $\xi = 3.25$	Graphene QD book (eV) $\xi = 3.14$
$\langle 11\|V\|11\rangle$	17.307	16.522
$\langle 12\|V\|21\rangle$	8.942	8.640
$\langle 13\|V\|31\rangle$	5.582	5.333
$\langle 11\|V\|12\rangle$	3.027	3.157
$\langle 12\|V\|31\rangle$	1.664	1.735
$\langle 12\|V\|12\rangle$	0.774	0.873
$\langle 11\|V\|22\rangle$	0.774	0.873
$\langle 22\|V\|13\rangle$	0.535	0.606
$\langle 12\|V\|23\rangle$	0.356	–
$\langle 11\|V\|13\rangle$	0.306	–

Table 2.1: Coulomb matrix elements for graphene using p_z Slater orbitals. The first column corresponds to the element we are referring to, the second column corresponds to the elements calculated using the VEGAS algorithm, we take the Slater parameter $\xi = 3.25$. The last column are calculated values in the graphene QDs book [1] for $\xi = 3.14$.

between atoms that are further than the NNN distance in graphene the Coulomb matrix elements $\langle ij|V|kl\rangle$ become negligible unless $j = k$ and $i = l$, corresponding to direct terms. Thus, we restrict ourselves to only the direct terms now. The direct terms have the form

$$\langle ij|V|ji\rangle = R_y \int\int d\vec{r}_1 d\vec{r}_2 |\psi_i(\vec{r}_1)|^2 |\psi_j(\vec{r}_2)|^2 \frac{2}{|\vec{r}_1 - \vec{r}_2|}, \tag{2.127}$$

where $|\psi_i(\vec{r}_1)|^2$ is the electron density on site i. It is still cumbersome to compute all these direct terms especially for large systems. We can perform a long-range approximation if the distance between site i and site j is sufficiently large, such that we approximate the electrons as point charges by replacing the density with a delta function. In other words we have

$$\langle ij|V|ji\rangle = \int\int d\vec{r}_1 d\vec{r}_2 \delta\left(\vec{r_1} - \vec{R}_i\right) \delta\left(\vec{r_2} - \vec{R}_j\right) \frac{2R_y}{|\vec{r}_1 - \vec{r}_2|}, \tag{2.128}$$

executing the delta functions we get

$$\langle ij|V|ji\rangle = \frac{2R_y}{|\vec{R}_i - \vec{R}_j|}. \tag{2.129}$$

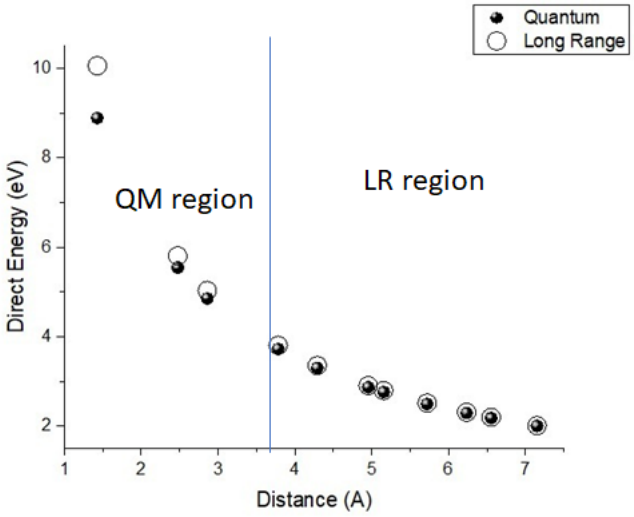

Figure 2.14: Comparing the long range approximation of Coulomb matrix elements with quantum mechanical Coulomb matrix elements. The x-axis denotes distances between atoms, it is separated into two regions, one where the long range approximation is valid, and the other where we take the quantum mechanical matrix element.

Fig. 2.14 shows the validity of this long range approximation. It is sufficient to compute the direct elements for distances less than about $3.5\mathring{A}$ and otherwise take a long-range approximation which reduces the 6-dimensional integral to a single function and thus reducing the numerical complexity tremendously.

Now that we have computed Coulomb matrix elements in the site representation, it is convenient to work in the itinerant basis instead of the localized basis in order to prevent the Hilbert space in many-body calculations from getting unmanageable. The advantage of the itinerant basis, is that we can ignore states that are far away from the Fermi level when attempting to find the low energy many-body states of the system. This is because configurations that are far away energetically tend to couple weakly. We will continue to work on the example of graphene as we have implemented this methodology for graphene, although it is extendable to other materials. The method outlined here is also consistent with what has been used in Refs. 110–112. The new Coulomb matrix elements we seek to obtain are defined in Eq. 2.69 but we limit ourselves to the single p_z orbital and we have

$$\langle pq|V|rs\rangle = \sum_{i,j,k,l} \left(C_i^p\right)^* \left(C_j^q\right)^* C_k^r C_l^s \langle ij|V|kl\rangle \,. \tag{2.130}$$

Just to give the context of the numerical complexity of this rotation, later in the thesis we will work on a bilayer graphene quantum dot in which the number of sites is 1.6 million. This summation over i, j, k, l would correspond to a sum over 10^{24} terms! Of course, only the non-zero Coulomb matrix elements need to be summed over. Thus the true numerical complexity is contained in the long range part of this expression. Let's focus on only the long range contribution to this summation, we have

$$\begin{aligned}\langle pq|V_{LR}|rs\rangle &= \sum_{i,j} \left(C_i^p\right)^* \left(C_j^q\right)^* C_i^r C_i^s \frac{2R_y}{|\vec{R}_i - \vec{R}_j|} \\ &= \sum_{i,j} \left(C_i^p\right)^* \left(C_j^q\right)^* C_i^r C_i^s V\left(\vec{R}_i - \vec{R}_j\right).\end{aligned} \tag{2.131}$$

Even this reduction is now a process of $O(N^2)$ which for the system we will work on later of 1.6 million atoms still corresponds to a sum over 10^{14} terms. Furthermore, this is only for a single Coulomb matrix element. In general, for a basis of 32 itinerant states there would be 1048576 of these terms to compute. So we need to further simplify the problem. Now let us define the following matrix [110–112]

$$F^{ps} = \sum_i F_i^{ps} = \sum_i C_i^{p*} C_i^s, \tag{2.132}$$

then we can write our LR contribution in the form

$$\langle pq|V_{LR}|rs\rangle = \sum_{i,j} F_i^{ps} F_j^{qr} V\left(\vec{R}_i - \vec{R}_j\right). \tag{2.133}$$

But Coulomb interaction depends only on the magnitude of the distance between atom i and atom j and if we exploit this fact, the numerical complexity is now less than $O(N^2)$. To minimize repeated multiplicative operations in this summation, we

can define a new data structure

$$G_i^{qr} = \sum_j F_j^{qr} V\left(\vec{R}_i - \vec{R}_j\right), \tag{2.134}$$

then we must compute

$$\langle pq|V_{LR}|rs\rangle = \sum_i F_i^{ps} G_i^{qr}. \tag{2.135}$$

The most numerically expensive part to compute is G_i^{qr} but for computing a single G vector for a fixed q, r we can compute matrix elements for any p, s with numerical complexity $O(N)$ which is very fast even for large numbers of atoms! This method will be implemented for problems described in chapter 6 and 7. It is worth noting that the short range part is numerically inexpensive since once we have the short-range Coulomb matrix elements computed there is only a small number of these elements that are non-zero that need to be summed over.

Chapter 3

Oscillations of the Bandgap in Hexagonal Graphene Quantum Dots

We would like to state this chapter is based on Ref. [113] with more derivations and detail shown. I have done all calculations in this paper except the DFT calculations.

In this chapter we determine the evolution of the bandgap energy with size in graphene quantum dots (GQDs). We find oscillatory behaviour of the bandgap and explain its origin in terms of armchair and zigzag edges. The electronic energy spectra of GQDs are computed using both the TB model and ab initio density functional methods. The results with zigzag edges of the TB model are analyzed by dividing zigzag graphene quantum dots (GQDs) into concentric rings. For each ring, the energy spectra, the wavefunctions and the bandgap are obtained analytically. The effect of inter-ring tunneling on the energy gap is determined. The growth of zigzag-terminated GQD into armchair GQD is shown to be associated with the addition of a one-dimensional Lieb lattice of carbon atoms with a shell of energy levels in the middle of the energy gap of the inner zigzag-terminated GQD. This introduces a different structure of the energy levels at the bottom of the conduction and top of the valence band in zigzag and armchair GQD which manifests itself in the oscillation of

the energy gap with increasing size. The evolution of the bandgap with the number of carbon atoms is compared with the notion of confined Dirac Fermions and tested against ab initio calculations of Kohn–Sham and time-dependent density functional theory (TD-DFT) energy gaps.

3.1 Tight-binding model of a zigzag graphene quantum dot

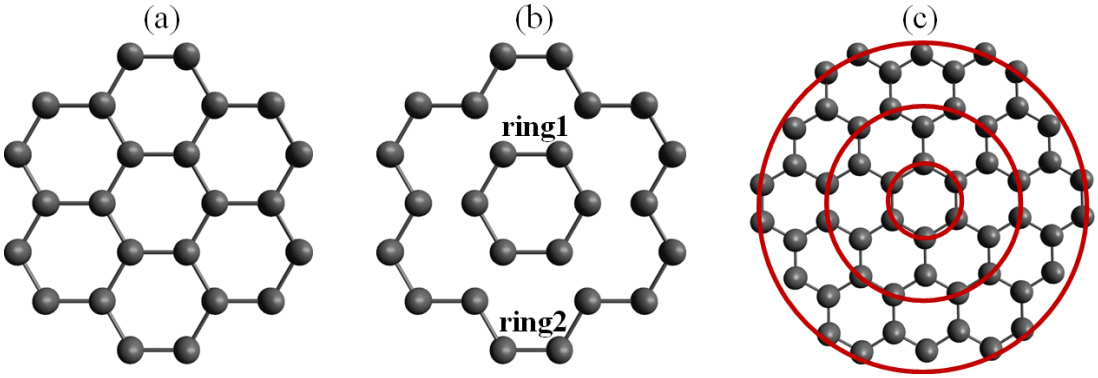

Figure 3.1: Decomposition of graphene quantum dot C24 into concentric rings. Grey spheres represent carbon atoms and connecting lines indicate electron tunneling between atoms. (a) C24 (coronene), (b) C24, with tunneling between ring1 and ring 2 turned off. (c) C54 with three rings as indicated by red circles.

We now define our model and introduce our procedure of dividing GQD into concentric rings on the example of a small GQD. Fig. 3.1(a) shows schematically the position of carbon atoms in the smallest graphene quantum dot, C24, with zigzag edges (coronene), composed of 24 Carbon (C24) and 12 hydrogen atoms (hydrogen atoms not shown in figure). We assume the structure as shown in figure. 3.1, verify it by DFT and retain one p_z electron per carbon atom. We neglect hydrogen atoms and with each ball in Fig. 3.1 we represent a single p_z orbital, while the 'stick' represents the matrix element t for tunneling between nearest neighbor p_z orbitals. The one-electron Hamiltonian is given by

$$\hat{\mathbf{H}} = t \sum_{\langle i,j\rangle,\sigma} c^{\dagger}_{i\sigma} c_{j\sigma}, \tag{3.1}$$

and describes tunneling of a p_z electron from a carbon atom j to its nearest neighbors i with amplitude t. We note t is negative. In the first step we divide our GQD into two rings, the inner ring of six C atoms (benzene) and the outer ring of 18 C atoms. We first set the tunneling matrix elements τ between the two rings to zero, as illustrated in Fig. 3.1(b). Fig. 3.1(c) shows a similar division of a larger GQD with 54 C atoms (C54) and a zigzag edge into three rings. The Hamiltonian of C24 can now be written as

$$\hat{H} = \hat{H}_{ring1} + \hat{H}_{ring2} + \hat{V}_{12}. \tag{3.2}$$

Neglecting the coupling $\hat{V}_{12}$ between the rings, the wavefunctions and energy levels of inner ring (ring 1) and outer ring (ring 2) can be written explicitly,

$$\psi_k^{ring} = \frac{1}{\sqrt{N}} \sum_{n=1}^{N} e^{ikan} \phi_n \left(\vec{r}\right), \tag{3.3}$$

where $\phi_n \left(\vec{r}\right)$ is a p_z orbital centered on atom n, $k = \frac{2\pi}{Na} p$, with $p = 0, \pm 1, \pm 2, ...$, and a is the bond length. We have $N = 18$ for ring 2, and $N = 6$ for ring 1. The energies are given by

$$E_{ring} = 2t \cos\left(ka\right). \tag{3.4}$$

The highest filled energy level is

$$E_{ring}^{\nu} = 2t \cos\left(\frac{2\pi}{N} \frac{\frac{N}{2} - 1}{2}\right). \tag{3.5}$$

Because we have electron-hole symmetry, the energy gap is just

$$\Delta_{ring} = \left| 4t \cos\left(\frac{2\pi}{N} \frac{\frac{N}{2} - 1}{2}\right) \right|. \tag{3.6}$$

When N becomes sufficiently large, this can be approximated as

$$\Delta_{ring} \approx \frac{4t\pi}{N}. \tag{3.7}$$

We see that the energy gap decreases inversely proportional to the circumference of

the ring $N \times a$ or radius of the ring R. The scaling of the gap of a 1D ring with N atoms is similar to the scaling of the gap defined by the confined Dirac Fermion model [98]. Let us now turn on electronic coupling $\hat{V}_{12}$ of outer and inner rings. The matrix elements of $\hat{V}_{12}$ coupling ring 1 and ring 2 are given by

$$\langle \psi_k^{ring2} | \hat{V}_{12} | \psi_q^{ring1} \rangle = \frac{1}{\sqrt{18 \cdot 6}} \sum_{n'=1}^{N_{ring2}} \sum_{n=1}^{N_{ring1}} e^{-ikan'} e^{iqan} \langle \phi_{n'} | \hat{V}_{12} | \phi_{n'} \rangle . \tag{3.8}$$

Since we are in a NN approximation, the coupling of $\hat{V}_{12}$ couples each atom in the inner ring 1 only to every third atom of the outer ring 2 (see Fig. 3.1(b)). Thus if we enumerate atoms correctly, this corresponds to $n = 3n'$ with amplitude τ, so we have

$$\langle \psi_k^{ring2} | \hat{V}_{12} | \psi_q^{ring1} \rangle = \frac{\tau}{\sqrt{18 \cdot 6}} \sum_{n'=1}^{N_{ring2}} \sum_{n=1}^{N_{ring1}} e^{-ikan'} e^{iqan} \delta_{n,3n'}, \tag{3.9}$$

executing the delta we get

$$\langle \psi_k^{ring2} | \hat{V}_{12} | \psi_q^{ring1} \rangle = \frac{\tau}{\sqrt{18 \cdot 6}} \sum_{n=1}^{N_{ring1}} e^{i(q-3k)an}. \tag{3.10}$$

We see that the matrix elements couple each single state 'q' of the inner ring with three 'k' states of the outer ring according to the selection rule $3k = q, q + Q, q - Q$ where the $Q = \frac{2\pi}{a}$ corresponds to the reciprocal lattice vector. Let $k_\nu = \frac{2\pi}{Na}\left(\frac{\frac{N}{2}-1}{2}\right)$ be the wavevector corresponding to the highest occupied state of the outer ring. From Eq. 3.10 we see that only three states q, $k_\nu + \frac{Q}{3}$, $k_\nu - \frac{Q}{3}$ couple with k_ν, where $q = 3k_\nu$. In order to obtain the energy of the top valence state we need to diagonalize only a 4×4 matrix. Instead of diagonalizing the full tunnelling $N \times N$ Hamiltonian of two rings with $N = 24$ we brought the Hamiltonian matrix to a diagonal form of blocks of 4×4 size each, which we need to diagonalize separately. The same process extends to larger rings. We can write explicitly the 4×4 Hamiltonian for the q, k_ν, $k_\nu + \frac{Q}{3}$

and $k_\nu - \frac{Q}{3}$ coupled levels as a function of the inter-ring coupling τ as

$$H = \begin{pmatrix} -t & \frac{\tau}{\sqrt{3}} & \frac{\tau}{\sqrt{3}} & \frac{\tau}{\sqrt{3}} \\ \frac{\tau}{\sqrt{3}} & 0.347t & 0 & 0 \\ \frac{\tau}{\sqrt{3}} & 0 & 1.532t & 0 \\ \frac{\tau}{\sqrt{3}} & 0 & 0 & 1.879t \end{pmatrix}. \tag{3.11}$$

The upper corner of the matrix describes coupling of the top of the valence band

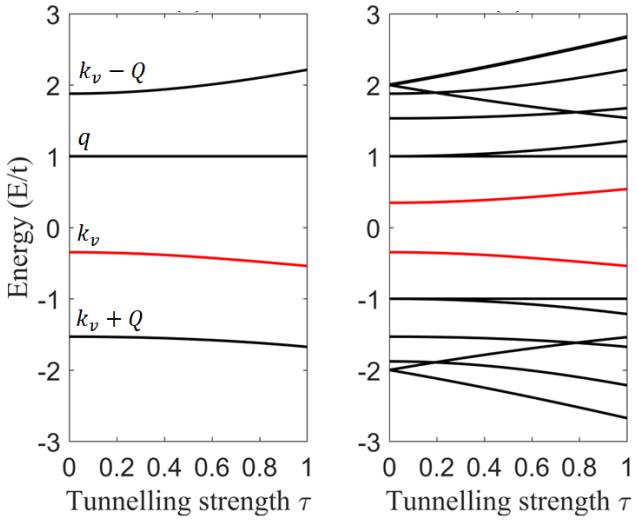

Figure 3.2: (a) Evolution of the q, k_ν, $k_\nu + \frac{Q}{3}$ and $k_\nu - \frac{Q}{3}$ states with the inter-ring tunneling strength τ in units of t. The red line shows evolution of the top valence state. (b) Evolution of the four groups of energy states, with the top of the valence, and bottom of conduction band plotted in red.

state k_ν of the outer ring with energy $0.3472t$ with the bottom of the conduction band state of the inner ring q with energy $-t$. The two remaining states of the outer ring, $k_\nu + \frac{Q}{3}$ and $k_\nu - \frac{Q}{3}$, provide additional indirect contribution to state k_ν by indirect coupling via the state q of the inner ring. We also note that the effective inter-ring tunneling is reduced, from τ to $\frac{\tau}{\sqrt{3}}$. Fig. 3.2(a) shows the evolution of the four energy levels q, k_ν, $k_\nu + \frac{Q}{3}$ and $k_\nu - \frac{Q}{3}$ as a function of the coupling strength τ illustrating the renormalization of the energy of the top of the valence band. Due to electron-hole symmetry this analysis also determines the renormalization of the bottom of the conduction band and hence, the energy gap of C24. The evolution of all four groups of energy levels (two groups are degenerate) with inter-ring tunneling τ, including

top of the valence band and bottom of the conduction band, is shown in Fig. 3.2(b). The inter-ring coupling renormalizes the energy gap and changes its dependence on the number of carbon atoms but the degeneracy of the conduction band minimum and valence band maximum remains.

3.2 Tight-binding model of an armchair graphene quantum dot

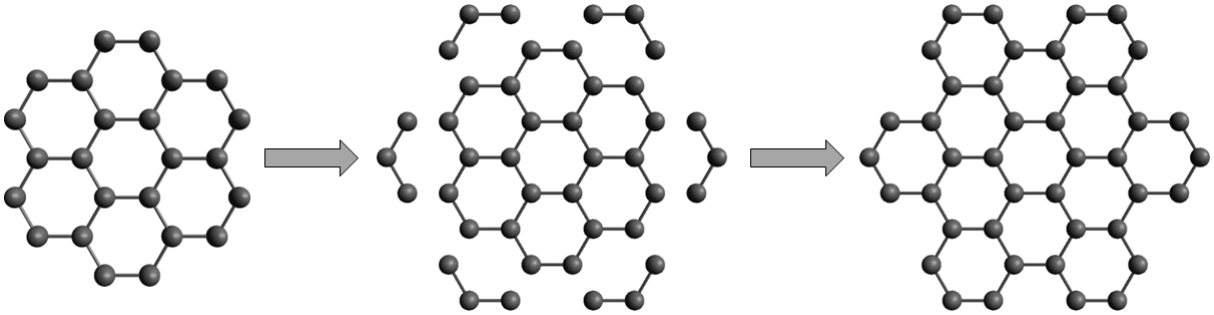

Figure 3.3: Schematic illustration of increasing the size of the GQD from C24 with zigzag edge to C42 with armchair edge by adding six Lieb clusters of three carbon atoms each.

Let us now focus on increasing the number of carbon atoms. Fig. 3.3 shows how a graphene quantum dot can be grown from C24 to C42 by addition of a third, incomplete ring of 18 carbon atoms. When completed, the final GQD corresponds to the smallest hexagonal GQD with an armchair edge. By looking at the added outer ring, central panel in Fig. 3.3, we see that the outer, third, ring is built of six disconnected groups with three carbon atoms each. Each group of three carbon atoms is next connected to the outer ring of the smaller, zigzag GQD, as seen in the right panel of Fig. 3.3. In this example, the outer ring forms a 1D Lieb lattice [78], a lattice with unit cell containing three atoms. The special property of the Lieb lattice is the existence of a shell of energy levels at zero-energy. We can show this by diagonalizing

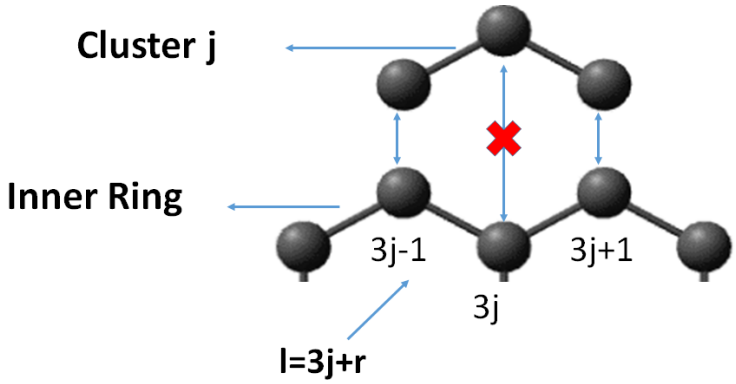

Figure 3.4: Defining the geometry of the cluster, and showing the non-zero hopping matrix elements between ring 2 and ring 3.

Eq. 3.1. The Hamiltonian for a single cluster is explicitly given by

$$H = \begin{pmatrix} 0 & t & 0 \\ t & 0 & t \\ 0 & t & 0 \end{pmatrix}. \tag{3.12}$$

This gives energies $E_- = -\sqrt{2}|t|$, $E_0 = 0$, $E_+ = \sqrt{2}|t|$ which is shown in Fig. 3.5 (c) as green lines. We indeed find a zero energy level for each of the six clusters and hence a six-fold degenerate shell at the zero-energy. This shell is in the middle of the gap of the inner C24 GQD, shown in Fig. 3.5 (c). Each of the zero energy levels corresponds to a state $\frac{1}{\sqrt{2}}(\phi_1 - \phi_3)$, i.e., a state built of orbitals on atoms one and three, but not middle atom two. The six states at zero-energy of the outer ring are analogous to the six states of the inner ring, benzene, in our previous analysis of C24 GQD. We follow the same methodology here by constructing itinerant states of the six clusters. We start by analyzing the interaction of the zero-energy shell with the outer ring of C24. We form the itinerant states of the outer third ring using zero energy states as

$$\psi_k^{ring3}(\vec{r}) = \frac{1}{\sqrt{6}} \sum_{j=0}^{5} e^{ik5aj} \frac{1}{\sqrt{2}} \left(\phi_{3j-1}(\vec{r}) - \phi_{3j+1}(\vec{r})\right), \tag{3.13}$$

where the labelling of atoms is shown in Fig. 3.4. We now derive the coupling matrix

element between the outer clusters (ring 3) and the inner ring 2

$$\begin{aligned}
\langle\psi_k^{ring2}|\hat{V}_{23}|\psi_q^{ring3}\rangle &= \frac{1}{\sqrt{2\cdot 18\cdot 6}}\sum_{n=0}^{17}\sum_{j=0}^{5} e^{-ikan}e^{i5qaj}\,\langle\phi_n|\hat{V}_{12}|\,(\phi_{3j-1}-\phi_{3j+1})\rangle \\
&= \frac{1}{\sqrt{2\cdot 18\cdot 6}}\sum_{n=0}^{17}\sum_{j=0}^{5} e^{i(5qj-kn)a}\left(\langle\phi_n|\hat{V}_{12}|\phi_{3j-1}\rangle-\langle\phi_n|\hat{V}_{12}|\phi_{3j+1}\rangle\right) \\
&= \frac{\tau}{\sqrt{2\cdot 18\cdot 6}}\sum_{n=0}^{17}\sum_{j=0}^{5} e^{i(5qj-kn)a}\left(\delta_{n,3j-1}-\delta_{n,3j+1}\right) \\
&= \frac{\tau}{\sqrt{18\cdot 6}}\sum_{j=0}^{5}\left(e^{i(5qj-k(3j-1))a}-e^{i(5qj-k(3j+1))a}\right) \\
&= \frac{\tau}{\sqrt{2\cdot 18\cdot 6}}\sum_{j=0}^{5} e^{i(5q-3k)ja}\left(e^{ika}-e^{-ika}\right) \\
&= \frac{2i\tau\sin ka}{\sqrt{2\cdot 18\cdot 6}}\sum_{j=0}^{5} e^{i(5q-3k)ja}
\end{aligned} \tag{3.14}$$

Using the definitions of q and k we can write this as

$$\langle\psi_k^{ring2}|\hat{V}_{23}|\psi_q^{ring3}\rangle = \frac{2\cdot 6i\tau\sin ka}{\sqrt{2\cdot 18\cdot 6}}\delta_{5q\pm Q,3k} = \frac{2i\tau\sin ka}{\sqrt{6}}\delta_{5q\pm Q,3k}. \tag{3.15}$$

We see that the selection rules are modified compared with C24, with $3k = 5q$, $5q - Q$, $5q + Q$. and the matrix element, Eq. 3.15, is modified due to the nature of the zero-energy Lieb orbital $\frac{1}{\sqrt{2}}(\phi_1 - \phi_3)$, a combination of orbitals one and three of each group of outer carbon atoms. Fig. 3.5(c) shows the energy levels of the inner QD, C24, and three shells of energy levels of the outer Lieb ring of 18 carbon atoms.

We see that there are indeed six states at zero-energy which are in the middle of the energy gap of the inner GQD, Fig. 3.5(c). We now proceed with the same methodology as for C24. We construct exact eigenstates of the outer ring 3 out of the states of the Lieb lattice. The eigenstates of the inner ring 1 and inner ring 2 were discussed already. With the inner-outer ring tunneling matrix elements due to $\hat{V}_{23}$ computed in Eq. 3.15, we can diagonalize the Hamiltonian resulting in the energy spectrum shown in Fig. 3.5(d). This energy spectrum includes also coupling with the

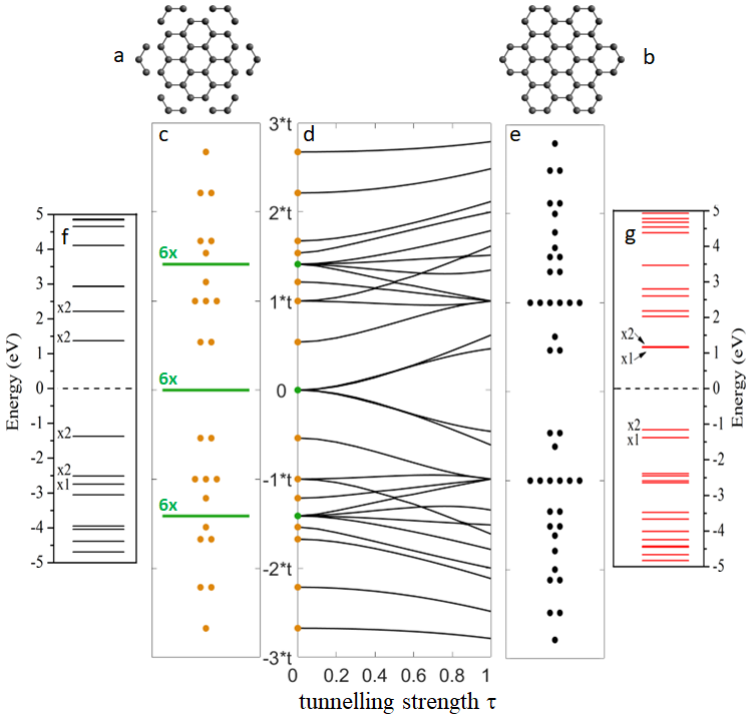

Figure 3.5: Structure and energy spectrum of C24 GQD with zigzag edges ((a) and (c)) and Lieb ring of 18 Carbon atoms evolving into C42 GQD with armchair edges ((b) and (e)) when τ is turned on (evolution shown in subplot (d)). The degeneracy of states in the vicinity of the Fermi level is shown explicitly. The matrix element τ couples p_z orbitals of the Lieb ring with C24 GQD. Kohn–Sham spectra of C24 and C42 GQDs are shown respectively in (f) and (g).

inner benzene ring. We see that the degeneracy of the zero-energy Lieb shell is lifted, an energy gap opens up across the Fermi level and the bottom of the conduction band and the top of the valence band originates from the zero-energy Lieb shell. Since there are six states in this shell the bottom of CB consists of three states and the top of the valence band consists of three states. There is a small splitting of the three states, but the splitting is small compared to the energy gap to the higher (lower) energy levels. The two states at the top of the VB of the zigzag GQD and three states of the armchair GQD are reproduced by ab intio DFT calculations done by Dr. Delgado Gran. The Kohn–Sham spectrum for zigzag and armchair GQDs is shown in Fig. 3.5(f) and (g).

Hence, we see that the nature and character of the energy gap for zigzag and armchair GQDs is different, with two degenerate states for zigzag and three almost degenerate states for armchair top (bottom) of the valence (conduction) band. This

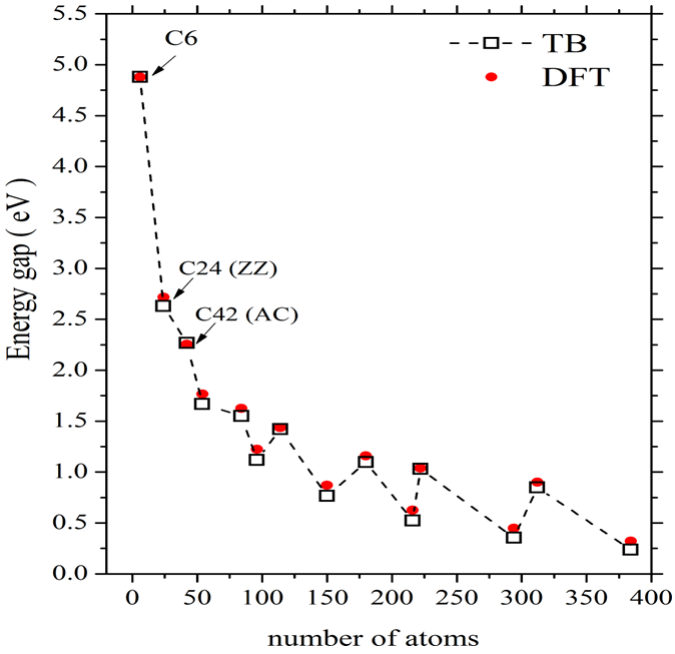

Figure 3.6: Energy gap for zigzag (ZZ) and armchair (AC) GQDs calculated with tight-binding (TB) (black squares) and density functional theory (DFT) (red dots) as a function of the number of Carbon atoms in the dot. DFT results were obtained using GGA-PBE approximation to the exchange-correlation energy. The hopping amplitude $t = -2.439$ eV fits the TB gap of benzene to DFT result. The oscillation starts from smallest ZZ and AC QDs, which are labeled with red boxes.

manifests itself in the oscillation of the energy gap of GQD with an increasing number of atoms, an effect already discussed by Guclu *et al* [114]. Fig. 3.6 shows the energy gap of GQDs with an increasing number of carbon atoms obtained by direct diagonalization of the TB Hamiltonian. An oscillation of the energy gap is visible for all zigzag and armchair structures, starting from the smallest GQDs (C24 and C42). The oscillation of the gap and its dependence $E_g \sim \frac{1}{\sqrt{N_{tot}}}$ for small size GQDs on the total number of atoms N_{tot} can now be understood in terms of the nature of the top of the valence and bottom of the conduction band states discussed above.

3.3 Conclusion

In conclusion, we analyzed the energy spectra of graphene quantum dots in terms of the nearest neighbor tight-binding model and the decomposition of graphene quantum dots into concentric rings. This decomposition allowed us to explain the dependence of the bandgap of zigzag quantum dots in terms of a bandgap of a quasi one-dimensional

outer ring. For the armchair-terminated quantum dots we found the bandgap originating from a six-fold degenerate zero-energy shell of a 1D Lieb lattice. Hence we find the top of the valence band and the bottom of the conduction band doubly degenerate for zigzag-terminated GQDs and three-fold degenerate for the armchair-terminated GQDs. The different origin of the bandgap in the two types of GQDs results in the oscillation of the bandgap with increasing size. The tight-binding results, needed to describe large, million atom graphene quantum dots, are validated by ab initio calculations including excitonic effects in the TD-DFT approach.

Chapter 4

Quantum Simulator of Extended Bipartite Hubbard Model with Broken Sublattice Symmetry: Magnetism, Correlations, and Phase Transitions

We would like to state this chapter is based on Ref. [85] with more derivations and detail shown. I have conducted all calculations in this chapter.

There is currently interest in understanding electronic properties of strongly correlated quantum materials often modelled by an extended Hubbard model [115–117]. It is expected that progress in solutions to this intractable problem may be achieved with quantum simulators.

A quantum simulator is a device that can simulate the behavior of a quantum system using a classical computer or a physical system that behaves according to the laws of quantum mechanics. The simulation of quantum systems is important because quantum mechanics is often too complex to be solved using classical computers, and quantum simulators provide a means of exploring the behavior of quantum systems

and testing quantum algorithms. A quantum simulator should possess certain properties, such as being able to simulate the dynamics of a quantum system accurately and efficiently, and being able to represent a wide range of quantum systems. The simulator should also be able to perform measurements on the simulated system to obtain information about its state [118–120].

Here we describe a proposal of a quantum simulator of the extended bipartite Hubbard model with broken sublattice symmetry inspired by graphene. Much progress in quantum simulators has been achieved with cold atoms and trapped ions [65,121–130]. Progress in solid state and photonic based simulators [66–69,69,70,73–76,82,120,131–136] is enabled by progress in new materials, including quasi-two-dimensional electronic systems (2DES) in semiconductor heterojunctions [9, 137] and graphene.

In this chapter, we develop a quantum simulator and model this quantum simulator of the extended bipartite Hubbard model with broken sublattice symmetry. The simulator consists of a structured lateral gate confining two-dimensional electrons in a quantum well into artificial minima arranged in a hexagonal lattice. The sublattice symmetry breaking is generated by forming an artificial triangular graphene quantum dot (ATGQD) with zigzag edges. The resulting extended Hubbard model gives us the ability to tune the ratio of tunneling strength to electron-electron interactions and control over sublattice symmetry as well as size and shape. The validity of the simulator is confirmed for small systems using mean-field and exact diagonalization many-body approaches which show that the ground state changes from a metallic to an antiferromagnetic (AF) phase by varying the distance between sites or depth of the confining potential. The one-electron spectrum of these triangular dots contains a macroscopically degenerate shell at the Fermi level. The shell persists at the mean-field level for weak interactions (metallic phase) but disappears for strong interactions in the AF phase. We determine the effects of electron-electron interactions on the ground state, the total spin, and the excitation spectrum as a function of filling of the ATGQD. We find that the half-filled charge-neutral shell leads to a partially spin-polarized state in both metallic and AF regimes in accordance with Lieb's theo-

rem [104]. In both regimes a relatively large gap separates the spin-polarized ground state to the first excited many-body state at half filling of the degenerate shell. By adding or removing an electron, this gap drops dramatically, and alternate total spin states emerge with energies nearly degenerate to a spin-polarized ground state.

4.1 Model of triangular artificial graphene quantum dot

We start with electrons confined to a quantum well described by a potential $V(z)$ where z is the growth direction. A metallic gate is deposited on the surface at a distance D from the quantum well. The potential on the gate generates a potential $V(\vec{r}-\vec{R})$ in the plane of a quantum well laterally confining an electron at $\vec{r}$ in the vicinity of position $\vec{R}$. An artificial graphene (AG) structure is defined by structuring the metallic gate, resulting in an array of N confining potentials, artificial atoms, positioned on a hexagonal lattice of potential minima at $\vec{R}_i$ separated by a distance a. We next introduce a back gate from which electrons are drawn into the artificial graphene structure leaving behind a positive, compensating charge described by a gate potential V_g. Hence, the artificial graphene Hamiltonian describing N_e electrons in an array of N potential traps in the quantum well, in the presence of a compensating gate potential and including electron-electron interactions is given by

$$H=\sum_{i=1}^{N_e}\left[-\frac{\hbar^2}{2m^*}\nabla_i^2+\sum_{j=1}^{N}v(\vec{r_i}-\vec{R_j})+v(z_i)+V_g\left(\vec{r_i},z_i\right)\right]+\sum_{i<j}^{N_e}\frac{e^2}{\kappa|\vec{r_i}-\vec{r_j}|}, \quad (4.1)$$

Here, we sum over N_e electrons with effective mass m^* in the field produced by an array of N sites, interacting with a gate, confined to a quantum well by potential $v(z_i)$ and interacting with each other via a Coulomb potential screened by a background dielectric function κ. The potential $v(\vec{r_i}-\vec{R_j})$ is described by a Gaussian potential

$$v(\vec{r_i}-\vec{R_j})=-V_0e^{-\frac{|\vec{r_i}-\vec{R_j}|^2}{d^2}}, \quad (4.2)$$

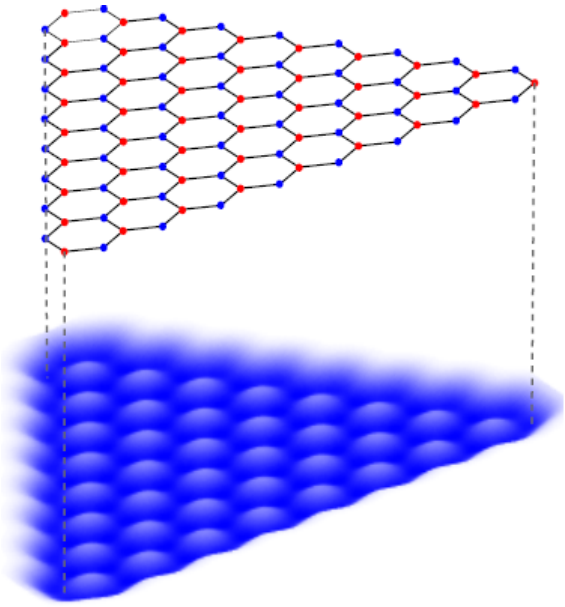

Figure 4.1: Potential profile of ATGQD with zigzag edges, with $N = 97$ sites separated by $a = 15$ nm. There is broken sublattice symmetry in this system in which the number of A sites does not equal the number of B sites.

with depth V_0, confinement length d, localized in the plane of the quantum well at $\vec{R}_j$. The one-electron potential $V(r) = \sum_j v(\vec{r} - \vec{R}_j)$ of the artificial graphene structure studied here is shown in Fig. 4.1. Different structures with different size and shape can be constructed analogously. Here, there are $N = 97$ sites, with each modelled as a Gaussian confining potential, with a depth $V_0 = 300$ meV, confinement length $d = 10$ nm and separation of $a = 15$ nm. We see that the confining potential forms a triangular quantum well, with minima arranged on a hexagonal lattice, with visible benzene like rings and terminated by zigzag edges. Such a structure is an example of a bipartite lattice with broken sublattice symmetry, and as such Lieb's theorem [104] will apply and play a critical role in determining the nature of the ground state.

4.2 One-electron spectrum in the tight-binding model

We now introduce one-electron into the artificial graphene structure shown in Fig. 4.1. Following the model described in Section II, the single-particle Hamiltonian is given by

$$H_0 = -\frac{\hbar^2}{2m^*}\nabla^2 + \sum_j v(\vec{r} - \vec{R}_j) + v(z), \tag{4.3}$$

where the sum over j extends over N sites, and $v(\vec{r}-\vec{R}_j)$ is given in Eq. 4.2. Here $v(z)$ is a potential of an infinite quantum well with width $0.1a$. Throughout this chapter, we assume strong confinement in the z-direction, so that the eigenstates factorize into an in-plane part and a part in the z-direction, which we assume to be the lowest state of an infinite quantum well $\xi(z) = \sqrt{\frac{2}{L}}\sin\frac{\pi z}{L}$. The lateral confining potential is smooth and parabolic at low energies. We note that we can decompose the Gaussian in terms of a parabolic confining potential plus a correction by Taylor expanding about the minimum as

$$\begin{aligned} v(\vec{r}-\vec{R}_j) = -V_0 e^{-\frac{|\vec{r}-\vec{R}_j|^2}{d^2}} &= -V_0 + \frac{|\vec{r}-\vec{R}_j|^2}{d^2} + \delta V_j \\ &= -V_0 + \frac{\overline{\omega}^2}{4}|\vec{r}-\vec{R}_j|^2 + \delta V_j \\ &= v_j^{ho} + \delta V_j, \end{aligned} \tag{4.4}$$

where $\overline{\omega} = \frac{2}{d}\sqrt{V_0}$. The correction term is given as

$$\delta V_j = V_0\left(1 - \frac{|\vec{r}-\vec{R}_j|^2}{d^2}\right) - V_0 e^{-\frac{|\vec{r}-\vec{R}_j|^2}{d^2}}. \tag{4.5}$$

Our Hamiltonian H_0 in Eq.(4.3), ignoring the z-direction, becomes

$$H_0 = -\frac{\partial^2}{\partial x^2} - \frac{\partial^2}{\partial y^2} + \sum_j \left(v_j^{ho} + \delta V_j\right), \tag{4.6}$$

where energies are measured in Rydbergs given by $R_y = \frac{\hbar^2}{2m^* a_B^2}$, and a_B is the Bohr radius. We see that at low energies, the in-plane part of the Hamiltonian mimics that of a 2D harmonic oscillator. Hence we expand the in-plane part of the wavefunction φ for a state ν in terms of two-dimensional harmonic oscillator eigenfunctions α centered on atom j:

$$\varphi^\nu = \sum_{j,\alpha} A_{j\alpha}^\nu \phi_{j\alpha}. \tag{4.7}$$

Our Schrodinger equation is then

$$\left[-\frac{\partial^2}{\partial x^2}-\frac{\partial^2}{\partial y^2}+\sum_j\left(v_j^{ho}+\delta V_j\right)\right]\sum_{l,\alpha}A_{l\alpha}^{\nu}\phi_{l\alpha}=\epsilon^{\nu}\sum_{l,\alpha}A_{l\alpha}^{\nu}\phi_{l\alpha}. \tag{4.8}$$

Projecting a state $m\beta$ on the LHS we get matrix elements of the Hamiltonian given by

$$H_{m\beta,l\alpha}=\epsilon_\beta S_{m\beta,l\alpha}+\langle\phi_{m\beta}|\delta V_m|\phi_{l\alpha}\rangle+\sum_{j\neq m}\langle\phi_{m\beta}|v_j^{ho}+\delta V_j|\phi_{l\alpha}\rangle\,, \tag{4.9}$$

and our Schrodinger equation is

$$\sum_{l,\alpha}H_{m\beta,l\alpha}A_{l\alpha}^{\nu}=\epsilon^{\nu}\sum_{l,\alpha}A_{m\alpha}^{\nu}S_{m\beta,l\alpha}. \tag{4.10}$$

Here $S_{m\beta,l\alpha}=\langle\phi_{m\beta}|\phi_{l\alpha}\rangle$ are overlap matrix elements for orbitals β, α localized on sites m, l. This is a matrix equation which can be written as

$$\mathbf{H}\mathbf{A}^{\nu}=\epsilon^{\nu}\mathbf{S}\mathbf{A}^{\nu}. \tag{4.11}$$

Since the harmonic oscillator states on different sites defined in Eq. 4.7 are not orthogonal, we would like to orthogonalize the basis. We can achieve this by the following:

$$\mathbf{H}\mathbf{A}^{\nu}=\epsilon^{\nu}\mathbf{S}\mathbf{A}^{\nu}=\epsilon^{\nu}\mathbf{S}^{\frac{1}{2}}\mathbf{S}^{\frac{1}{2}}\mathbf{A}^{\nu}, \tag{4.12}$$

inserting the identity $\left(\mathbf{S}^{\frac{1}{2}}\right)^{-1}\mathbf{S}^{\frac{1}{2}}$ we get

$$\mathbf{H}\left(\mathbf{S}^{\frac{1}{2}}\right)^{-1}\mathbf{S}^{\frac{1}{2}}\mathbf{A}^{\nu}=\epsilon^{\nu}\mathbf{S}^{\frac{1}{2}}\mathbf{S}^{\frac{1}{2}}\mathbf{A}^{\nu}. \tag{4.13}$$

This gives our generalized eigenvalue problem

$$\tilde{\mathbf{H}}\mathbf{B}^{\nu}=\epsilon^{\nu}\mathbf{B}^{\nu}, \tag{4.14}$$

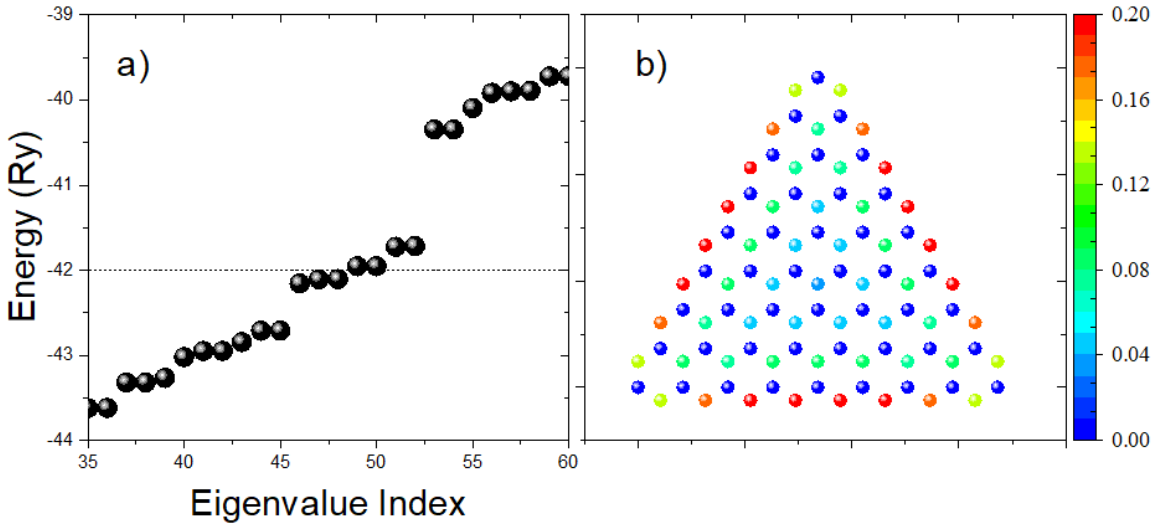

Figure 4.2: a) TB spectrum for AG Triangular quantum dot with zigzag edges near the Fermi level. b) Sum of charge density for the shell containing 7 states near the Fermi level

where $\mathbf{B}^{\nu} = \mathbf{S}^{1/2}\mathbf{A}^{\nu}$ and $\mathbf{S}$ is the overlap matrix. The corresponding renormalized Hamiltonian is

$$\tilde{\mathbf{H}} = \mathbf{S}^{-\frac{1}{2}}\mathbf{H}\mathbf{S}^{-\frac{1}{2}}. \tag{4.15}$$

The wavefunction is now expanded in terms of orthogonal states $\psi_{m\beta}$ localized on different sites

$$\phi^{\nu} = \sum_{m,\beta} B^{\nu}_{m\beta}\psi_{m\beta}. \tag{4.16}$$

The orthogonal orbitals localized on site "m" are given explicitly by

$$\psi_{m\beta} = \sum_{l\alpha}(S^{-\frac{1}{2}})_{l\alpha,m\beta}\phi_{l\beta}. \tag{4.17}$$

Fig. 4.2 shows the energy levels of a single electron obtained by diagonalizing Eq. 4.15 for $N = 97$ sites in the basis of 3 harmonic oscillator shells, S, P, and D per site, with separation of potential minima corresponding to $a = 12.5$ nm, and all other parameters given in section 4.1. We observe a well-defined shell of almost degenerate states at the Fermi level contained in the $1S$-band. We note that the Fermi level corresponds to a half-filled electron system. The nearly degenerate states near the Fermi level localize at the edge of the sample in agreement with that of graphene

[58, 138]. Furthermore, a large gap separates the $1S$ band of levels from the P, and D derived levels and the single-particle spectrum resembles a spectrum obtained by diagonalizing a TB model with nearest neighbour tunneling matrix elements [58]. Thus, we limit ourselves to only S orbitals from here on, in order to simplify many-body calculations. We take the hopping parameter t between nearest-neighbour $1S$ orbitals to be equal to half the bandwidth of the $1S$ band. We find $t = 26.98$ meV for a site separation of $a = 12.5$ nm and $t = 3.18$ meV for a site separation of $a = 15$ nm. In Fig. 4.2 we see a shell of nearly degenerate zero-energy states at the Fermi level split by the introduction of next-nearest-neighbour hopping generated by the itinerant orbitals. Note that in artificial graphene, it is possible to have a single electron moving in the system of potential minima, and optical experiments, for example, could probe the existence of this zero-energy shell.

4.3 Many-body Hamiltonian

With the orthogonalized orbitals $\psi_{m\beta}$ limited to the $1S$ band, we can write the many-body Hamiltonian, Eq. 4.1, in the second quantized form as

$$H = \sum_{i,\sigma} \epsilon_{i\sigma} c^\dagger_{i\sigma} c_{i\sigma} + \sum_{i,j,\sigma} t_{ij} c^\dagger_{i\sigma} c_{j\sigma} + \frac{1}{2} \sum_{i,j,k,l,\sigma,\sigma'} \langle ij|V|kl\rangle \, c^\dagger_{i\sigma} c^\dagger_{j\sigma'} c_{k\sigma'} c_{l\sigma} + \sum_{i,\sigma} v^g_{ii} c^\dagger_{i\sigma} c_{i\sigma}, \tag{4.18}$$

where $\epsilon_{i\sigma}$ are the onsite energies and $t_{ij\sigma}$ are the hopping matrix elements computed above. v^g_{ii} corresponds to the back gate and $\langle ij|V|kl\rangle$ are Coulomb matrix elements given by

$$\begin{aligned} \langle ij|V|kl\rangle = R_y \int dz_1 dz_2 \int d\vec{r}_1 d\vec{r}_2 \psi^*_i(\vec{r}_1) \xi^*_i(z_1) \psi^*_j(\vec{r}_2) \xi^*_j(z_2) \\ \times \frac{2}{|\vec{r}_1 - \vec{r}_2 + (z_1 - z_2)\hat{z}|} \psi_k(\vec{r}_2) \xi_k(z_2) \psi_l(\vec{r}_1) \xi_l(z_1), \end{aligned} \tag{4.19}$$

where the functions ψ_i are the $1S$ localized and orthogonal orbitals which are defined in Eq. 4.17. The functions $\xi = \sqrt{\frac{2}{L}} \sin(\frac{\pi z}{L})$ describe the lowest-energy sub-band of an infinite quantum well confining the electrons in the z-direction, while Hubbard U is

Matrix Element	Value (R_y)
$\langle 11\|V\|11\rangle$	6.596
$\langle 12\|V\|21\rangle$	2.166
$\langle 13\|V\|31\rangle$	1.177
$\langle 11\|V\|12\rangle$	0.509
$\langle 12\|V\|31\rangle$	0.231
$\langle 12\|V\|12\rangle$	0.091
$\langle 11\|V\|22\rangle$	0.091
$\langle 22\|V\|13\rangle$	0.0095
$\langle 12\|V\|23\rangle$	0.037
$\langle 11\|V\|13\rangle$	0.0093

Matrix Element	Value (R_y)
$\langle 11\|V\|11\rangle$	6.636
$\langle 12\|V\|21\rangle$	1.455
$\langle 13\|V\|31\rangle$	0.809
$\langle 11\|V\|12\rangle$	0.065
$\langle 12\|V\|31\rangle$	0.015
$\langle 12\|V\|12\rangle$	0.033
$\langle 11\|V\|22\rangle$	0.033
$\langle 22\|V\|13\rangle$	0.003
$\langle 12\|V\|23\rangle$	0.0035
$\langle 11\|V\|13\rangle$	0.0012

Table 4.1: Coulomb matrix elements for artificial graphene using $1S$ harmonic oscillator orbitals. In the left table it is computed for a separation $a = 10$ nm and in the right it is computed for $a = 15$ nm

defined as $U = \langle ii|V|ii\rangle$. We use the VEGAS algorithim to compute Coulomb matrix elements for different seperation between dots a. Table. 4.1 shows the Coulomb matrix elements computed for artificial graphene for two different separation between sites, $a = 10$ nm and $a = 15$nm. It is interesting to note that for $a = 15$ nm the sites are well separated and on average the Coulomb matrix elements appear smaller with the exception of the onsite term. One would think this corresponds to the more weakly interacting regime, but in fact it does not. This is because the hopping parameter t which is characteristic of the single-particle properties of the system drops much more dramatically and the ratio between the Coulomb matrix elements and the hopping paramter grows much more dramatically.

The back gate term is given by

$$v_{ii}^{g} = \sum_{j} \frac{-\frac{2N_p}{N}}{\sqrt{(x_i - x_j)^2 + (y_i - y_j)^2 + d_{gate}^2}}, \tag{4.20}$$

where N_p is the number of positive charges on the gate. The model assumes that N_p is equal to the number of electron charges in the system N in order to enforce charge neutrality, and is uniformly smeared on the gate.

Since the Hamiltonian in Eq. 4.18 cannot be solved exactly, we start by solving the mean-field HF problem first.

4.4 Mean-field Hartree-Fock calculation

The magnetic properties of artificial graphene, and the nature of the ground state for different electron numbers, can be determined by solving the mean-field HF Hamiltonian derived in 2.3.1 and given by:

$$H_{MF}^{ATGQD} = -\sum_{i,l,\sigma} t_{il\sigma} c_{i\sigma}^{\dagger} c_{l\sigma} + \sum_{i,j,k,l,\sigma,\sigma'} \left[\langle ij|V|kl\rangle - \langle ij|V|lk\rangle\, \delta_{\sigma\sigma'}\right] \rho_{jk\sigma'} c_{i\sigma}^{\dagger} c_{l\sigma}, \quad (4.21)$$

where we are ignoring the positive background for the time being, it will be included later. To help with convergence of the HF procedure, we can exploit the solution of bulk AG, then measure our density matrix elements with respect to deviations from the bulk solution. This is done in the following way:

$$\begin{aligned}
H_{MF}^{ATGQD} =& H_{MF}^{ATGQD} - H_{MF}^{0} + H_{MF}^{0} \\
=& \left[-\sum_{i,l,\sigma}^{N} t_{il\sigma} c_{i\sigma}^{\dagger} c_{l\sigma} + \sum_{i,j,k,l,\sigma,\sigma'}^{N} \left[\langle ij|V|kl\rangle - \langle ij|V|lk\rangle\, \delta_{\sigma\sigma'}\right] \rho_{jk\sigma'} c_{i\sigma}^{\dagger} c_{l\sigma}\right] \\
& - \left[-\sum_{i,l,\sigma}^{\infty} t_{il\sigma} c_{i\sigma}^{\dagger} c_{l\sigma} + \sum_{i,j,k,l,\sigma,\sigma'}^{\infty} \left[\langle ij|V|kl\rangle - \langle ij|V|lk\rangle\, \delta_{\sigma\sigma'}\right] \rho_{jk\sigma'}^{0} c_{i\sigma}^{\dagger} c_{l\sigma}\right] \\
& + \left[-\sum_{i,l,\sigma}^{\infty} t_{il\sigma} c_{i\sigma}^{\dagger} c_{l\sigma} + \sum_{i,j,k,l,\sigma,\sigma'}^{\infty} \left[\langle ij|V|kl\rangle - \langle ij|V|lk\rangle\, \delta_{\sigma\sigma'}\right] \rho_{jk\sigma'}^{0} c_{i\sigma}^{\dagger} c_{l\sigma}\right] \\
=& \left[-\sum_{i,l,\sigma}^{N} t_{il\sigma} c_{i\sigma}^{\dagger} c_{l\sigma} + \sum_{i,j,k,l,\sigma,\sigma'}^{N} \left[\langle ij|V|kl\rangle - \langle ij|V|lk\rangle\, \delta_{\sigma\sigma'}\right] \rho_{jk\sigma'} c_{i\sigma}^{\dagger} c_{l\sigma}\right] \\
& - \sum_{i,l,\sigma}^{\infty} \left[-t_{il\sigma} c_{i\sigma}^{\dagger} c_{l\sigma} + \sum_{j,k,\sigma'}^{\infty} \left[\langle ij|V|kl\rangle - \langle ij|V|lk\rangle\, \delta_{\sigma\sigma'}\right] \rho_{jk\sigma'}^{0} c_{i\sigma}^{\dagger} c_{l\sigma}\right] \\
& + \sum_{i,l,\sigma}^{\infty} \left[-t_{il\sigma} c_{i\sigma}^{\dagger} c_{l\sigma} + \sum_{j,k,\sigma'}^{\infty} \left[\langle ij|V|kl\rangle - \langle ij|V|lk\rangle\, \delta_{\sigma\sigma'}\right] \rho_{jk\sigma'}^{0} c_{i\sigma}^{\dagger} c_{l\sigma}\right].
\end{aligned} \quad (4.22)$$

We can split the summation up in the middle term (the sum that runs over i, and l) from $1...N$ and then from $N+1...\infty$ and the outcome after some algebra is

$$\begin{aligned} H_{MF}^{ATGQD} = & \left[\sum_{i,j,k,l,\sigma,\sigma'}^{N} \left[\langle ij|V|kl\rangle - \langle ij|V|lk\rangle \, \delta_{\sigma\sigma'} \right] \rho_{jk\sigma'} c_{i\sigma}^{\dagger} c_{l\sigma} \right] \\ & - \sum_{i,l,\sigma}^{N} \left[\sum_{j,k,\sigma'}^{\infty} \left[\langle ij|V|kl\rangle - \langle ij|V|lk\rangle \, \delta_{\sigma\sigma'} \right] \rho_{jk\sigma'}^{0} c_{i\sigma}^{\dagger} c_{l\sigma} \right] \\ & + \sum_{i,l,\sigma}^{N} \left[-t_{il\sigma} c_{i\sigma}^{\dagger} c_{l\sigma} + \sum_{j,k,\sigma'}^{\infty} \left[\langle ij|V|kl\rangle - \langle ij|V|lk\rangle \, \delta_{\sigma\sigma'} \right] \rho_{jk\sigma'}^{0} c_{i\sigma}^{\dagger} c_{l\sigma} \right]. \end{aligned} \tag{4.23}$$

If we ignore three and four-center scattering Coulomb matrix elements near the edge of the triangular graphene quantum dot we get our HF Hamiltonian:

$$\begin{aligned} H_{MF}^{ATGQD} = & \sum_{i,l,\sigma}^{N} \tau_{il\sigma}^{0} c_{i\sigma}^{\dagger} c_{l\sigma} + \sum_{i,j,k,l,\sigma,\sigma'}^{N} \left[\langle ij|V|kl\rangle - \langle ij|V|lk\rangle \, \delta_{\sigma\sigma'} \right] \times \left(\rho_{jk\sigma'} - \rho_{jk\sigma'}^{0} \right) c_{i\sigma}^{\dagger} c_{l\sigma} \\ & + \sum_{i,\sigma}^{N} v_{ii}^{g} c_{i\sigma}^{\dagger} c_{i\sigma}, \end{aligned} \tag{4.24}$$

where $\rho_{jk\sigma'}$ is are density matrix elements for the ATGQD, and $\rho_{jk\sigma'}^{0}$ is the density matrix for the bulk system. $\tau_{il\sigma}^{0}$ is defined in Eq. 2.108 but for the bulk system. We have included the positive background back in the expression. The density matrix elements for bulk graphene are derived in Ref. 1. In the metallic phase we have $\rho_{jk\sigma'}^{0} = \frac{1}{2}$ when $j = k$ and $\rho_{jk\sigma'}^{0} = 0.262$ when j, k are NNs. Graphene is a semi-metal and as such, we expect that AG in the metallic phase will behave like graphene. But Ref. 81 predicted that for smaller values of the ratio between Hubbard U and the NN tunnelling matrix element t, a 2D honeycomb lattice system is in a metallic phase, while when the ratio is large the system is in the AF phase. In other words, a phase transition occurs as a function of the ratio $\frac{U}{t}$. We control this ratio by tuning the separation between sites. As such we will proceed to derive the NN density matrix elements assuming that we are in the AF phase. We start with the mean field

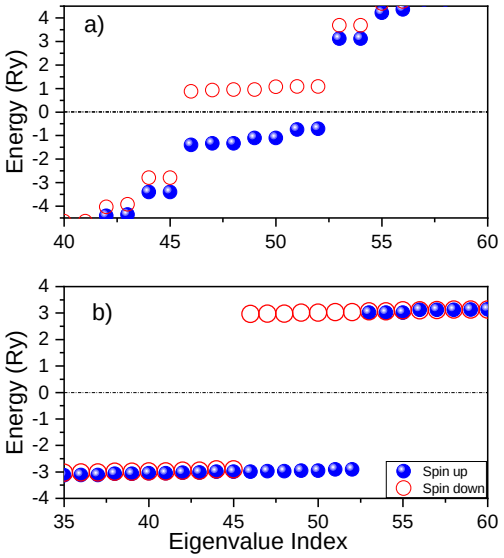

Figure 4.3: a) HF Spectrum for ground state of N=97 sites at half-filling with lattice constant $a = 12.5$ nm. We observe a shell of distinct degenerate states near the Fermi level, with spin up and down electrons, and a splitting of spin degeneracy of all levels due to an imbalance of up and down spins found in the HF solution. All states below the Fermi level $E_F = 0$ (middle line) are occupied, all states above are unoccupied. b) HF spectrum for lattice separation $a = 15$ nm. Note the disappearance of a degenerate shell at the Fermi level and emergence of a large gap proportional to Hubbard U separating the valence and conduction band states, AF spin ordering and a partially spin-polarized ground state.

Hamiltonian for bulk graphene (or artificial graphene) given by

$$H^0_{MF} = \sum_{i,l,\sigma} t_{il\sigma} c^\dagger_{i\sigma} c_{l\sigma} + \sum_{i,j,k,l,\sigma,\sigma'} \left[\langle ij|V|kl\rangle - \langle ij|V|lk\rangle\, \delta_{\sigma\sigma'}\right] \rho^0_{jk\sigma'} c^\dagger_{i\sigma} c_{l\sigma}. \tag{4.25}$$

Now, if we take only onsite density matrix elements, and we keep only terms where $i = l$ (i.e. ignore small scattering elements), we can write the Hamiltonian as

$$H^0_{MF} = \sum_{i,l,\sigma} t_{il} c^\dagger_{i\sigma} c_{l\sigma} + \sum_{i,\sigma} \Delta_{i\sigma} c^\dagger_{i\sigma} c_{i\sigma}, \tag{4.26}$$

where

$$\Delta_{i\sigma} = \sum_{j\sigma'} \left[\langle ij|V|ji\rangle - \langle ij|V|ij\rangle\, \delta_{\sigma\sigma'}\right] \rho^0_{jj\sigma'}. \tag{4.27}$$

Postulating that we are in the AF regime, so that

$$\rho^0_{jj\uparrow} = \begin{cases} 1 & j \in \text{Sublattice A} \\ 0 & j \in \text{Sublattice B} \end{cases}, \tag{4.28a}$$

$$\rho^0_{jj\downarrow} = \begin{cases} 0 & j \in \text{Sublattice A} \\ 1 & j \in \text{Sublattice B}, \end{cases} \tag{4.28b}$$

we arrive at the expressions

$$\Delta_{A\uparrow} = \sum_{j>1} \langle 1j|V|j1\rangle\,, \tag{4.29a}$$

$$\Delta_{A\downarrow} = U + \sum_{j>1} \langle 1j|V|j1\rangle\,, \tag{4.29b}$$

$$\Delta_{B\uparrow} = U + \sum_{j>1} \langle 1j|V|j1\rangle\,, \tag{4.29c}$$

$$\Delta_{B\downarrow} = \sum_{j>1} \langle 1j|V|j1\rangle\,, \tag{4.29d}$$

where $\langle 1j|V|j1\rangle$ corresponds to a direct interaction with a fixed site we call $i = 1$, and another site j which is independent of which sublattice we fix our state $i = 1$ to since all sites are identical. Now we can subtract the constant $\frac{U}{2} + \sum_{i>1} \langle 1i|V|i1\rangle$ from all terms since this leads to only a shift in energies. We get

$$\Delta_{A\uparrow} = -\frac{U}{2}, \tag{4.30a}$$

$$\Delta_{A\downarrow} = \frac{U}{2}, \tag{4.30b}$$

$$\Delta_{B\uparrow} = \frac{U}{2}, \tag{4.30c}$$

$$\Delta_{B\downarrow} = -\frac{U}{2}. \tag{4.30d}$$

Taking nearest-neighbours hopping only, the Hamiltonian in the basis of sublattices $A\uparrow$, $B\uparrow$, $A\downarrow$, $B\downarrow$ is given by

$$H\left(\vec{k}\right) = \begin{bmatrix} -\frac{U}{2} & -tf(\vec{k}) & 0 & 0 \\ -tf^*(\vec{k}) & \frac{U}{2} & 0 & 0 \\ 0 & 0 & \frac{U}{2} & -tf(\vec{k}) \\ 0 & 0 & -tf^*(\vec{k}) & -\frac{U}{2} \end{bmatrix}. \tag{4.31}$$

This Hamiltonian is block diagonal, with each block mimicking gapped graphene. The Bloch functions are given as

$$\phi_k^A(\vec{r}) = \frac{1}{\sqrt{N_U}} \sum_{\vec{R}_A} e^{i\vec{k}\cdot\vec{R}_A} \phi_z\left(\vec{r} - \vec{R}_A\right), \tag{4.32a}$$

$$\phi_k^B(\vec{r}) = \frac{1}{\sqrt{N_U}} \sum_{\vec{R}_B} e^{i\vec{k}\cdot\vec{R}_B} \phi_z\left(\vec{r} - \vec{R}_B\right), \tag{4.32b}$$

The valence band solution is given by

$$E_k^- = -\sqrt{\left(\frac{U}{2}\right)^2 + t^2|f(\vec{k})|^2}, \tag{4.33}$$

$$\psi_{k-}{}^{(\downarrow)} = -\sin\frac{\varphi_k}{2} e^{i\theta_k} \phi_k^A(\vec{r}) + \cos\frac{\varphi_k}{2} \phi_k^B(\vec{r}), \tag{4.34a}$$

$$\psi_{k-}^{(\uparrow)}(\vec{r}) = \cos\frac{\varphi_k}{2} \phi_k^A(\vec{r}) - \sin\frac{\varphi_k}{2} \phi_k^B(\vec{r}), \tag{4.34b}$$

where $\frac{U}{2} = |E_k^-|\cos\varphi_k$ defines φ_k, and $f(\vec{k})$ is the usual form factor of graphene. The density matrix elements are defined as

$$\rho_{ij\sigma}^0 = \sum_{\vec{k}} b^*_{\vec{R}_i,\vec{k},\sigma} b_{\vec{R}_j,\vec{k},\sigma}, \tag{4.35}$$

where $b_{\vec{R}_j,\vec{k},\sigma}$ are the coefficients of the wavefunction defined in Eq. 4.34. Computing the density matrix we have

$$\rho^0_{BB\downarrow} = \rho^0_{AA\uparrow} = \sum_{\vec{k}} \cos^2 \frac{\varphi_k}{2} \approx 1, \tag{4.36a}$$

$$\rho^0_{BB\uparrow} = \rho^0_{AA\downarrow} = \sum_{\vec{k}} \left(1 - \cos^2 \frac{\varphi_k}{2}\right) \approx \frac{t}{U}, \tag{4.36b}$$

$$\rho^0_{BB\uparrow} = \rho^0_{AA\downarrow} = \sum_{\vec{k}} \sin \frac{\varphi_k}{2} \cos \frac{\varphi_k}{2} e^{-i\theta_k} e^{i\vec{k}\cdot b} \approx 0, \tag{4.36c}$$

where the approximate solution exploits the fact that we are in the AF phase and so $\frac{t}{U} << 1$. This is in agreement with the numerical calculation of the density matrix elements in a finite flake in the center of the structure where the atoms environment is like bulk.

Now recalling Eq. 4.25, $\tau^0_{il\sigma}$ is a tunneling matrix element which describes the properties of bulk artificial graphene in terms of the tunneling matrix element t_{il} and bulk density matrix $\rho^0_{jk\sigma}$. It is given by

$$\tau^0_{il\sigma} = -t_{il\sigma} + \sum_{jk\sigma'} \left[\langle ij|V|kl\rangle - \langle ij|V|lk\rangle \, \delta_{\sigma\sigma'}\right] \rho^0_{jk\sigma'}. \tag{4.37}$$

Here the superscript 0 on $\tau^0_{il\sigma}$ is to denote that it is computed with the bulk density matrix elements. In addition to the onsite interaction terms, all direct terms are taken into account, as well as all exchange terms up to NNNs. The bulk density matrix elements are given in Eq. 4.36. They have been obtained by Potasz et al. [106] for the metallic regime. We use the solution of the TB model as an input of our initial state to the HF equation. We note the Hamiltonian in Eq. 4.24 is symmetric with respect to spin, and thus can be diagonalized in separate subspaces for spin up and spin down, but with the spin up Hamiltonian having a dependence on the density of spin down electrons and vice versa. We focus on $S_z \geq 0$ and proceed to diagonalize Eq.(4.24), with results shown in Fig. 4.3 and Fig. 4.4.

Fig. 4.3(a) shows the energy spectrum for spin up and down electrons in the

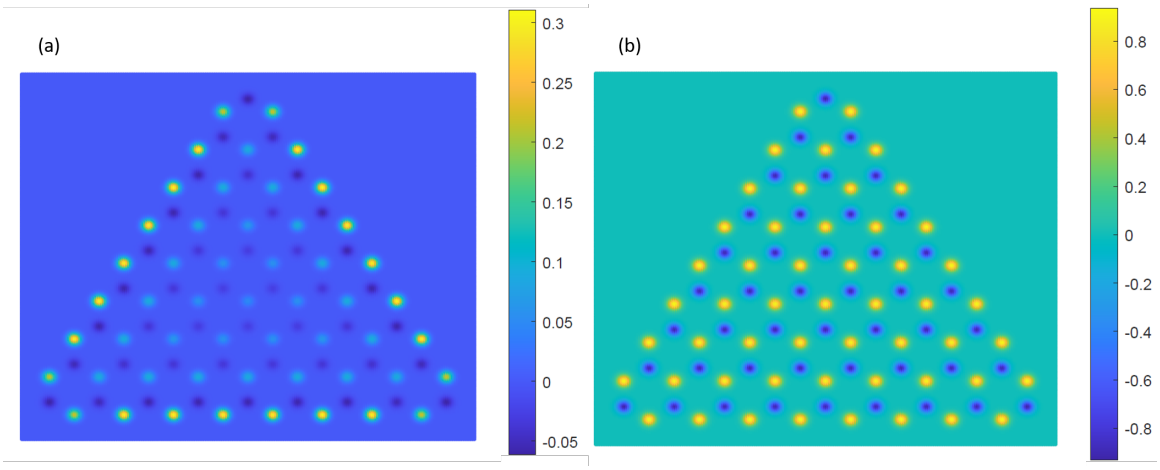

Figure 4.4: a) Spin density obtained for the spin-polarized HF ground state for $a = 12.5$ nm. We observe the simulator to be in the metallic phase, with the extra spins occupying the edge. b) Spin density for the spin-polarized ground state for $a = 15$ nm . We notice one spin is localized on one sublattice, while the other, is localized on the other sublattice. Due to a sublattice imbalance this as well leads to spin-polarized electrons localized on the edge.

metallic regime, $a = 12.5$ nm. We see a spin splitting of levels due to a spin imbalance obtained in HF and consistent with Lieb's theorem. We observe a nearly degenerate shell at the Fermi level, with the blue spin up electrons fully occupying a degenerate shell, leaving the red spin down levels completely empty above the Fermi level. These extra spins are found to align on the edge of the triangle as seen in Fig. 4.4(a), with a uniform zero spin density away from the edges indicating a semi-metallic regime.

We now proceed to the strongly interacting regime by increasing the distance between lattice sites to $a = 15$ nm. We find the ground state to be again partially spin-polarized due to broken sublattice symmetry in agreement with Lieb's theorem [104]. We however lose the distinct degenerate shell at the Fermi level. Instead we find a large gap, proportional to Hubbard U, separating the valence and conduction band, suggesting an insulating phase (Fig. 4.3(b)). We observe an antiferromagnetic spin ordering in the bulk as shown in Fig. 4.4(b) as expected in the large U/t regime [81] and ferromagnetic ordering at the edges of the ATGQD.

4.5 Electronic correlations via configuration interaction

In this section we include the effects of correlations via the configuration interaction method. It is separated into two subsections, one for the metallic phase, and one for the AF phase.

4.5.1 Electronic correlations in the metallic phase

We now turn to including electronic correlations. Let us begin with the semi-metallic phase. In the example of ATGQD with $N = 97$ sites, the breaking of sublattice symmetry results in $N_d = 7$ fold degenerate shell as shown in Figure 4.3. The electronic correlations are most important for electrons occupying the degenerate shell and we will treat them using the configuration-interaction (CI) method. The remaining background electrons are treated in HF. Hence we proceed to solve the HF problem for $97 - 7 = 90$ electrons on 97 sites with $N_\uparrow = N_\downarrow = 45$. This leaves the degenerate shell at the Fermi level empty. We then rotate the many-body Hamiltonian, Eq. 4.18, to the HF basis [106, 139] for $N = 90$ with the final result given by

$$H = \sum_{p,\sigma} \epsilon^{HF}_{p\sigma} b^\dagger_{p\sigma} b_{p\sigma} - \sum_{p,q,\sigma} t_{pq\sigma} b^\dagger_{p\sigma} b_{q\sigma} + \frac{1}{2} \sum_{p,q,r,s,\sigma,\sigma'} \langle pq|V|rs\rangle \, b^\dagger_{p\sigma} b^\dagger_{q\sigma'} b_{r\sigma'} b_{s\sigma} + \sum_{p,q,\sigma} v^{add}_{pq} b^\dagger_{p\sigma} b_{q\sigma}, \tag{4.38}$$

where

$$v^{add}_{pq} = \sum_{i,j} a^*_{ip\sigma} a_{iq\sigma} \frac{-\frac{2N_{add}}{N}}{\sqrt{(x_i - x_j)^2 + (y_i - y_j)^2 + d^2_{gate}}}, \tag{4.39}$$

$$t_{pq\sigma} = \sum_{i,l} \tau_{il\sigma} a^*_{il\sigma} a_{lq\sigma}, \tag{4.40}$$

and

$$b_{q\sigma} = \sum_{l} a_{lq\sigma} c_{l\sigma}, \tag{4.41}$$

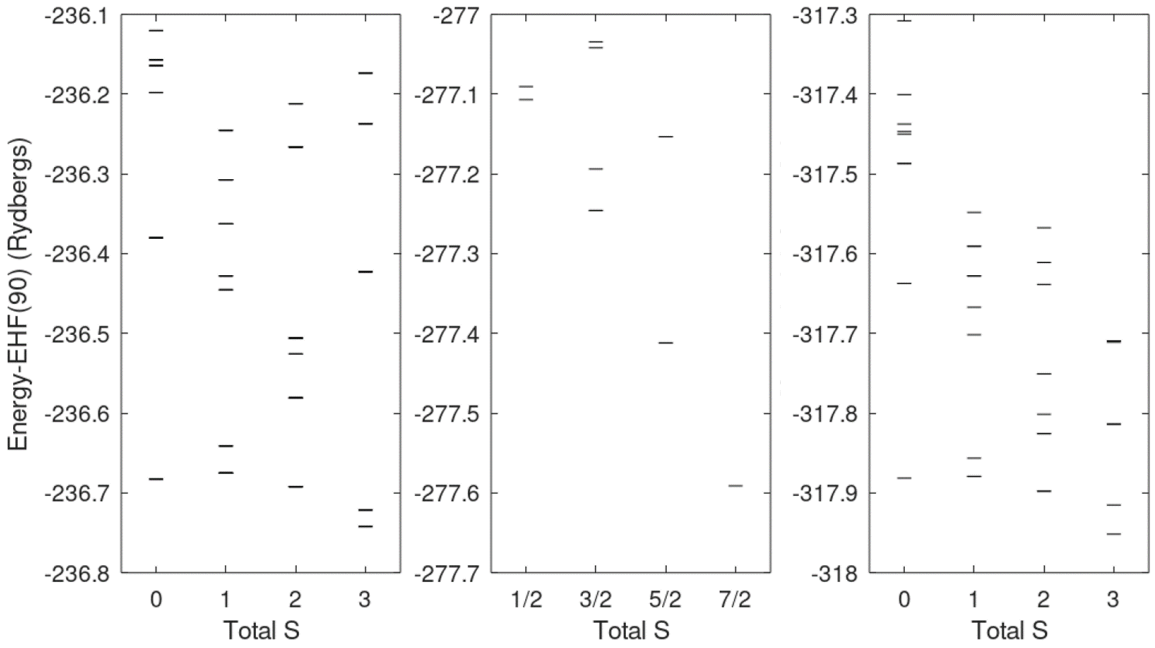

Figure 4.5: The low-energy spectra in the metallic phase for a) 97-1 electrons b) 97 electrons c) 97+1 electrons. For 97 electrons the ground state is partially spin-polarized, and we see a large gap that separates this state from other spin states, but the introduction or removal of an electron collapses this gap and many spins states exist at very close energies to the spin-polarized ground state for the $N = 97 - 1$ and $N = 97 + 1$ electron cases.

with $\tau_{il\sigma}$ defined in Eq. 4.37 but computed with respect to ATGQD density matrix elements. $a_{lq\sigma}$ are the eigenvectors obtained by diagonalizing Eq. 4.24. We note that a term $t_{pq\sigma}$ appears. It lowers the contribution of the quasiparticle-quasiparticle interaction term $\langle pq|V|rs\rangle$. $\langle pq|V|rs\rangle$ are Coulomb matrix elements in the basis of HF states, and are computed by rotating the real-space matrix elements in Eq. 4.19, to the basis of HF states. They describe the remaining interaction of HF quasiparticles beyond the mean-field. The last term in Eq. 4.38 involving v_{pq}^{add} describes additional HF quasiparticles added to the degenerate shell. Since we solve the HF problem for $N_e = 90$ electrons, when adding HF quasiparticles at the CI level, we must compensate this charge with additional positive charges on the gate to maintain charge neutrality. Since a large gap separates the nearly degenerate shell from other states, it suffices to take only the shell near the Fermi level for CI calculations and neglect scattering from the valence band to the shell or from the shell to the conduction band. Fig. 4.5 shows the low-energy spectra obtained by diagonalizing Eq. 4.38 for half-filled system

with $N = 97$, with extra electron ($N = 98$) and with extra hole ($N = 96$). Focusing on the half-filled (N=97 electrons) case in Fig. 4.5(b), we see the ground state of the half-filled shell to be maximally spin-polarized, in agreement with Lieb's theorem. The energy of this configuration is well separated from other states with lower total spin S, in other words the energy gap between our ground state, and first excited state with a different total spin S is large. This implies that the energy cost to flip a spin is large. The removal or addition of a single electron, Fig. 4.5(a) and Fig. 4.5(c), results in a ground state which is still maximally spin-polarized, but other low spin states lower their energy due to correlations, with many total S states emerging very close in energy. It costs practically zero energy to flip a spin in this case. In contrast to regular graphene [106] where the ground state corresponded to $S = 0$, the ground state here has $S = 3$, but we observe a dramatic drop of the energy gap between different total S states, a phenomenon seen in graphene as well [58, 106, 138]. Correlations in the lower spin states cause a decrease of the energies, they become almost degenerate in energy with the maximum spin state. It is worth noting that the spin of the ground state for $N = 96$ electrons is in agreement with Ref. [106], and the shrinking of the gap between different total spins states is consistent as well.

4.5.2 Electronic correlations in the antiferromagnetic phase

Due to the very different quasiparticle spectra for the AF phase and the semi-metallic phase as seen in Fig. 4.3, we require two different approaches to the many-body problem. Here we solve the many-body problem in the AF phase in real space by improving on the HF ground state in real space. In the AF phase there is no degenerate shell at the Fermi level. Hence, we begin with the HF solution in the AF phase. We obtain the HF solution for a fixed number of spin up and spin down electrons by diagonalizing Eq. 4.24, yielding a single Slater determinant

$$|HFGS\rangle = \prod_{q=1}^{\lambda_F^{\uparrow}} b_{q\uparrow}^{\dagger} \prod_{q=1}^{\lambda_F^{\downarrow}} b_{q\downarrow}^{\dagger} |0\rangle \,, \tag{4.42}$$

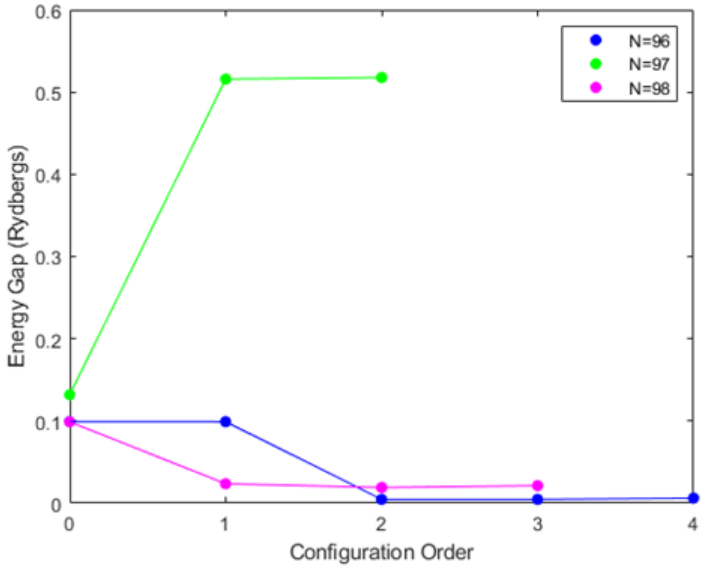

Figure 4.6: Energy Gap for different number of electrons as a function of increasing Hilbert space size. In green, we are at half-filling, and the gap between the ground state and the next spin state is very large, while for the case where we have added or removed an electron from the system, the energy gap collapses to almost zero.

is defined by filling up HF quasi particle levels up to the Fermi level for each spin. We then rotate this HF state to the site basis. In the site representation, we have a linear combination of Slater determinants, and we select the largest contributing state. For example, at half-filling for $S_z = \frac{7}{2}$, the ground state is given by

$$|GS\rangle = \prod_{i\in A} c^\dagger_{i\uparrow} \prod_{i\in B} c^\dagger_{i\downarrow} |0\rangle \,, \tag{4.43}$$

where we place spin up electrons on the A sublattice, and spin down electrons on the B sublattice, representing a perfect antiferromagnetic phase. This is the largest dominant real space configuration composing that HF ground state seen in Fig. 4.4(b). We then divide the Hilbert space into segments for different S_z subspaces. This is done by starting with the ground state for different S_z, as shown above and constructing configurations with the same total S_z. The Hilbert space is divided into 5 sets of configurations defined by

$$|O_{1,0}\rangle = \sum_{\substack{i,j,\sigma \\ <0DO>}} c^\dagger_{j\sigma} c_{i\sigma} |GS\rangle \tag{4.44a}$$

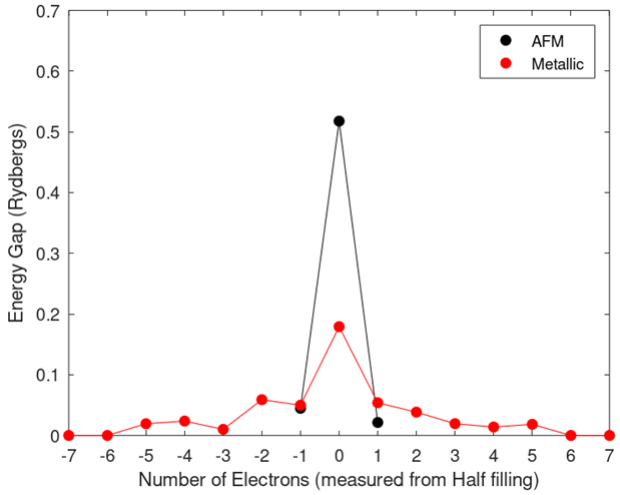

Figure 4.7: Energy gap vs filling factor, for AF (black) and metallic regime (red). In both cases a similar behaviour is observed in which at half-filling the gap is large, and collapses away from half-filling.

$$|O_{1,1}\rangle = \sum_{\substack{i,j,\sigma \\ <1DO>}} c^\dagger_{j\sigma} c_{i\sigma} \, |GS\rangle \tag{4.44b}$$

$$|O_{2,0}\rangle = \sum_{\substack{i,j,k,l,\sigma,\sigma' \\ <0DO>}} c^\dagger_{l\sigma} c^\dagger_{k\sigma'} c_{j\sigma'} c_{i\sigma} \, |GS\rangle \tag{4.44c}$$

$$|O_{2,1}\rangle = \sum_{\substack{i,j,k,l,\sigma,\sigma' \\ <1DO>}} c^\dagger_{l\sigma} c^\dagger_{k\sigma'} c_{j\sigma'} c_{i\sigma} \, |GS\rangle \tag{4.44d}$$

$$|O_{2,2}\rangle = \sum_{\substack{i,j,k,l,\sigma,\sigma', \\ <2DO>}} c^\dagger_{l\sigma} c^\dagger_{k\sigma'} c_{j\sigma'} c_{i\sigma} \, |GS\rangle \, , \tag{4.44e}$$

where the brackets under the sum denote a restriction of the configurations in which we include either 0, 1 or 2 double occupancies (DO) measured from the number of DO of the ground state. The subscripts of $|O_{\mu,\nu}\rangle$ are defined with the first number denoting the number of electrons moved, and the second number being the number of extra double occupancies. We also restrict configurations by allowing only nearest-neighbour scatterings describing correlations. We then proceed to diagonalize the Hamiltonian in Eq. 4.18, as it is written in the site basis, and not in the HF basis. We take the same Coulomb matrix elements as described at the HF stage. After diagonalization, we observe a maximally spin-polarized ground state in the case of $N = 96$, 97 and 98 electrons. In the case of adding or removing an electron, the

energies are very close to each other. In Fig. 4.6 we observe that in the half-filled case we have a large gap separating this state from any other spin state. Meanwhile, when we add or remove an electron the energy gap between the spin-polarized ground state, and the spin state closest in energy collapses to nearly zero. We now compare the metallic phase and AF phases. We first note that in the metallic phase, we see an emergence of a shell at zero energy of states which are practically degenerate. Here we are guided by the intuition that exchange interaction will lower the energy of a spin-polarized half-filled system thus expecting Lieb's theorem to be valid. In the AF regime, without the presence of a degenerate shell, we still see a spin-polarized ground state. We then explore the regimes where we move away from half-filling, where Lieb's theorem doesn't need to hold. In both regimes, we see a collapse of the energy gap. This is consistent with previous work [58, 106]. Fig. 4.7 shows schematically the collapse of the energy gap away from half-filling. The gap peaks at half-filling and collapses when we add/remove an electron. We note that in the metallic regime, we study this as a function of filling factor, and see that the gap is maximum at half filling, where the spin-polarized ground state is most stable.

Chapter 5

Edge States in HgTe Quantum Dots

We would like to state that this chapter is based on Ref. [86] and only minor changes were made to fix any typos or rewrite a few things more clearly. I have conducted all calculations in this chapter except for the calculations involving strain.

There is currently significant interest in both topological insulators (TIs) [140–151] and in semiconductor quantum dots [1,40–46,152–154]. A TI is a semiconductor with an insulated bulk and an energy gap in which the gapless helical states, localized at the edge of the material, were predicted to exist [140–142, 144–147]. The interest in TIs was stimulated further by the experimental demonstration of edge states and the spin quantum Hall effect in HgTe/CdTe quantum wells with an inverted band structure [142] and in many other materials [144–151].

Simultaneously, the interest in semiconductor quantum dots is driven by potential applications in lasers, transistors, and single and entangled photon sources as building blocks in quantum technologies [40–46]. Moreover, interest in HgTe-based nanocrystals and nanoplatelets [155, 156] is motivated by their potential application as far-infrared (FIR) detectors [157, 158]. In normal semiconductors, edge states, being detrimental to the performance of the devices, are commonly passivated. This improves the performance of the device. By contrast, edge states in topologically

nontrivial insulators are robust and give rise to novel physics. For example, one can envisage edge states as realizations of one-dimensional (1D) strongly interacting systems and, as will be discussed in this chapter, sites in one-dimensional Hubbard models [99, 100, 159]. Edge states also arise naturally in the study of quantum dots in two-dimensional (2D) materials such as graphene [1].

The theory of interface between topological and normal HgTe insulators was developed by, e.g., Volkov and Pankratov [140], Zhang et al. [141], and Fu and Kane [160]. Zhang et al. [141] used $\vec{k} \cdot \vec{p}$ theory to derive the four-band effective 2D Bernevig-Hughes-Zhang (BHZ) Hamiltonian. The BHZ Hamiltonian is one of the simplest Hamiltonians that describes the quantum spin Hall effect and edge states at the interface between inverted band HgTe quantum wells and normal insulators. The BHZ model has also been used to describe different quantum dot structures. Such examples include work done by Chang et al. [161–163] and Zhu et al. [164], who both numerically analyzed helical edge states in cylindrical quantum dots. Later on, Zhu et al. [165] numerically studied the effects of tensile strain on rectangular quantum dots along the horizontal axis, concluding that irrespective of the deformations, edge states are robust and the energy gap increases. In previous work, using an eight-band 3D $\vec{k} \cdot \vec{p}$ model, it was shown that edge states appeared as a function of the thickness of the quantum dot and/or applied strain [166].

Tight-binding models [167] have also been used to understand the electronic and optical properties of HgTe TI quantum dots, by e.g. Peeters et al. [168] and Delerue et al. [169]. Some of these tight-binding models [168, 169] have been used to investigate the edge states in HgTe TIs [168] and optical absorption in HgTe quantum rings [167]. Such approaches are, however, numerical in nature and do not allow for simple understanding of the physics of TI quantum dots.

In this chapter we present a theory of the electronic properties of quasi two-dimensional quantum dots made of topological insulators. The topological insulator is described by either an eight band $\vec{k} \cdot \vec{p}$ Hamiltonian or by a four-band $\vec{k} \cdot \vec{p}$ BHZ Hamiltonian. The trivial versus topological properties of the BHZ Hamiltonian

are characterized by the different topologies that arise when mapping the in-plane wavevectors through the BHZ Hamiltonian onto a Bloch sphere. In the topologically nontrivial case, edge states are formed in the disc and square geometries of the quantum dot. We account for the effects of compressive strain in topological insulator quantum dots by means of the Bir-Pikus Hamiltonian. Tuning strain allows topological phase transitions between topological and trivial phases, which results in the vanishing of edge states from the energy gap. This may enable the design of a quantum strain sensor based on strain-driven transitions in HgTe topological insulator square quantum dots.

5.1 Models

An example of a quasi-2D TI is a quantum well made of HgTe, embedded in a higher bandgap normal insulator material such as CdTe [141,166]. This structure is described by the effective quasi-2D BHZ $\vec{k}\cdot\vec{p}$ Hamiltonian, in which the wide bandgap insulator is replaced by a vacuum with an infinite energy gap. This avoids the uncertainties in $\vec{k}\cdot\vec{p}$ treatment of material interfaces [170, 171] but it implies that the wavefunction of an electron is zero at the physical edge of the nanostructure. Therefore, we need to determine the position of edge states away from the interface. In this chapter we study finite nanostructures of quasi-2D HgTe quantum dots as illustrated in Fig. 5.1 and described by the BHZ Hamiltonian. The results for the disc will be compared with the eight band $\vec{k}\cdot\vec{p}$ approach [166] and then, with the BHZ approach validated, the BHZ model will be applied to the square quantum dot.

In the $\vec{k}\cdot\vec{p}$ BHZ theory, the wavefunction of the spin-up electron in a quasi-2D layer of HgTe is written as a linear combination of electron $|e\uparrow\rangle$ and heavy hole $|hh\uparrow\rangle$ states: $|\varphi_k\uparrow\rangle = A_k e^{i\vec{k}\cdot\vec{r}}|e\uparrow\rangle + B_k e^{i\vec{k}\cdot\vec{r}}|hh\uparrow\rangle$ with a similar expansion for the spin-down electron.

The effective four-band Hamiltonian is given by the spin block diagonal BHZ

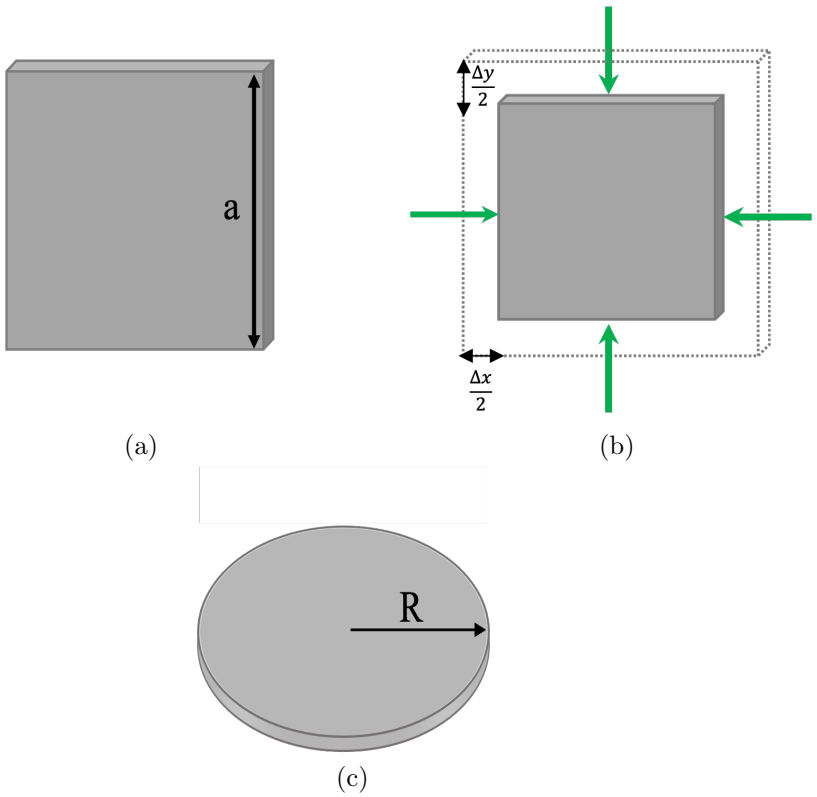

(a) (b)

(c)

Figure 5.1: Schematic pictures of quasi-2D HgTe TI quantum dot systems. (**a**) Square quantum dot unstrained. (**b**) Square quantum dot after undergoing compressive strain in the horizontal and vertical directions resulting in the quantum dot reducing in size in both directions. (**c**) Disc quantum dot.

Hamiltonian:

$$H_{BHZ} = \begin{pmatrix} H_{\uparrow} & 0 \\ 0 & H_{\downarrow} \end{pmatrix}. \tag{5.1}$$

The spin-up Hamiltonian $H_{\uparrow}$, acting on spinors (A_k, B_k), is given by

$$H_{\uparrow} = \begin{bmatrix} \frac{\Delta(k_x,k_y)}{2} & v_f(k_x - ik_y) \\ v_f(k_x + ik_y) & -\frac{\Delta(k_x,k_y)}{2} \end{bmatrix}, \tag{5.2}$$

where v_f is the Fermi velocity, $\Delta(k_x, k_y) = 2(M + B(k_x^2 + k_y^2))$ is the decoupled conduction and valence band quasi-particle energy, M is the energy gap, B is proportional to the inverse of the effective mass, and we take $\hbar = 1$.

The effective parameters M and B can be derived from a three-dimensional eight-band $\vec{k}\cdot\vec{p}$ theory for a given thickness of HgTe layer [166]. The spin-down Hamiltonian in Eq. (5.1) is given by $H_{\downarrow}(k) = H_{\uparrow}^{\star}(-k)$.

The Hamiltonian matrix in Eq. (5.2) can be written in the following compact Weyl Hamiltonian form (for spin-up):

$$H_{\uparrow} = \vec{d}\left(\vec{k}\right) \cdot \vec{\sigma}, \tag{5.3}$$

where pseudospin $\vec{\sigma}$ are the Pauli matrices in the space of electron and heavy hole states, and the vector $\vec{d}(\vec{k})$ is given by

$$\vec{d}\left(\vec{k}\right) = \left(v_f k_x, v_f k_y, \frac{\Delta(k_x, k_y)}{2}\right). \tag{5.4}$$

We will show later that the vector $\vec{d}\left(\vec{k}\right)$ maps the in-plane wavevectors k_x, k_y onto a Bloch sphere and characterizes the topology of the bulk energy bands.

5.1.1 Influence of strain

In this chapter, we study the influence of compressive strain in HgTe TI quantum dots as shown in Fig. 5.1b. We account for the effects of strain by introducing a four-band Bir-Pikus Hamiltonian derived from the eight-band Bir-Pikus Hamiltonian [166, 172]:

$$H_{\uparrow\downarrow}^{BP}(k) = \begin{bmatrix} \hat{t} & 0 \\ 0 & \hat{u} + \hat{v} \end{bmatrix}, \tag{5.5}$$

where the operators $\hat{t} = a_c(\varepsilon_{xx} + \varepsilon_{yy})$, $\hat{u} = a_v(\varepsilon_{xx} + \varepsilon_{yy})$ and $\hat{v} = \frac{1}{2}b(\varepsilon_{xx} + \varepsilon_{yy})$ are written in terms of the strain tensor matrix elements ε_{ij}, and deformation potentials a_c, a_v, and b. In this chapter, we utilize the deformation potential parameters found in van de Walle's work [173], namely $a_c = -4.60eV$, $a_v = -0.13eV$, and $b = -1.15eV$.

Following Novik et al.'s [172] approach, we add the spin-up Bir-Pikus Hamiltonian, Eq. (5.5), to the spin-up BHZ Hamiltonian, Eq. (5.2), resulting in the strain Hamiltonian:

$$H_{\uparrow}^{Strain}(k) = \begin{bmatrix} \frac{\Delta(k_x,k_y)}{2} - \frac{\gamma(\varepsilon)}{2} & v_f(k_x - ik_y) \\ v_f(k_x + ik_y) & -\frac{\Delta(k_x,k_y)}{2} + \frac{\gamma(\varepsilon)}{2} \end{bmatrix}, \tag{5.6}$$

where $\gamma(\varepsilon) = \hat{u}+\hat{v}-\hat{t}$ describes the relative shift of the conduction and valence bands of the HgTe TI [141]. $\gamma(\varepsilon)$ renormalizes the gap such that the Fermi level remains at $E = 0$ and can be found by taking a combination of energies at the bottom of the conduction band $E_c(k = 0)$ and top of the valence band $E_v(k = 0)$ at the Γ-point: $(E_c(k = 0)+E_v(k = 0))/2 = (\hat{t}+\hat{u}+\hat{v})/2$ and adding it to the Bir-Pikus Hamiltonian. Here $\gamma(\varepsilon)$ acts as a tuning parameter, driving the TI square quantum dot from the non-trivial, topological phase to the trivial, normal phase. The strain tensors adjust the width and height of the square by $\varepsilon_{xx} = \Delta x/x$ and $\varepsilon_{yy} = \Delta y/y$.

In this work, we consider the case when a square quantum dot is compressively strained in the horizontal and vertical directions as shown in Fig. 5.1b and compare our results to straining 3D HgTe TI disc quantum dots [166]. We then discuss the application of strained quantum dots as quantum strain sensors.

5.1.2 Energy levels and wavefunctions of HgTe nanostructures

In finite HgTe nanostructures, the motion of an electron is laterally confined by an external potential $V(x, y)$. The wavefunction $|\varphi_s \uparrow\rangle$ of the spin-up electron can be expressed as a linear combination of electron $|e \uparrow>$ and heavy hole $|hh \uparrow\rangle$ basis states and envelope functions $f(x, y)$ and $g(x, y)$:

$$|\varphi_s \uparrow\rangle = A_s f(x, y) |e \uparrow\rangle + B_s g(x, y) |hh \uparrow\rangle . \tag{5.7}$$

The envelope functions for the quantum dot level s satisfy the effective Schrödinger equation:

$$\begin{bmatrix} \frac{\Delta(\hat{p}_x,\hat{p}_y)}{2} + V(x, y) & v_f(\hat{p}_x - i\hat{p}_y) \\ v_f(\hat{p}_x + i\hat{p}_y) & -\frac{\Delta(\hat{p}_x,\hat{p}_y)}{2} - V(x, y) \end{bmatrix} \begin{bmatrix} A_s f(x, y) \\ B_s g(x, y) \end{bmatrix} = E_s \begin{bmatrix} A_s f(x, y) \\ B_s g(x, y) \end{bmatrix}, \tag{5.8}$$

where $\hat{p}_x = -i\partial/\partial x$ and $\hat{p}_y = -i\partial/\partial y$ are momentum operators acting on the envelope functions f and g.

5.1.3 Energy levels and wavefunction of HgTe quantum disc

Following the work in Ref. [166], we start our discussion of quantum dots with a circular quantum disc with radius R as shown in Fig. 5.1c, where the potential is infinite outside of the disc and zero inside. The wavefunction is a spinor characterized by pairs of angular momentum quantum numbers m in the conduction band and $m+1$ in the valence band for a state p. We expand the wavefunction in the basis of Bessel functions as:

$$|\Psi_m^p(r)\rangle = \sum_n A_n^{p,m}\phi_{n,m}(r)\,|e\rangle + \sum_s B_s^{p,m+1}\phi_{s,m+1}(r)\,|hh\rangle\,, \tag{5.9}$$

where $\phi_{n,m}(r) = \frac{\sqrt{2}}{R}\frac{1}{|J_{m+1}(\alpha_m^n)|}J_m(\alpha_m^n\frac{r}{R})\frac{1}{\sqrt{2\pi}}e^{im\varphi}$, $J_m(\alpha_m^n\frac{r}{R})$ is the Bessel function of order m, and α_m^n is the n-th zero of the Bessel function of order m.

The probability of an electron positioned at $r = r_0$ is given by:

$$\langle\Psi_m^p(r)|\,\delta(r-r_0)\,|\Psi_m^p(r)\rangle = \sum_{n,q}\left(A_n^{p,m}\right)^\star A_q^{p,m}\phi_{n,m}(r_0)\phi_{q,m}(r_0) + \sum_{s,w}\left(B_s^{p,m+1}\right)^\star B_w^{p,m+1}\phi_{s,m+1}(r_0)\phi_{w,m+1}(r_0). \tag{5.10}$$

The Hamiltonian, neglecting strain, in polar coordinates is given by

$$H_\uparrow = \begin{bmatrix} \frac{\Delta(\hat{k}_r)}{2} & v_f\hat{k}_- \\ v_f\hat{k}_+ & -\frac{\Delta(\hat{k}_r)}{2}\end{bmatrix}, \tag{5.11}$$

where $\frac{\Delta(\hat{k}_r)}{2} = M + B(-\frac{\partial^2}{\partial r^2} - \frac{1}{r}\frac{\partial}{\partial r} - \frac{1}{r^2}\frac{\partial^2}{\partial\varphi^2})$ is an intraband operator, and $\hat{k}_\mp = -ie^{i\varphi}(\frac{\partial}{\partial r}\mp i\frac{1}{r}\frac{\partial}{\partial\varphi})$ are operators connecting conduction and valence band states. Acting with the Hamiltonian in Eq. (5.11) on the wavefunction given in Eq. (5.9), we arrive at the set of equations for amplitudes A and B:

$$\varepsilon_{n,m}A_n^{m,p} + iv_f\sum_s\langle m,n|\,k_-\,|m+1,s\rangle\,B_s^{m+1,p} = E^{m,p}A_n^{m,p} \tag{5.12}$$

$$-iv_f \sum_s \langle m+1,n|\, k_+ \,|m,s\rangle\, A_s^{m,p} - \varepsilon_{n,m+1} B_n^{m+1,p} = E^{m,p} B_n^{m+1,p}, \tag{5.13}$$

where $\varepsilon_{n,m} = (M + B(\alpha_m^n)^2)$ and

$$\langle m,n|\, k_- \,|m+1,s\rangle = \frac{2}{R} \frac{J_{m+1}(\alpha_m^n)}{|J_{m+1}(\alpha_m^n)|} \frac{J_{m+2}(\alpha_{m+1}^s)}{|J_{m+2}(\alpha_{m+1}^s)|} \frac{\alpha_m^n \alpha_{m+1}^s}{(\alpha_m^n)^2 - (\alpha_{m+1}^s)^2}, \tag{5.14}$$

$$\langle m+1,n|\, k_+ \,|m,s\rangle = \frac{2}{R} \frac{J_{m+1}(\alpha_{m+1}^n)}{|J_{m+1}(\alpha_{m+1}^n)|} \frac{J_{m+2}(\alpha_m^s)}{|J_{m+2}(\alpha_m^s)|} \frac{\alpha_{m+1}^n \alpha_m^s}{(\alpha_{m+1}^n)^2 - (\alpha_m^s)^2}. \tag{5.15}$$

The eigenvectors $A_n^{m,p}$ and $B_s^{m,p}$, and eigenvalues $E^{m,p}$ are found by diagonalizing the Hamiltonian in Eqs. (5.12) and (5.13). The spin-down eigenvalues can be obtained analogously.

5.1.4 Energy levels and wavefunction of HgTe quantum square

Let us now consider an HgTe square TI quantum dot, finite in the x- and y-directions with side length a as shown in Fig. 5.1a. We seek the wavefunction for an electron in a square quantum well given in terms of trigonometric functions $f_{n,m}(x,y)$, where n and m are integer quantum numbers. Our wavefunction has the form:

$$|\Psi^p(x,y)\rangle = \sum_{n,m} A_{n,m}^p f_{n,m}(x,y)\,|e\rangle + \sum_{k,l} B_{k,l}^p f_{k,l}(x,y)\,|hh\rangle\,, \tag{5.16}$$

where $f_{n,m}(x,y) = \frac{2}{a} sin(\frac{n\pi x}{a}) sin(\frac{m\pi y}{a})$. The function $f_{n,m}(x,y)$ vanishes at the edges of the square.

Here the probability density of an electron positioned at $\vec{r} = \vec{r_0}$ can be found by:

$$\langle \Psi^p(x,y)|\, \delta(\vec{r} - \vec{r_0}) \,|\Psi^p(x,y)\rangle =$$
$$\sum_{n,m,q,r} \left(A_{n,m}^p\right)^\star A_{q,r}^p f_{n,m}(x_0,y_0) f_{q,r}(x_0,y_0) + \sum_{k,l,v,w} \left(B_{k,l}^p\right)^\star B_{v,w}^p f_{k,l}(x_0,y_0) f_{v,w}(x_0,y_0). \tag{5.17}$$

Acting with the Hamiltonian, Eq. (5.6), on the wavefunction, Eq. (5.16), gives us a system of equations for coefficients $A^p_{q,r}$ and $B^p_{q,r}$:

$$\left[M + B\left(\frac{q^2\pi^2}{a^2} + \frac{r^2\pi^2}{a^2}\right) - \frac{\gamma(\varepsilon)}{2}\right] A^p_{q,r} + v_f \sum_{kl} \langle qr| V |kl\rangle B^p_{kl} = E^p A^p_{q,r}, \quad (5.18)$$

$$v_f \sum_{nm} \langle qr| V |nm\rangle A^p_{nm} - \left[M + B\left(\frac{q^2\pi^2}{a^2} + \frac{r^2\pi^2}{a^2}\right) - \frac{\gamma(\varepsilon)}{2}\right] B^p_{q,r} = E^p B^p_{q,r}, \quad (5.19)$$

with strain given by parameter $\gamma(\varepsilon)$ and coupling matrix elements given by $\langle qr| V |kl\rangle = -i\delta_{r,l} \langle q| \partial_x |k\rangle - \delta_{q,k} \langle r| \partial_y |l\rangle$, and $\langle q| \partial_x |k\rangle = \langle q| \partial_y |k\rangle = \frac{2}{a}\frac{qk}{(k^2-q^2)}[(-1)^{q+k}-1]$ if $q \neq k$ otherwise $\langle q| \partial_x |k\rangle = \langle q| \partial_y |k\rangle = 0$ when $q+k$ is even and when $q = k$. The spin-up eigenvectors and eigenvalues can be found by diagonalizing Eqs. (5.18) and (5.19) while the spin-down eigenvectors and eigenvalues can be found similarly.

5.2 Results and discussion

We start our discussion with a study of the transition of the BHZ Hamiltonian from the topological phase to the normal phase as a function of its parameters. This is done by mapping the (k_x, k_y) plane onto the normal vector $\hat{n}(k_x, k_y) = \vec{d}(k_x, k_y)/|\vec{d}(k_x, k_y)|$ defined on a Bloch sphere following the analysis for topological insulators and superconductors as discussed by e.g. Alicea [174]. We follow with an analysis of the electronic properties of disc HgTe TI quantum dots and square HgTe TI quantum dots with and without applied strain obtained from numerically diagonalizing their respective Hamiltonians discussed in section 5.1. We then relate the emergence of edge states to strain by tuning the parameter $\gamma(\epsilon)$ until a topological phase transition occurs in square quantum dots.

5.2.1 Phase transitions in the bulk BHZ model

Here we discuss the existence of two phases in the BHZ Hamiltonian: the trivial (normal) and the non-trivial (topological). The trivial insulator leads to normal energy bands with $|hh\rangle$ states contributing to the valence band and $|e\rangle$ states contributing

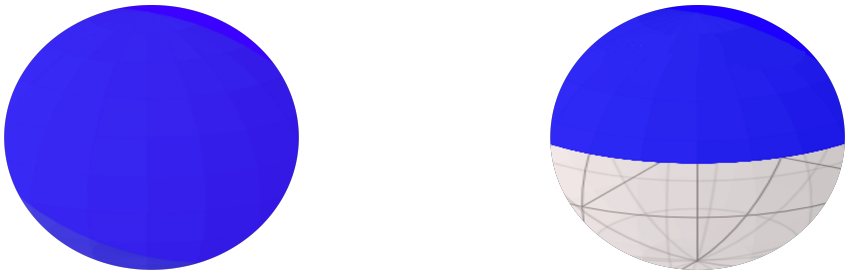

(a) (b)

Figure 5.2: Mapping $\vec{n}$ of the (k_x, k_y) plane represented by $-10 < k_x < 10$ and $-10 < k_y < 10$ region (with wavectors in nm^{-1}) onto a Bloch sphere for the (**a**) topological, inverted band regime where $M < 0$ and $B > 0$, and (**b**) topologically trivial regime with normally ordered bands for $M > 0$ and $B > 0$. The topology of the two Bloch spheres is different, (**b**) contains a hole and (**a**) does not. The parameters of the topological regime are $M = -150$meV, $B = 107$meV nm^2, and $v_f = 600$meVnm, while in the topologically trivial regime the parameters are $M = +150$meV, $B = 107$meVnm^2, and $v_f = 600$meVnm [166].

to the conduction band, while the non-trivial phase leads to a TI with inverted bands and edge states existing inside the bulk energy gap.

The bulk BHZ Hamiltonian, Eq. (5.3), $H_\uparrow = \vec{d}(k_x, k_y) \cdot \vec{\sigma}$, is entirely specified by the vector $\vec{d}(k_x, k_y)$. We relate the Hamiltonian to the topology by defining a vector $\hat{n}(k_x, k_y)$. The vector $\hat{n}$ maps the (k_x, k_y) plane onto the Bloch sphere. The topology of the mapping depends on parameters M, B, and v_f.

Fig. 5.2a shows the values of $\hat{n}(k_x, k_y)$ mapped onto a Bloch sphere for $M < 0$ (inverted bands) and $B > 0$. We see that the mapping converts the (k_x, k_y) plane onto the entire Bloch sphere. In Fig. 5.2b, we show the result of the mapping for $M > 0$ (normal bands) and $B > 0$, i.e., the sign of the energy gap is reversed. For this set of parameters, only the top part of the sphere is populated and there is a hole on the Bloch sphere. Clearly, the topology of the Bloch sphere is different for the trivial ($M > 0$) and topological ($M < 0$) insulators. Therefore, we can create a trivial or topological insulator by changing the sign of M and inverting the bands.

5.2.2 Edge states in the disc quantum dot

We now turn to the disc quantum dot. By comparison of results obtained using a quasi-2D BHZ model with 3D eight band $\vec{k} \cdot \vec{p}$ model we aim to validate the BHZ model

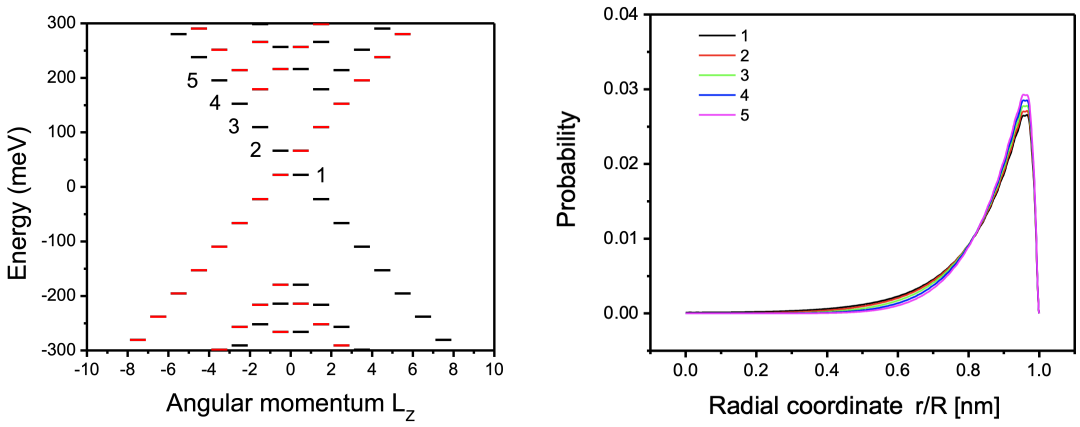

(a) (b)

Figure 5.3: (**a**) Spectrum of energy levels for a disc TI quantum dot as a function of total angular momentum $L_z = m + S_z$ where m is the orbital angular momentum and s_z is the spin for radius $R = 167$nm. Red levels correspond to spin down and black levels to spin up. Energy levels in the bulk gap are visible. (**b**) Electronic probability for states 1-5 shown in (**a**). The edge character of gap states and their position with respect to the edge are visible. The Hamiltonian in Eqs. (5.12) and (5.13) is numerically diagonalized with parameters $M = -150$meV, $B = 107$meVnm^2, and $v_f = 600$meVnm, corresponding to the topological regime.

and a develop better understanding of results obtained in the eight band model. In the disc the angular momentum $\hat{L}_z = m + \hat{s}_z$ is conserved. Here, $\hat{s}_z = \pm 1/2$ is the spin of the electron (up or down). For $\hat{s}_z = 1/2$, the energy spectrum as a function of $\hat{L}_z$ is obtained via a numerical diagonalization of Eqs. (5.12) and (5.13). For the opposite electron spin we formulate the appropriate equations arising from the Hamiltonian $H_\downarrow$. The eigenstates obtained for $\hat{s}_z = 1/2$ ($\hat{s}_z = -1/2$) are shown in Fig. 5.3a with black (red) bars.

Fig. 5.3a shows the energy levels of a disc with radius $R = 167$nm for parameters corresponding to the topological, inverted band regime with $M = -150$meV. We see a discrete spectrum of valence and conduction band states. Additionally, inside the energy gap, from -150meV to 150meV, we find a ladder of equally spaced edge states with linear dispersion as a function of angular momentum and energy bands. We see that the disc behaves like a finite edge of an HgTe TI nanoribbon [149], with periodic boundary conditions yielding a discrete energy spectrum with size quantization related to the circumference of the disc.

Fig. 5.3b shows the electronic probability as a function of the radial coordinate

for different edge states labeled in Fig. 5.3a. This electronic probability density is calculated using Eq. (5.10), by summing the eigenvectors for the angular momenta states in Fig. 5.3a. It is found that the electronic probability density peaks away from the physical edge and decays quickly into the center of the disc.

These results show that the electronic properties of the 2D four-band BHZ HgTe TI disc quantum dot are in agreement with previous works on 3D eight-band HgTe TI disc quantum dots in Ref. [166] and agree with BHZ results by Chang et al. [161]. Thus, we anticipate that the electronic properties and topological phase transitions found when compressively straining the 3D eight-band HgTe TI quantum dots will also be present when compressively straining the 2D four-band BHZ HgTe TI quantum dots.

5.2.3 Edge states and strain-driven transitions in the square quantum dot

Having validated the BHZ model we now turn to discussion of the energy spectrum of a square quantum dot as a function of strain obtained by diagonalizing Eqs. (5.18) and (5.19). The main difference between the quantum disc and a quantum square is the presence of sharp corners. We show below that these corners have zero electronic probability density, with edge states localized along the edges of the square. Fig. 5.4a-5.4d shows the evolution of the energy spectrum of the square quantum dot with lateral size $a = 40$nm and inverted bands as a function of applied strain while Fig. 5.4e-5.4h shows probability density of the corresponding lowest energy conduction band state. We see a discrete spectrum of quantized energy levels in the conduction and valence bands. In the topological inverted band regime (zero strain) in the energy window corresponding to a bulk gap, we see a ladder of equally spaced energy levels, Fig. 5.4a, with corresponding probability density localized at the edges of the square and expelled from the corners Fig. 5.4e. In Fig. 5.4a-5.4d, only the bulk bands are plotted as a function of momentum.

In Fig. 5.4e, the electronic probability density is plotted for the first energy state

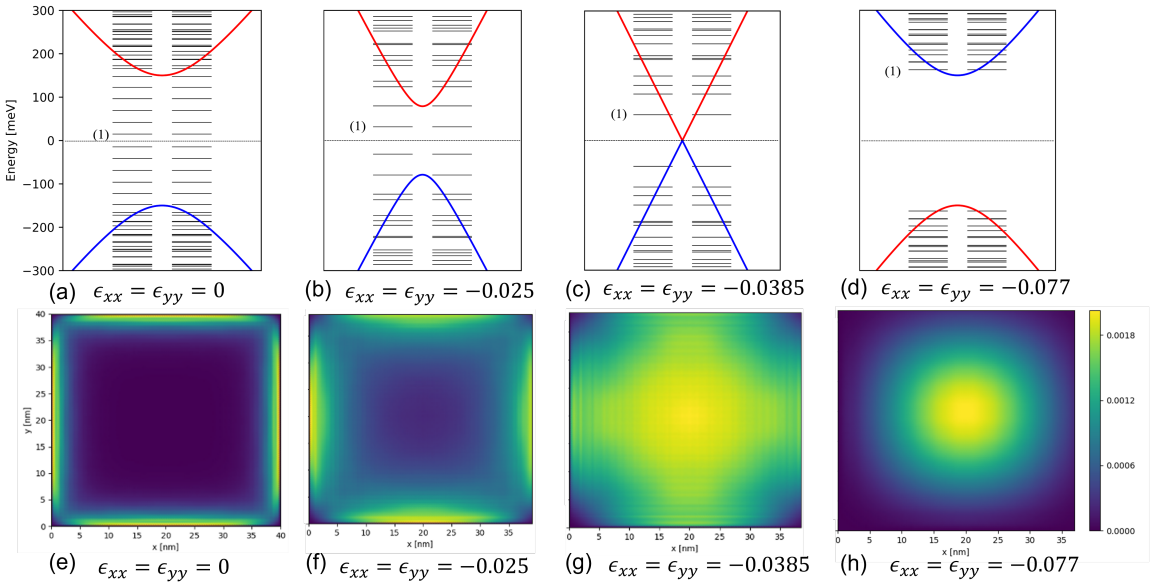

Figure 5.4: Energy spectra for four different cases of applied strain. (**a**) No strain applied, a topological insulator with a ladder of equally spaced energy levels in the gap of the bulk material is visible. (**b**) Some strain applied, the gap begins to close. (**c**) Dirac cone without edge states. (**d**) Normal insulator without states inside of the bulk gap. We see that by compressively straining the system, a topological phase transition occurs. The first energy level is labelled (1) and spin degenerate eigenvalues are shown next to each other and plotted together with the energy bands to show edge states inside the energy gap. The black dotted line at zero energy denotes the Fermi level. (**e**)-(**h**) color scale showing the probability of the first state above the Fermi level in (**a**)-(**d**). The parameters used in the diagonalization of the square quantum dot are the topological regime parameters: $M = -150\text{meV}$, $B = 107\text{meVnm}^2$, and $v_f = 600\text{meVnm}$.

above the Fermi level in Fig. 5.4a. The electronic probability density is obtained using Eq. (5.17). Fig. 5.4e also shows the formation of edge states localized along the edges of the square but approaching zero in the corners of the square. These edge states can be viewed as quantum rings [161], where electrons are localized along the sides of the squares and can tunnel from site to site. Thus, these edge states may be used as sites in the 1D Hubbard model.

Fig. 5.4 shows that by progressively applying compressive stress in the horizontal and vertical directions of the square quantum dot one causes the inverted bands to close. Then, as depicted in Figs. 5.4c and 5.4g, at the topological phase transition $\varepsilon_{xx} = -0.0385$ and $\varepsilon_{yy} = -0.0385$, the bands form a Dirac cone. Upon applying compressive strain beyond this threshold, the bands become normally ordered, a gap

free of edge states opens and states are localized inside the quantum dot. Therefore, under negative strain, the system is driven from the inverted band regime to the normal band regime and edge states disappear. Presence or absence of edge states can be detected in transport through the quantum dot. This is the principle of operation of the quantum strain sensor [166] based on TI HgTe quantum dots.

5.3 Conclusions

We presented here a contribution to the theory of the electronic properties of quasi two-dimensional nanostructures made of topological insulators (TIs). The TI quantum dots were described by the four-band BHZ Hamiltonian as well as a 3D eight band $\vec{k} \cdot \vec{p}$ model [166]. The trivial versus topological properties of the BHZ Hamiltonian were inferred from the mapping of the 2D wavevector plane through the BHZ Hamiltonian onto a Bloch sphere. In the topologically non-trivial case, edge states were found in the disc and square geometries. By tuning the compressive strain on the square quantum dot in the topologically non-trivial phase, the edge states began to disappear from the energy gap and after a significant amount of strain was applied, a topological phase transition occurred, causing the transition of TI to normal insulator and vanishing of edge states in a quantum dot. This allowed us to relate the emergence of edge states explicitly to transition from the normal to the inverted band regime tuned by applied strain to the square quantum dot and to the change in the topology of mapping the BHZ Hamiltonian onto Bloch spheres.

We show that for a square quantum dot edge states have vanishing probability density at the corners so electrons are localised along each edges. These localised states would play the role of sites in the Hubbard model once they are populated with electrons which would interact strongly if they are on the same site. The existence of localized 1D edge states may enable the design of quasi-one-dimensional quantum rings with localized electronic states along the sides of the square, acting as tunable one-dimensional Hubbard models once populated with interacting electrons. The presence or absence of edge states and hence modification of their electronic properties

are found to be controlled by strain. Strain-driven topological phase transitions can be detected in transport and serve as a basis for quantum strain sensors based on HgTe quantum dots in topological insulators.

Chapter 6

Theory of Excitons in Gated Bilayer Graphene Quantum Dots

We would like to state that this chapter is based on Ref. [87] except with more details shown. I have performed all mentioned calculations in this chapter except for DFT fitting procedures.

There is currently great interest in semiconductor quantum dots (QDs) as building blocks of quantum technology. This includes lateral gated QDs confining either spins of electrons or holes for quantum computation [43, 175, 176], self-assembled QDs and nanoplatelets confining electrons and holes for emitters, detectors, lasers, displays, and single and entangled photon pair sources [177–181]. The gated lateral QDs allow for high tunability of their electronic properties, but are limited to confining either electrons or holes, while self-assembled dots confine both electrons and holes, but are difficult to tune. Simultaneously, with the development of QDs in semiconductors, a new class of two-dimensional semiconductors was developed based on bilayer graphene (BLG). Optical properties of BLG were studied in the context of stage 2 intercalated graphite [182, 183]. However, the isolation of a single BLG layer enables application of a vertical electric field, which opens the energy gap [18, 26, 29, 184, 185]. Hence, BLG turns out to be a voltage-tunable semiconductor with the energy gap in the THz to FIR range [186].

In 2009, motivated by the tunable bandgap in BLG, Park and Louie [187] predicted the excitonic spectrum of BLG, relating the optical selection rules to the Berry's phase and strong electron-hole interactions. Soon Ju et al. [185] experimentally observed excitons in BLG using photocurrent spectroscopy. They found two bright absorption peaks with the $2p$ exciton being the dominant bright peak, as predicted in Refs. [187, 188]. This remarkable behaviour was attributed to the pseudospin winding number of 2 found in BLG [29, 30, 187, 189]. In 2007, Pereira et al. [38] proposed a lateral confining potential realized by position-dependent doping, confining both an electron and a hole. Furthermore, they showed that the pseudospin winding number of 2 has a dramatic effect on the angular momentum dependence of the QD spectrum, different than that of conventional semiconductors. Not only was this proposed system able to confine both electrons and holes, but was also tunable through the use of gates. Soon several groups constructed gated lateral QDs in BLG and demonstrated confinement of either electrons or holes [31, 34]. Further experimental studies of gated BLG were carried out in Refs. [37,64,190], where either confined electron or hole levels have been realized. The work on electron-electron interactions on the example of two-electron complexes was reported in Refs. [39, 64, 110], where an unusual two-particle ground state, a spin-triplet but valley-singlet, was demonstrated.

In this chapter we establish that lateral gated QDs in BLG confine simultaneously electrons and holes through the confining potential proposed in Ref. [38]. We develop a theory of such an interacting two-particle complex forming an exciton in gated BLG QDs. We start with a multi-million-atom computational box of BLG, in which we introduce vertical and lateral gates. We determine the effective lateral confining potential using ab-inito methods. We next compute confined QD levels in the valence and conduction band. We then calculate microscopic Coulomb interaction matrix elements [101], the quasi-particle spectrum and the exciton spectrum by solving the Bethe-Salpeter equation (BSE). Using excitonic states and computed dipole matrix elements, we predict the exciton fine structure and a nontrivial absorption spectrum.

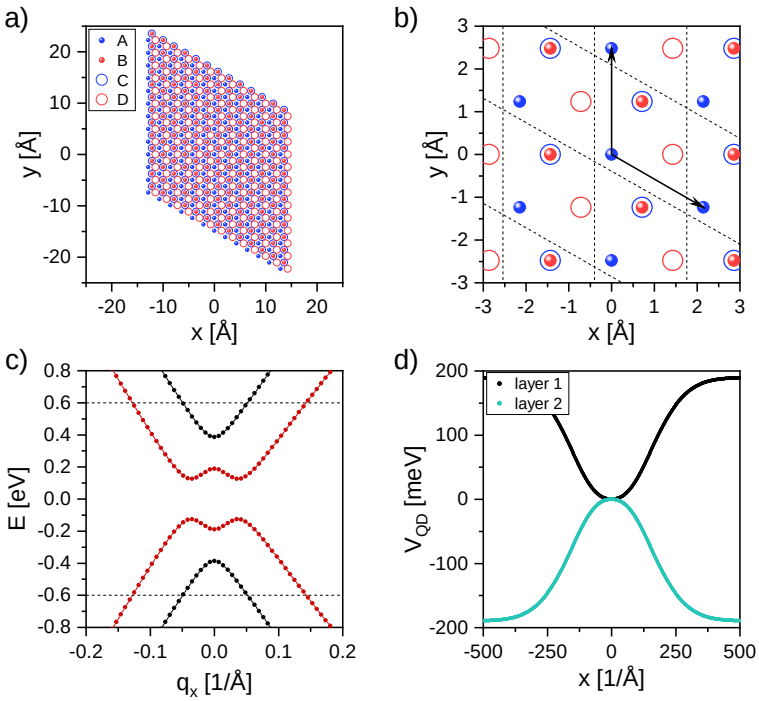

Figure 6.1: a) Bilayer graphene computational box. The rhomboidal geometry is not to scale. Sublattices A, B (layer 1), C, D (layer 2) are shown. (b) the lattice vectors and the Bernal stacking . (c) the bulk band structure of BLG in the vicinity of $\vec{K}$-point. applied voltage $V \approx 0.38$ eV, $\gamma_0 \approx -2.5$ eV and $\gamma_1 \approx 0.34$ eV . States within energy window $E_{cut} = 600$ meV are retained in our calculations. (d) confing potential V(x) on layer 1 (black) and 2(green). The potential confines electrons on one layer, and holes on the other for a QD radius $R_{QD} = 20$ nm.

6.1 Bulk bilayer graphene

We consider two Bernal-stacked layers (discussed in section. 2.1.2) of graphene as shown in Fig. 6.1(a) and (b). The sublattices are labelled A, B, C, D. We choose the real-space computational box to be rhomboidal, as shown in Fig. 6.1 (a) (drawn not to scale). Sublattices A and B belong to the layer 1 while sublattices C and D compose the layer 2. The nearest-neighbor in-plane bond length is $a = 0.143$ nm and the distance between layers is $h = 0.335$ nm. The sublattice B on layer 1 and the sublattice C on layer 2 are coupled as shown in Fig. 6.1(b), and the unit vectors are defined as $\vec{a_1} = a\left(0, \sqrt{3}\right)$ and $\vec{a_2} = a\left(\frac{3}{2}, \frac{\sqrt{3}}{2}\right)$. The computational box containing our BLG structure is generated by taking $M_1 = M_2$ unit cells along the $\vec{a}_1$

and $\vec{a}_2$ directions. The total number of Carbon atoms in the computational box with $M_1 = 633$ is 1602756. To remove the finite-size effects, we impose periodic boundary conditions connecting the opposite edges of the rhombus. We apply an external electric field (the displacement field) perpendicular to the surface. The applied voltage is $+V/2$ on layer 1 and $-V/2$ on layer 2 so that the potential difference between layers is V. We define our Bloch wavefunction for this system as

$$|\phi_{\vec{k},l}\rangle = \frac{1}{\sqrt{M}} \sum_{\vec{R}} e^{i\vec{k}\cdot\left(\vec{R}+\vec{d}_l\right)} |\psi_{\vec{R},l}\rangle, \tag{6.1}$$

where $M = M_1 M_2$ is the number of unit cells, and $|\psi_{\vec{R},l}\rangle$ is a p_z Slater orbital localized on unit cell $\vec{R}$ and sublattice l. $\vec{d}_l$ is the position of sublattice l within a unit cell taken to be

$$\vec{d}_A = \quad (0,0,0)\,, \tag{6.2a}$$

$$\vec{d}_B = \quad \vec{b}, \tag{6.2b}$$

$$\vec{d}_C = \quad \vec{b} - h\hat{z}, \tag{6.2c}$$

$$\vec{d}_D = \quad \vec{a}_2 - \vec{b} - h\hat{z}, \tag{6.2d}$$

where $\vec{b} = \left(\frac{1}{2}a, \frac{\sqrt{3}}{2}a\right)$. The computational rhombus defined in Fig. 6.1 is constructed by periodically repeating the unit cell containing four atoms, one for each of the four sublattices, spanned by two basis vectors $\vec{a}_1$ and $\vec{a}_2$ defined in Fig. 6.1(b). One can obtain the allowed $\vec{k}$ points by imposing $u^l_k(\vec{r}) = u^l_k(\vec{r}+M\vec{a}_1)$ and $u^l_k(\vec{r}) = u^l_k(\vec{r}+M\vec{a}_2)$ where $\phi_{\vec{k},l}(\vec{r}) = e^{i\vec{k}\cdot\vec{r}} u^l_k(\vec{r})$ defines our Bloch function. This gives two conditions:

$$e^{-iM\vec{k}\cdot\vec{a_1}} = 1, \tag{6.3a}$$

$$e^{-iM\vec{k}\cdot\vec{a_2}} = 1. \tag{6.3b}$$

Using the definitions of $\vec{a}_1$, and $\vec{a}_2$ we get

$$a_{1x}k_xM + a_{1y}k_yM = 2\pi n_1 \tag{6.4a}$$

$$a_{2x}k_xM + a_{2y}k_yM = 2\pi n_2. \tag{6.4b}$$

Solving for k_x in Eq. 6.4(a) and plugging into Eq. 6.4(b) we get

$$\begin{aligned}
a_{2x}\frac{\left(\frac{2\pi n_1}{M} - a_{1y}k_y\right)}{a_{1x}} + a_{2y}k_y &= \frac{2\pi n_2}{M} \\
-\frac{a_{2x}a_{1y}k_y}{a_{1x}} + a_{2y}k_y &= \frac{2\pi n_2}{M} - \frac{a_{2x}}{a_{1x}}\frac{2\pi n_1}{M} \\
\frac{a_{2y}a_{1x} - a_{2x}a_{1y}}{a_{1x}}k_y &= \frac{2\pi n_2}{M} - \frac{a_{2x}}{a_{1x}}\frac{2\pi n_1}{M} \\
k_y &= \frac{2\pi}{a_{2y}a_{1x} - a_{2x}a_{1y}}\left(-a_{2x}\frac{n_1}{M} + a_{1x}\frac{n_2}{M}\right).
\end{aligned} \tag{6.5}$$

Now solving for k_y in Eq. 6.4(b) and plugging into Eq. 6.4(a) we get

$$\begin{aligned}
a_{1x}k_x + a_{1y}\frac{\left(\frac{2\pi n_2}{M} - a_{2x}k_x\right)}{a_{2y}} &= \frac{2\pi n_1}{M} \\
a_{1x}k_x - \frac{a_{1y}a_{2x}k_x}{a_{2y}} &= \frac{2\pi n_1}{M} - \frac{a_{1y}}{a_{2y}}\frac{2\pi n_2}{M} \\
\frac{a_{2y}a_{1x} - a_{2x}a_{1y}}{a_{2y}}k_x &= \frac{2\pi n_1}{M} - \frac{a_{1y}}{a_{2y}}\frac{2\pi n_2}{M} \\
k_x &= \frac{2\pi}{a_{2y}a_{1x} - a_{2x}a_{1y}}\left(a_{2y}\frac{n_1}{M} - a_{1y}\frac{n_2}{M}\right).
\end{aligned} \tag{6.6}$$

This allows us to write

$$\vec{k} = \frac{2\pi}{a_{2y}a_{1x} - a_{2x}a_{1y}}\left[\left(\frac{n_1}{M}a_{2y} - \frac{n_2}{M}a_{1y}\right)\hat{k_x} + \left(-\frac{n_1}{M}a_{2x} + \frac{n_2}{M}a_{1x}\right)\hat{k_y}\right], \tag{6.7}$$

where $n_1 = -(M-1)/2...(M-1)/2$ and similarly for n_2.

Our wavefunction for the bulk system is given as

$$|\Phi^p_{\vec{k}}\rangle = \sum_l A^p_{\vec{k},l}\,|\phi_{\vec{k},l}\rangle\,, \tag{6.8}$$

where p labels band, l labels atom in the unit cell and $A^p_{\vec{k},l}$ are coefficients obtained by solving the Schrodinger equation. The Hamiltonian in the basis of sublattices A,

B, C, D is given by

$$\mathbf{H}_{bulk}(\vec{k}) = \begin{pmatrix} \frac{V}{2} & \gamma_0 f\left(\vec{k}\right) & 0 & 0 \\ \gamma_0 f^*\left(\vec{k}\right) & \frac{V}{2} & \gamma_1 & 0 \\ 0 & \gamma_1 & -\frac{V}{2} & \gamma_0 f\left(\vec{k}\right) \\ 0 & 0 & \gamma_0 f^*\left(\vec{k}\right) & -\frac{V}{2} \end{pmatrix}. \tag{6.9}$$

Here, γ_0 and γ_1 are the intralayer and interlayer nearest neighbour (NN) hopping terms, respectively, and $+V/2$ and $-V/2$ are potentials on the top and bottom layer due to the applied vertical electric field. We neglect the trigonal warping term as we are focusing on strong confinement. The effects of the trigonal warping reduces the symmetry of the bulk system from C_∞ to C_3 introducing additional bright states in the bulk BLG absorption spectrum [188]. Unlike in $\vec{k}\cdot\vec{p}$ calculations, we perform atomistic calculations which already include the C_3 symmetry.

If we define the following eigenvectors

$$\mathbf{A}^p_k(\vec{k}) = \begin{pmatrix} \tilde{A}^p_{\vec{k},A} \\ \tilde{A}^p_{\vec{k},B} e^{-i\phi_{\vec{k}}} \\ \tilde{A}^p_{\vec{k},C} e^{-i\phi_{\vec{k}}} \\ \tilde{A}^p_{\vec{k},D} e^{-2i\phi_{\vec{k}}} \end{pmatrix}, \tag{6.10}$$

then the bulk Hamiltonian defined in Eq. 6.9 in the basis of $\tilde{A}^p_{\vec{k},l}$ becomes completely real. It is given by

$$\mathbf{H}_{bulk}(\vec{k}) = \begin{pmatrix} \frac{V}{2} & \gamma_0 \left|f\left(\vec{k}\right)\right| & 0 & 0 \\ \gamma_0 \left|f\left(\vec{k}\right)\right| & \frac{V}{2} & \gamma_1 & 0 \\ 0 & \gamma_1 & -\frac{V}{2} & \gamma_0 \left|f\left(\vec{k}\right)\right| \\ 0 & 0 & \gamma_0 \left|f\left(\vec{k}\right)\right| & -\frac{V}{2} \end{pmatrix}. \tag{6.11}$$

We can now diagonalize Eq. 6.11 at each point $\vec{k}$ defined in Eq. 6.7 to obtain the energies and wavefunctions for the bulk. Figure 6.1(c) shows the band structure calculated for the intralayer tunneling matrix element $\gamma_0 = -2.5$ eV , the interlayer tunneling matrix element $\gamma_1 = 0.34$ eV, and the displacement voltage comparable to the interlayer tunneling, $V = 0.38$ eV. The values of γ_0 and γ_1 were obtained by fitting the tight-binding parameters to ab-initio DFT calculations of the bulk BLG

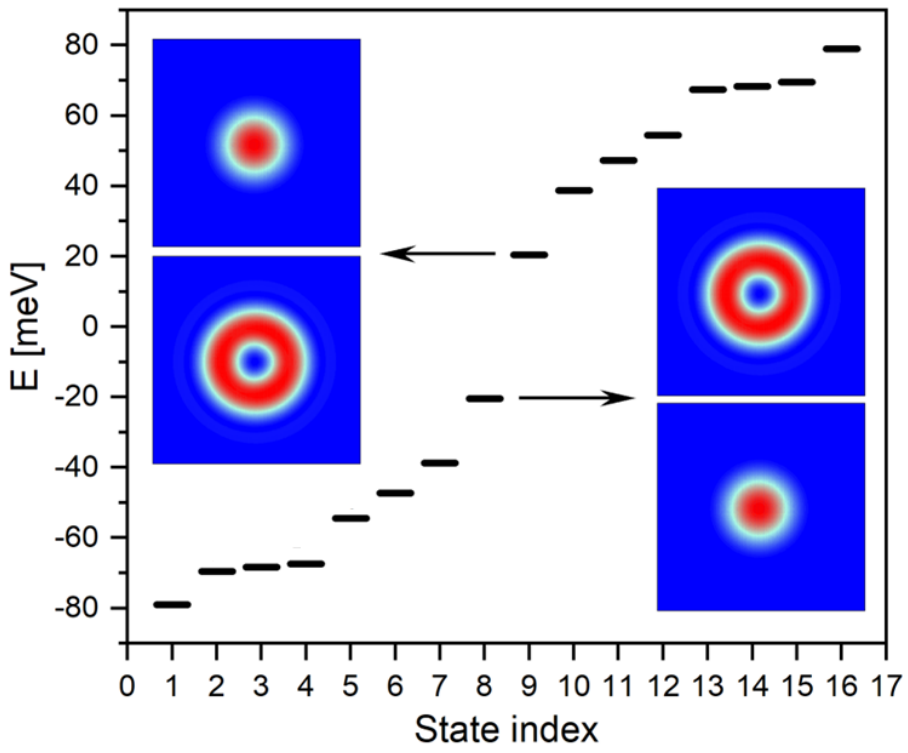

Figure 6.2: Spectrum of quantum dot energy levels as a function of level index for the $-\vec{K}$ valley of the gated bilayer graphene QD. Inset shows the wavefunctions of level (8) and level (9) , upper plots showing the probability density on layer 1, the lower plot on layer 2.

bandstructure. In the absence of the electric field bulk BLG is gapless [15–17,183,191], but the applied electric field opens an energy gap [17–26] visible in Fig. 6.1(c). At the $\vec{K}$ point of the Brillouin zone, the states corresponding to the edges of the low-energy conduction and valence bands are localized on the uncoupled sublattices A and D, respectively, with a phase difference of $2\phi_k$, which generates a Berry phase of 2π [15–17, 29, 30]. We also see that the opening of the gap is associated with a characteristic conduction and valence band dispersion resembling a Mexican hat, with the density of states diverging at the bottom of the conduction and top of the valence band, in analogy to one-dimensional systems.

6.2 Gated bilayer graphene quantum dot

Our goal is to confine electrons and holes laterally in the center of the computational rhombus. This is done by applying a lateral potential in its center, which is attractive for electrons on layer 1 and repulsive for electrons (attractive for holes) on layer 2. This can be accomplished by removing a circular, disc-like element from the top and bottom gate. The resulting confining potential due to removed gates can be approximated by simple Gaussian potentials for the top ($z = 0$) and bottom ($z = -h$) layers of the form

$$V_{QD}(\rho) = \begin{cases} -(V/2)e^{-\frac{\rho^2}{R_{QD}^2}} & z = 0, \\ +(V/2)e^{-\frac{\rho^2}{R_{QD}^2}} & z = -h, \end{cases} \tag{6.12}$$

where ρ is the 2D radial coordinate. This type of potential was also proposed in Refs. [38, 39]. We see that the voltage drop of $-V/2$ on the top layer in the center of the dot exactly cancels the applied bulk voltage $+V/2$. A similar cancellation is observed on the bottom layer. Hence, the vertical electric field is zero in the center of the QD and approaches the applied electric field far away from the center. Since the applied vertical electric field at each radius ρ redistributes charges, we seek to extract an effective potential $V(\rho)$ that takes into account the screening of the applied field in the gated system. This is done by performing *ab-initio* calculations for biased bulk BLG with a voltage drop $V_{QD}(\rho)$ at radius ρ resulting in a new screened voltage drop $V_{QD}^{eff}(\rho)$. We then fit this effective potential using a sum of Gaussians. Two Gaussians are sufficient, and the fitting yields our new effective potential given by

$$V_{QD}^{eff}(\rho) = \begin{cases} -(c_1 e^{-\frac{\alpha_1 \rho^2}{R_{QD}^2}} + c_2 e^{-\frac{\alpha_2 \rho^2}{R_{QD}^2}}) & z = 0, \\ +(c_1 e^{-\frac{\alpha_1 \rho^2}{R_{QD}^2}} + c_2 e^{-\frac{\alpha_2 \rho^2}{R_{QD}^2}}) & z = -h, \end{cases} \tag{6.13}$$

with parameters $c_1 = -0.01763$ eV, $c_2 = 0.20726$ eV, $\alpha_1 = 6.128$, and $\alpha_2 = 1.0064$ for a fixed QD radius $R_{QD} = 20$ nm.

Figure 6.1(d) shows a slice of the full single-particle potential along the x direction. This potential includes the vertical electric field and the double-Gaussian quantum

dot potential given above. Our new Hamiltonian for the gated BLG QD can now be written as

$$\hat{H} = \hat{H}_{bulk} + \hat{V}_{QD}^{eff}. \tag{6.14}$$

To find the single-particle states and energies we expand our wavefunction $|\varphi^s\rangle$ in the basis of the eigenstates of the computational rhombus $|\Phi_{\vec{k}}^p\rangle$. We confine ourselves to the low energy spectrum taking a cutoff $E_{cut} = 600$ meV as shown in Fig. 6.1 (c). This corresponds to a total basis size (including both valleys) of 18752 and samples the higher energy bands as well as the low energy bands. Writing our wavefunction explicitly, we have

$$|\varphi^s\rangle = \sum_{\vec{k}} \sum_{p} B_{p,\vec{k}}^s \, |\Phi_{\vec{k}}^p\rangle \,, \tag{6.15}$$

where s labels our QD state. Acting the Hamiltonian in Eq. 6.14 on Eq. 6.15 we have

$$\left[H_{bulk} + \hat{V}_{QD}^{eff}\right] \sum_{\vec{k}} \sum_{p} B_{p,\vec{k}}^s \, |\Phi_{\vec{k}}^p\rangle = E_s \sum_{\vec{k}} \sum_{p} B_{p,\vec{k}}^s \, |\Phi_{\vec{k}}^p\rangle \,, \tag{6.16}$$

projecting $\langle \Phi_{\vec{k}'}^{p'}|$ we have

$$\sum_{p} B_{p,\vec{k}}^s \, \langle \Phi_{\vec{k}'}^{p'} | H_{bulk} | \Phi_{\vec{k}}^p \rangle + \sum_{p} B_{p,\vec{k}}^s \, \langle \Phi_{\vec{k}'}^{p'} | \hat{V}_{QD}^{eff} | \Phi_{\vec{k}}^p \rangle \sum_{\vec{k}} = E_s \sum_{\vec{k}} \sum_{p} B_{p,\vec{k}}^s \, \langle \Phi_{\vec{k}'}^{p'} | \Phi_{\vec{k}}^p \rangle \,. \tag{6.17}$$

Since $\Phi_{\vec{k}'}^{p'}$ are eigenstates of the bulk Hamiltonian we get

$$\epsilon_{p,\vec{k}} B_{p,\vec{k}}^s + \sum_{\vec{k}',p'} B_{p',\vec{k}'}^s \, \langle \Phi_{\vec{k}}^p | \hat{V}_{QD}^{eff} | \Phi_{\vec{k}'}^{p'} \rangle = E_s B_{p,\vec{k}}^s, \tag{6.18}$$

where $\epsilon_{p,\vec{k}}$ are the energies obtained by diagonalizing Eq. 6.11. We will now derive $\langle \Phi_{\vec{k}}^p | \hat{V}_{QD}^{eff} | \Phi_{\vec{k}'}^{p'} \rangle$. We have

$$\langle \Phi_{\vec{k}}^p | \hat{V}_{QD}^{eff} | \Phi_{\vec{k}'}^{p'} \rangle = \sum_{l,l'} A_{\vec{k},l}^{*p} A_{\vec{k}',l'}^{p'} \, \langle \phi_{\vec{k},l} | \hat{V}_{QD}^{eff} | \phi_{\vec{k}',l'} \rangle \,, \tag{6.19}$$

using Eq. 6.1 we get

$$\langle \Phi^p_{\vec{k}} | \hat{V}^{eff}_{QD} | \Phi^{p'}_{\vec{k}'} \rangle = \frac{1}{M} \sum_{l,l'} \sum_{\vec{R},\vec{R}'} A^{*p}_{\vec{k},l} A^{p'}_{\vec{k}',l'} e^{-i\vec{k}\cdot\left(\vec{R}+\vec{d}_l\right)} e^{i\vec{k}'\cdot\left(\vec{R}'+\vec{d}_{l'}\right)} \langle \psi_{\vec{R},l} | \hat{V}^{eff}_{QD} | \psi_{\vec{R}',l'} \rangle . \quad (6.20)$$

Assuming $\hat{V}^{eff}_{QD}$ is slowly varying such that the potential within a unit cell is constant, then $\hat{V}^{eff}_{QD}(\rho_i) \approx \hat{V}^{eff}_{QD}\left(\frac{\vec{R}+\vec{R}'}{2}\right)$, so we have

$$\langle \Phi^p_{\vec{k}} | \hat{V}^{eff}_{QD} | \Phi^{p'}_{\vec{k}'} \rangle = \frac{1}{M} \sum_{l,l'} \sum_{\vec{R},\vec{R}'} A^{*p}_{\vec{k},l} A^{p'}_{\vec{k}',l'} e^{-i\vec{k}\cdot\left(\vec{R}+\vec{d}_l\right)} e^{i\vec{k}'\cdot\left(\vec{R}'+\vec{d}_{l'}\right)} \hat{V}^{eff}_{QD}\left(\frac{\vec{R}+\vec{R}'}{2}\right) \delta_{\vec{R},\vec{R}'} \delta_{l,l'}. \quad (6.21)$$

Executing the deltas, we get

$$\langle \Phi^p_{\vec{k}} | \hat{V}^{eff}_{QD} | \Phi^{p'}_{\vec{k}'} \rangle = \frac{1}{M} \sum_{l} e^{i(\vec{k}'-\vec{k})\cdot\vec{d}_l} A^{*p}_{\vec{k},l} A^{p'}_{\vec{k}',l} \sum_{\vec{R}} e^{i(\vec{k}'-\vec{k})\cdot\vec{R}} \hat{V}^{eff}_{QD}\left(\vec{R}\right), \quad (6.22)$$

then define $V_{\vec{k},\vec{k}',l} = \frac{1}{M}\sum_{\vec{R}} e^{i(\vec{k}'-\vec{k})\cdot\vec{R}} \hat{V}^{eff}_{QD}\left(\vec{R}\right)$ and we get

$$\langle \Phi^p_{\vec{k}} | \hat{V}^{eff}_{QD} | \Phi^{p'}_{\vec{k}'} \rangle = \sum_{l} A^{*p}_{\vec{k},l} A^{p'}_{\vec{k}',l} e^{i\left(\vec{k}'-\vec{k}\right)\cdot d_l} V^{eff}_{\vec{k},\vec{k}',l}, \quad (6.23)$$

with $V^{eff}_{\vec{k},\vec{k}',l}$ being the Fourier transform of the confining potential. Since our quantum dot potential differs only by a sign on different layers, we will solve this only for a single layer. It is worth noting that the Fourier transform of a Gaussian in 1D is

$$\begin{aligned}
F(e^{-\frac{R^2}{R^2_{QD}}}) &= \frac{1}{\sqrt{2\pi}} \int_{-\infty}^{\infty} dR e^{-iqR} e^{-\frac{R^2}{R^2_{QD}}} \\
&= \frac{1}{\sqrt{2\pi}} \int_{-\infty}^{\infty} dR e^{-\left(\frac{R}{R_{QD}}+\frac{iqR_{QD}}{2}\right)^2 - \frac{q^2R^2_{QD}}{4}} \\
&= \frac{1}{\sqrt{2\pi}} e^{-\frac{q^2R^2_{QD}}{4}} \int_{-\infty}^{\infty} dR e^{-\left(\frac{R}{R_{QD}}+\frac{iqR_{QD}}{2}\right)^2} \\
&= \frac{1}{\sqrt{2\pi}} R_{QD} e^{-\frac{q^2R^2_{QD}}{4}} \int_{-\infty}^{\infty} du e^{-u^2} \\
&= \sqrt{\frac{R^2_{QD}}{2}} e^{-\frac{R^2_{QD}q^2}{4}},
\end{aligned} \quad (6.24)$$

and so the inverse transform in 1D can yield

$$e^{-\frac{R^2}{R_{QD}^2}} = \frac{1}{\sqrt{2\pi}}\sqrt{\frac{R_{QD}^2}{2}}\int_{-\infty}^{\infty} dq e^{iqR} e^{-\frac{R_{QD}^2 q^2}{4}}. \tag{6.25}$$

We can easily extrapolate to 2D and get

$$e^{-\frac{R^2}{R_{QD}^2}} = \frac{R_{QD}^2}{4\pi}\int_{-\infty}^{\infty} d\vec{q} e^{i\vec{q}\cdot\vec{R}} e^{-\frac{R_{QD}^2 q^2}{4}}. \tag{6.26}$$

For our discrete grid of our rhombus we have

$$e^{-\frac{R^2}{R_{QD}^2}} = A\frac{R_{QD}^2}{4\pi}\sum_{\vec{q}} e^{i\vec{q}\cdot\vec{R}} e^{-\frac{R_{QD}^2 q^2}{4}}, \tag{6.27}$$

where A corresponds to the smallest area in our reciprocal space (k-space in our case and thus the area of a unit cell). Now with this at hand, let us compute $V^{eff}_{\vec{k},\vec{k}',l}$ for layer 1:

$$V^{eff}_{\vec{k},\vec{k}',1} = \sum_{\vec{R}} e^{i(\vec{k}'-\vec{k})\cdot\vec{R}} V^{eff}_{QD}\left(\vec{R}\right). \tag{6.28}$$

Plugging in Eq. 6.13 we get

$$\begin{aligned}
V^{eff}_{\vec{k},\vec{k}',1} &= \frac{1}{M}\sum_{\vec{R}} e^{i(\vec{k}'-\vec{k})\cdot\vec{R}}\left[-c_1 e^{-\frac{\alpha_1\rho_i^2}{R_{QD}^2}} - c_2 e^{-\frac{\alpha_2\rho_i^2}{R_{QD}^2}}\right] \\
&= A\frac{R_{QD}^2}{4\pi}\sum_{\vec{q}}\frac{1}{M}\sum_{\vec{R}} e^{i(\vec{k}'-\vec{k}+\vec{q})\cdot\vec{R}}\left[-\frac{c_1}{\alpha_1}e^{-\frac{R_{QD}^2 q^2}{4\alpha_1}} - \frac{c_2}{\alpha_2}e^{-\frac{R_{QD}^2 q^2}{4\alpha_2}}\right] \\
&= A\frac{R_{QD}^2}{4\pi}\sum_{\vec{q}}\left[-\frac{c_1}{\alpha_1}e^{-\frac{R_{QD}^2 q^2}{4\alpha_1}} - \frac{c_2}{\alpha_2}e^{-\frac{R_{QD}^2 q^2}{4\alpha_2}}\right]\frac{1}{M}\sum_{\vec{R}} e^{i(\vec{k}'-\vec{k}+\vec{q})\cdot\vec{R}} \\
&= A\frac{R_{QD}^2}{4\pi}\sum_{\vec{q}}\left[-\frac{c_1}{\alpha_1}e^{-\frac{R_{QD}^2 q^2}{4\alpha_1}} - \frac{c_2}{\alpha_2}e^{-\frac{R_{QD}^2 q^2}{4\alpha_2}}\right]\delta_{\vec{k}'-\vec{k},\vec{q}} \\
&= A\frac{R_{QD}^2}{4\pi}\left[-\frac{c_1}{\alpha_1}e^{-\frac{R_{QD}^2|\vec{k}'-\vec{k}|}{4\alpha_1}} - \frac{c_2}{\alpha_2}e^{-\frac{R_{QD}^2|\vec{k}'-\vec{k}|}{4\alpha_2}}\right],
\end{aligned} \tag{6.29}$$

where A is the area of our unit cell, it is given by $A = \frac{8\pi^2}{3\sqrt{3}Ma^2}$. Finally, gathering everything, we can write

$$V^{eff}_{\vec{k},\vec{k}',l} = \pm Q^2 R_{QD}^2\left[\frac{c_1}{\alpha_1}e^{-\frac{R_{QD}^2|\vec{k}'-\vec{k}|^2}{4\alpha_1}} + \frac{c_2}{\alpha_2}e^{-\frac{R_{QD}^2|\vec{k}'-\vec{k}|^2}{4\alpha_2}}\right], \tag{6.30}$$

with $Q^2 = 2\pi/3\sqrt{3}Ma^2$. We take the + sign for the sublattice $l = C, D$ and the − sign for $l = A, B$. We see that the matrix elements of the confining potential are products of two contributions: (i) from the confining electrostatic potential and (ii) from the bulk wavefunctions which contains information about the Berry's curvature. We now solve equation (6.18) to obtain our QD spectrum and wavefunctions. If we were to retain only the electrostatic confining potential we would have obtained the spectrum of a two-dimensional harmonic oscillator as in the usual semiconductor quantum dots. However, the contribution from wavefunctions and Berry's phases alters significantly the energy spectrum as shown in Fig. 6.2.

Figure 6.2 shows the QD energy spectrum for the QD radius $R_{QD} = 20$ nm for valley $\vec{K}$ near the Fermi level set at zero. We see that the confinement of electrons and holes results in the reduction of the single-particle energy gap, 380 meV in the bulk, to ~ 40 meV. We find the QD energy spectrum to be very different from that found in gated lateral QD in GaAs or self-assembled QDs, which are understood in terms of electronic shells of a two-dimensional harmonic oscillator [192, 193]. The insets in Fig. 6.2 show the electronic wavefunctions on layer 1 (top) and layer 2 (bottom) for states at the top of the valence band and at the bottom of the conduction band. We see that the lowest of the conduction-band states is s-like, followed by two levels of a p shell which is split in energy. However, the next group of levels cannot be understood in terms of the three levels of a d shell. Hence, the single-particle spectrum here is different from self-assembled and gated QDs as pointed out by Peeters and co-workers [38].

Now we can also write our QD wavefunctions by rewriting equation (6.15) as a linear combination of atomic p_z orbitals

$$|\varphi^s\rangle = \sum_{\vec{R},l} C^s_{\vec{R},l} \, |\psi_{\vec{R},l}\rangle \,, \tag{6.31}$$

with coefficients $C^s_{\vec{R},l} = \frac{1}{\sqrt{M}} \sum_{\vec{k},p} B^s_{p,\vec{k}} A^p_{\vec{k},l} e^{i\vec{k}\cdot(\vec{R}+\vec{d}_l)}$.

6.3 Bethe-Salpeter equation

We start our many-body analysis by approximating the many-electron ground state as a single Slater determinant $|GS\rangle = \prod_{p,\sigma} c^{\dagger}_{p\sigma} |0\rangle$ of all occupied valley and spin QD valence band states shown in Fig. 6.2. Here, $c^{\dagger}_{p\sigma}$ creates an electron with spin σ in a p state of the valence band. Next, we write the exciton states $|\psi^{\mu}\rangle$ as a linear combination of one electron-hole pair excitations conserving S_z as

$$|\psi^{\mu}\rangle = \sum_{p,q,\sigma} A^{\mu}_{p,q,\sigma} c^{\dagger}_{q\sigma} c_{p\sigma} |GS\rangle \,. \tag{6.32}$$

Here, $A^{\mu}_{p,q,\sigma}$ is the amplitude corresponding to the electron-hole pair excitation involving states p and q. Here, $c_{p\sigma}$ removes an electron with spin σ from the occupied state p in the valence band leaving behind a hole, and $c^{\dagger}_{q\sigma}$ places this electron in the empty conduction band state q. The index p runs over all VB states in the QD and the index q goes through all unoccupied states of the QD.

The many-electron Hamiltonian in the basis of QD single-particle states can be written as

$$\begin{aligned} \hat{H}_{MB} = & \sum_{p,\sigma} E_p c^{\dagger}_{p,\sigma} c_{p,\sigma} \\ & + \frac{1}{2} \sum_{pqrs} \sum_{\sigma\sigma'} \langle pq|V_C|rs\rangle c^{\dagger}_{p\sigma} c^{\dagger}_{q,\sigma'} c_{r,\sigma'} c_{s,\sigma} \\ & - \sum_{p,s,\sigma} V^{P}_{ps} c^{\dagger}_{p\sigma} c_{s,\sigma}. \end{aligned} \tag{6.33}$$

The indices in sums run over all QD states (those in the valence and conduction bands). Further, the potential $V_C = \frac{e^2}{\kappa|\vec{r_1} - \vec{r_2}|}$ accounts for electron-electron Coulomb interactions screened by the dielectric constant κ. In what follows we will use the value of $\kappa = 6$ (Ref. [1]). In the third term of equation (6.33) we account for a positive charge background with the same charge distribution as that of the electrons in the filled valence band. The positive background ensures the overall charge neutrality and cancels out the direct interaction among electrons in the valence band.

The Coulomb matrix elements $\langle pq|V_C|rs\rangle$ are expressed atomistically as

$$\langle p,q|V_C|r,s\rangle = \sum_{i,j,k,l} \left(C_i^p\right)^* \left(C_j^q\right)^* C_k^r C_l^s \langle i,j|V_C|k,l\rangle, \tag{6.34}$$

where $\langle i,j|V_C|k,l\rangle$ are Coulomb matrix elements computed numerically with Slater-like p_z orbitals localized on atoms i, j, k, l [1]. The sum above runs over atomic sites and is difficult to compute for a system of millions of atoms (1.6 million in this example). For computational details, see Ref. [110] and section 2.5.2 on discussion of the calculation of Coulomb matrix elements.

We now move on to obtaining the exciton states $|\psi^\mu\rangle$. The amplitudes $A^\mu_{p,q,\sigma}$ corresponding to the electron-hole pair excitations composing these states satisfy the Bethe-Salpeter equation (BSE):

$$\begin{aligned} &\sum_{q',p',\sigma'} [(E_{q',\sigma'} + \Sigma_{q',\sigma'}) - (E_{p',\sigma'} + \Sigma_{p',\sigma'})]\delta_{p,p'}\delta_{q,q'}\delta_{\sigma,\sigma'} A^\mu_{p',q',\sigma'} \\ &+ \sum_{q',p',\sigma'} [\langle p,q'|V_C|p',q\rangle - \langle p,q'|V_C|q,p'\rangle\, \delta_{\sigma\sigma'}] A^\mu_{p',q',\sigma'} = E_\mu A^\mu_{p,q,\sigma}. \end{aligned} \tag{6.35}$$

Here, the electron-hole pair energy is renormalized by the self-energy, which in the screened Hartree-Fock approximation is given by $\Sigma_{p,\sigma} = -\sum_{q,\sigma'} \delta_{\sigma,\sigma'} \langle q,p|V_C|q,p\rangle$, where the sum over q runs over the valence band states. In this example of a QD, we find self-energies at the top of the valence band and at the bottom of the conduction band to converge with 120 filled valence band QD states. The scattering of electron-hole pairs (the vertex correction) is controlled by an attractive (negative) direct term and a repulsive (positive) exchange term. We note that the BSE for a QD contains all possible electron-hole pairs, accounting for the mixing of the relative and center of mass motion.

To compute the excitonic states we solve the BSE given above. We start our analysis by computing the spectrum of non-interacting electron-hole pairs, i.e., $V_C \equiv 0$, shown in Fig. 6.3(a). We find degenerate shells of electron-hole levels, forming either eight-fold or sixteen-fold degenerate manifolds. The eight-fold degeneracy can

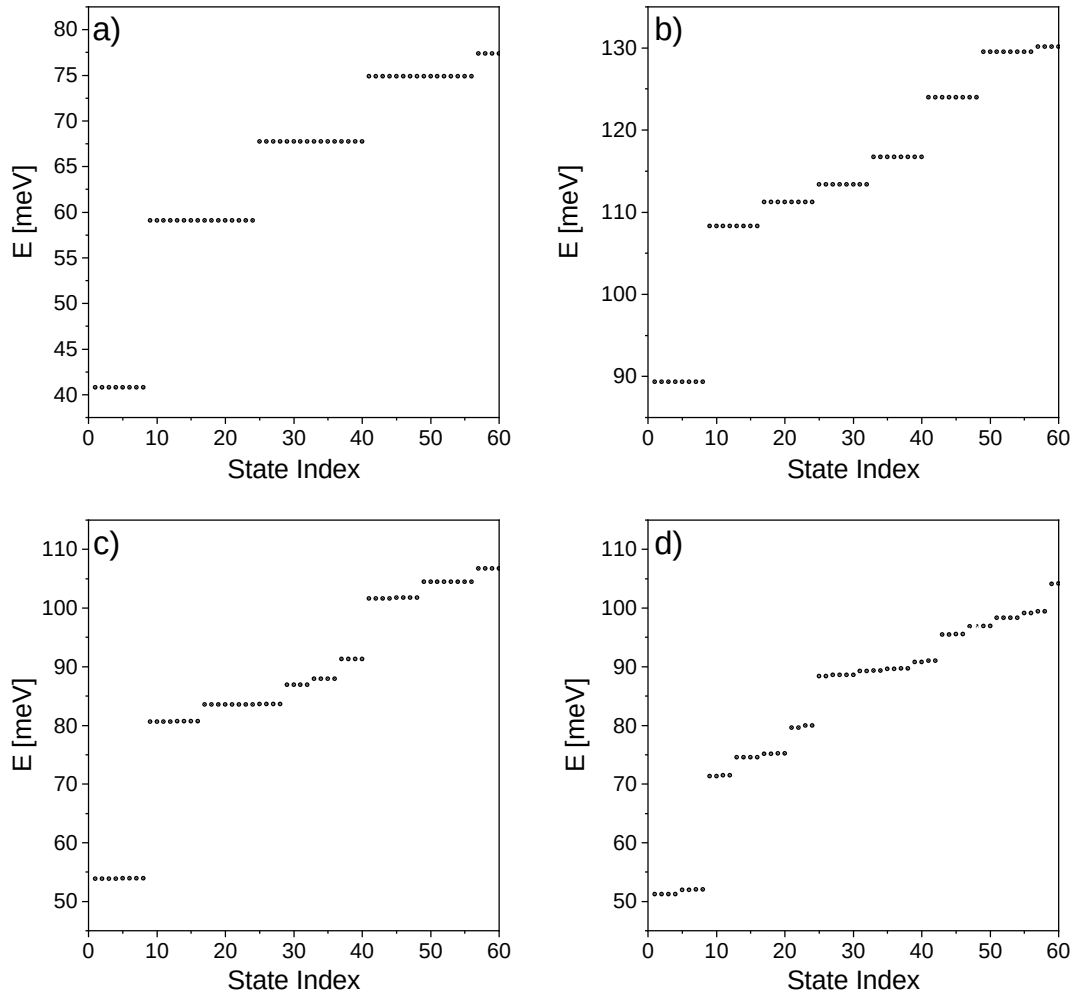

Figure 6.3: (a) Energies of noninteracting electron-hole pairs. (b) Energy spectrum of the pairs renormalized by self-energies. (c) Energy spectrum of the pairs accounting for the self-energies and vertex corrections (the electron-hole attraction) but without correlations. (d) Excitonic energy diagram accounting for all aspects of the electron-electron interaction.

be understood by constructing all electron-hole pairs that have the energy of the single-particle energy gap and conserve total S_z. This corresponds to removing an electron from state number 8 and placing it on state number 9 in Fig. 6.3(a). Both states 8 and 9 have spin and valley degeneracy. There will be two electron-hole pairs in each valley (total of four, including spin) and four more between valleys. Thus we have eight possible electron-hole pairs with the energy of the single-particle gap. To understand the sixteen-fold manifold, let us consider the second lowest-energy electron-hole pairs. These pairs are constructed by exciting electrons from state 8 to state 10 and from state 7 to state 9 in Fig. 6.2(a). The two possibilities arising from

the electron-hole symmetry double the resulting degeneracy to sixteen.

Next, we turn on the self-energy contribution to the electron-hole pair energies. The resulting spectrum is shown in Fig. 6.3(b). The self-energies result in a large blueshift of the electron-hole pair energies. Furthermore, the self-energies split the sixteen-fold degenerate manifolds into two subclasses because the values of the self-energy in the excitations involving states 8 and 10 are different than those involving states 7 and 9.

We next calculate the energies of electron-hole pairs including self-energies and vertex corrections, i.e. the electron-hole attraction. These spectra are shown in Fig. 6.3(c). Direct electron-hole attraction is large and lowers the energy of the electron-hole complex, while the electron-hole exchange interaction is repulsive and raises the energy of the complex slightly. While the direct electron-hole interaction does not discriminate valleys, the exchange interaction is different within a valley and between valleys. This separates the energy of intervalley and intravalley electron-hole pairs. Indeed, the intervalley electron-hole pair has a lower energy due to its smaller repulsive exchange interaction. We also observe reordering of higher-energy electron-hole pairs due to large exchange values compared to the single-particle level spacing.

Finally, we include the Coulomb scattering connecting electron-hole pairs and solve the full BSE. The resulting excitonic spectrum is shown in Fig. 6.3(d). The excitonic states can be categorized as inter/intra-valley singlets/triplets. The intervalley excitons are at lower energies than their intravalley counterparts because the repulsive exchange interaction for intravalley excitons is stronger. Furthermore, each class of intravalley and intervalley excitons is further split into spin singlet and triplets. Triplets are at lower energies than their singlet counterparts as the exchange now favours the triplets in energy. Focusing on the ground state, we see that it is approximately four-fold degenerate and corresponds to intervalley excitons formed from electron-hole pairs across the gap. The singlet-triplet splitting for these states is negligible and is the reason why it appears four-fold rather than two-fold degenerate.

6.4 Optical absorption

The exciton states are created by absorbing photons with energy ω. Starting with the Fermi's golden rule, and the ground state $|GS\rangle$ as the fully occupied valence band, the absorption spectrum is given by [139]:

$$A(\omega) = \sum_{\mu} \left| \sum_{s,s',\sigma} \mathcal{E}_0^{\pm} \cdot \vec{D}_{s,s'} \left(A^{\mu}_{s,s',\sigma} \right)^* \right|^2 \delta\left(E_{\mu} - \omega \right). \tag{6.36}$$

Here $\mathcal{E}_0^{\pm}$ is the polarization vector for our circularly polarized electric field and $\vec{D}_{s,s'}$ are dipole matrix elements given by

$$\vec{D}_{s,s'} = \langle s | \vec{r} | s' \rangle = \sum_{i,j} (C_i^s)^* C_j^{s'} \langle i | \vec{r} | j \rangle . \tag{6.37}$$

The dipole matrix elements connecting real-space orbitals are given by

$$\langle i | \vec{r} | j \rangle = D_{ij} \left(\hat{R}_j - \hat{R}_i \right) + \vec{R}_j \delta_{ij}, \tag{6.38}$$

where $D_{ij} = \left| \int d\vec{r} \phi^*_{p_z} \left(\vec{r} - \vec{R}_i \right) \vec{r} \phi_{p_z} \left(\vec{r} - \vec{R}_j \right) \right|$ and $\phi_{p_z} \left(\vec{r} - \vec{R}_j \right)$ is the Slater p_z orbital with Slater parameter $\xi = 3.25$. If the atoms i and j are nearest neighbors, we find $D_{ij} = 0.313763\ a_b$, while if they are next nearest neighbors, $D_{ij} = 0.0711159\ a_b$, where a_b is the Bohr radius.

Figure 6.4 shows the effect of the wavefunctions on dipole matrix elements controlling the coupling of the QD with light. The arrows in Fig. 6.4(a) show which states in the valence band are connected with which states in the conduction band by finite dipole matrix elements. We see that, unlike in self-assembled quantum dots, the state at the top of the valence band (number 8) is not connected with the lowest-energy state (number 9) in the conduction band, but with the third excited state (number 11). By symmetry, the state at bottom of the conduction band (number 9) is connected with the valence band state number 6. The second-highest in energy valence band state (number 7) is now connected with the highly excited conduction band

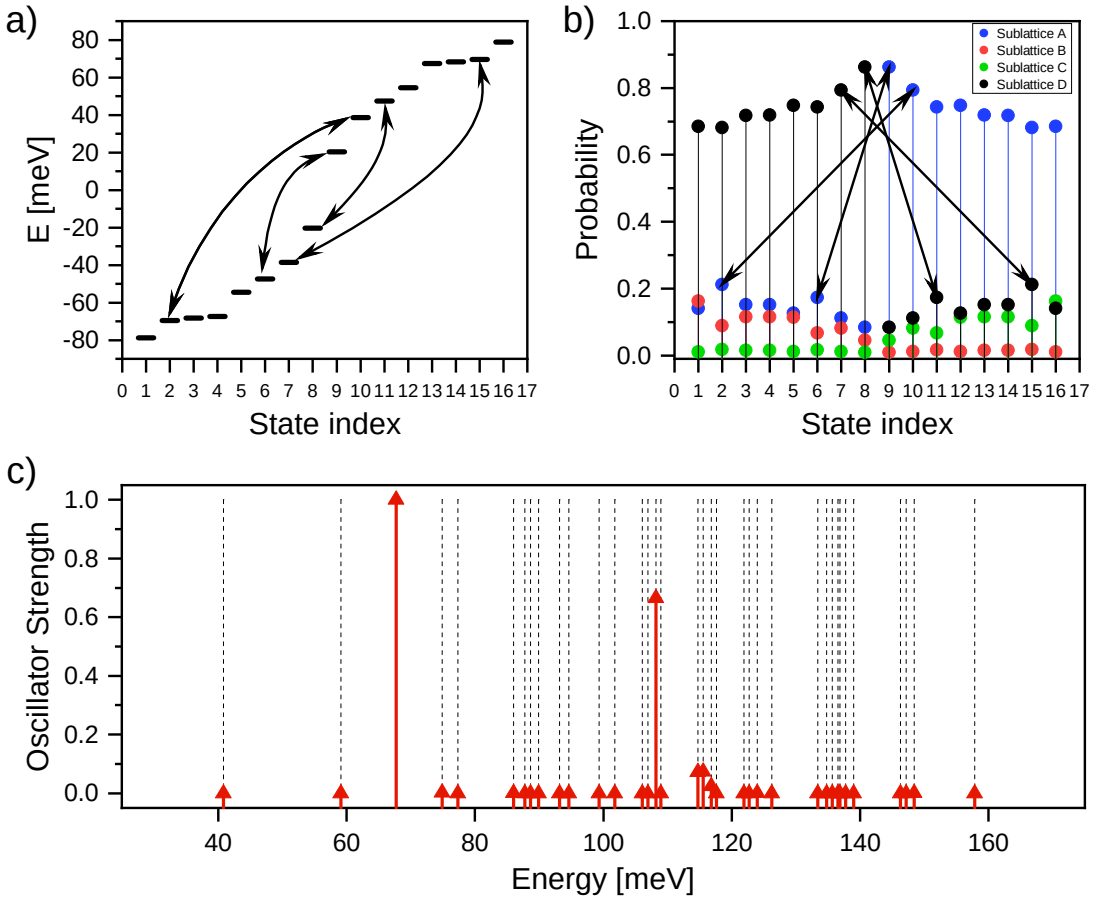

Figure 6.4: (a) Optically active transitions indicated by arrows connecting single-particle state energy levels in the $-\vec{K}$ valley of the gated bilayer graphene QD. (b) sublattice occupation by the wavefunction. Sublattice A,B correspond to layer 1, while sublattice C,D corresponds to layer 2. The dark black lines pointing to states show the transitions with finite dipole matrix element. (c) red peaks - square of dipole matrix elements for one valley as a function of energy. The dashed lines mark the energy of all electron-hole pairs constructed within one valley.

state number 15. Figure 6.4(b) shows how the probability density corresponding to different states is distributed over sublattices. In particular, we see that the large dipole elements correspond to the two QD states residing largely on the same sublattice. For example, state number 11 and state number 8 both occupy the sublattice B. As we shall show, this complicated light-matter coupling is further significantly modified by electron-electron interactions.

Figure 6.5 shows the absorption spectrum as a function of the photon energy for our model QD. The vertical black lines correspond to energies E_μ of excitonic states, while the red line corresponds to excitonic states contributing to absorption. In

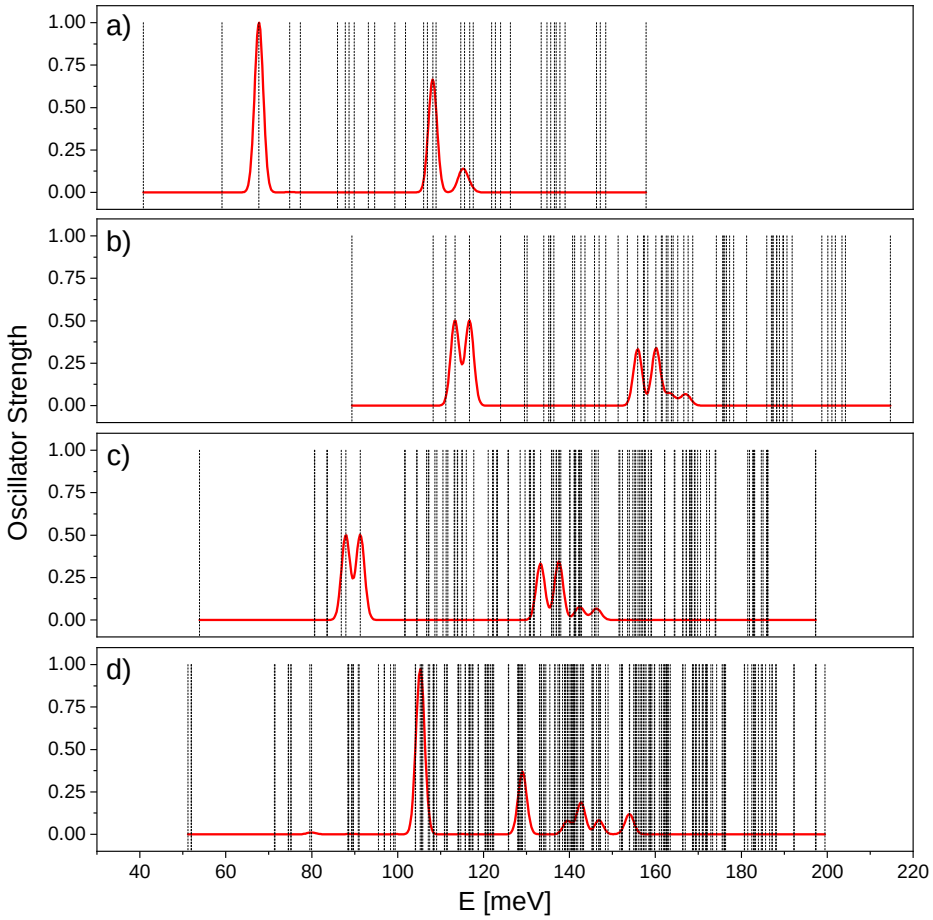

Figure 6.5: Absorption Spectrum as a function of photon energy ω for the gated bilayer graphene quantum dots. (a) no interactions , (b) including self energies, (c) including self-energies and electron-hole attraction. (d) corresponds to the full BSE.

Fig. 6.5(a) we show the absorption spectrum ignoring interactions. We find the low-energy electron-hole pairs to be dark. This is a consequence of the previously discussed zero dipole matrix elements for the two lowest-energy electron-hole complexes. The third dashed line corresponds to the first bright peak at around 67 meV. This is the energy of electron-hole pair with a large dipole matrix element, i.e., the sixteen-fold degenerate third manifold shown in Fig. 6.3(a). A second smaller peak is seen in Fig. 6.5(a) at around 108 meV. This maximum corresponds to the second bright dipole matrix element shown in Fig. 6.4(c).

We now turn on the effects of self-energies shown in Fig. 6.5(b). As already discussed, self-energies split the sixteen-fold manifold into two sub-manifolds, and thus the single large peak has split into two. The peaks have also shifted to higher

energies due to the blueshift introduced by the self-energies.

The inclusion of the electron-hole attraction causes a redshift shown in Fig. 6.5(c), bringing the absorption maxima closer in energy to the non-interacting peaks. The vertex correction has also broken the degeneracy of intravalley and intervalley electron-hole pairs. Reordering of levels occurs due to the electron-hole exchange and new dark states emerge at an energy lower than that of the bright state.

Finally, when the scattering terms are accounted for in the full BSE, the degenerate states split into triplets and singlets, with triplets being dark, as shown in Fig. 6.5(d). The lowest exciton energy decreased to 50 meV due to correlations, but the bright exciton peak has moved to higher energy due to the singlet-triplet splitting. Many new dark states emerge at low energies since the dark triplets have shifted down in energy. More level reordering occured due to the singlet triplet splitting as well as correlations. The bright peak is now blueshifted to 110 meV, i.e., $\sim$ 30 Thz. There is a second smaller peak at 130 meV which corresponds to the second optically active transition. This transition is smeared out in the interacting system since correlations spread the relevant optically active electron-hole pairs amongst many exciton states. The many dark low-energy excitonic states are either intervalley excitons, spin triplets, or have vanishing dipole matrix elements. The presence of many low-energy dark states makes these BLG QDs potential candidates for storage of photons.

6.5 Conclusion

In summary, we developed a theory of excitons confined in laterally gated bilayer graphene quantum dots. These nanostructures combine the ability to confine electrons and holes of semiconductor self-assembled quantum dots with the tunability of laterally gated semiconductor quantum dots, with the latter confining only either electrons or holes. Here we describe such a strongly interacting electron-hole complex forming an electrically tunable exciton. We find these excitons to be very different from excitons found in semiconductor quantum dots and nanocrystals. Indeed, the exciton energy as well as the absorption and emission spectrum is tunable by voltage

from the THz to FIR range. The conservation of spin, valley, and orbital angular momentum results in a band of dark low-energy states making this system a promising candidate for storage, detection and emission of photons in the Terahertz range.

Chapter 7

N Electron Ground State of Gated Bilayer Graphene Quantum Dot

This chapter is based on a draft of a paper we are preparing to submit. This has been modified and edited to fit the context of the thesis as it builds off of the previous chapter. This work was done in close collaboration with the other authors, and I have reproduced the results for $N = 2$ electrons and have all the numerical tools in place to reproduce all the results.

In this chapter, we expand our knowledge on gated bilayer graphene quantum dots using the methodology described in chapter 6. In the previous chapter, we studied both the VB and CB, but focused on only excitons. In this chapter we focus on only the CB and study the N electron ground state as a function of interaction strength. We perform calculations for $N = 2 - 6$ electrons as a function of the interaction strength $\kappa = 1$ (strongest interactions) to $\kappa = 15$ (weakest interactions). In the following, we will illustrate the results in detail for $N = 2$ and $N = 4$. We note that the problem of interacting massive Dirac Fermions remains challenging and until now, was studied for only two interacting particles. Here we present results up to N=6 massive Dirac Fermions.

We predict the existence of spontaneous spin and valley symmetry broken states of interacting massive Dirac Fermions in a bilayer graphene gated quantum dot based on

exact diagonalization of the many-body Hamiltonian. Atomistic tight-binding model is used to compute the energies and wavefunctions of the single-particle states confined in the dot created by vertical electric field and lateral metallic gates. Electron-electron interaction Coulomb matrix elements are obtained for a set of several lowest-energy electronic orbitals and screened by the dielectric constant of the surrounding medium. The effect of the Coulomb interaction is measured by the ratio of Coulomb matrix element $\langle 11|V|11\rangle$, to the single-particle level spacing. As we increase the strength of interactions relative to the single-particle level spacing, we find the electrons in a series of spin and valley symmetry-broken phases with increasing valley and spin polarization. The phase transitions result from the competition of the single-particle, exchange, and correlation energy scales. A phase diagram for N = 2-6 massive Dirac Fermions filling up the two lowest energy shells is mapped out as a function of the strength of Coulomb interactions.

7.1 N-electron many-body complexes

We begin by considering the SP QD states computed in the previous chapter, now shown in Figures 7.1. These states are now labelled in increasing order starting from the bottom of the CB. In (a) and (b) we show the positive eigenenergies of the gated BLG QD in two cases: without and with the trigonal warping (γ_3 described in section 2.1.2), respectively. We find that in either case the states form valley doublets, producing quadruply degenerate manifolds (shells) including spin. However, we do not identify any quasi-degenerate orbital shells. This is in contrast with recent experimental studies [194, 195], where shells of excited states with degeneracy of 12 (2 spin $\times$2 valley $\times$3 trigonal warping effect) were detected in addition spectra. We attribute the absence of this high-order degeneracy to the small size of our quantum dot. In consequence, as the electron energy spectra with and without trigonal warping are qualitatively the same, henceforth we assume $\gamma_3 = 0$. We distribute N electrons on the single-particle quantum dot SP states shown in Fig. 7.1(a). The Hamiltonian

of this interacting system is

$$\hat{H}_{MB} = \sum_{p,\sigma} E_p c^+_{p,\sigma} c_{p,\sigma} + \frac{1}{2\kappa} \sum_{pqrs} \sum_{\sigma\sigma'} \langle p, q|V_C|r, s\rangle c^+_{p\sigma} c^+_{q,\sigma'} c_{r,\sigma'} c_{s,\sigma}. \tag{7.1}$$

The index $p = \{\alpha, \xi\}$ enumerates the single-particle states with level α in valley ξ,

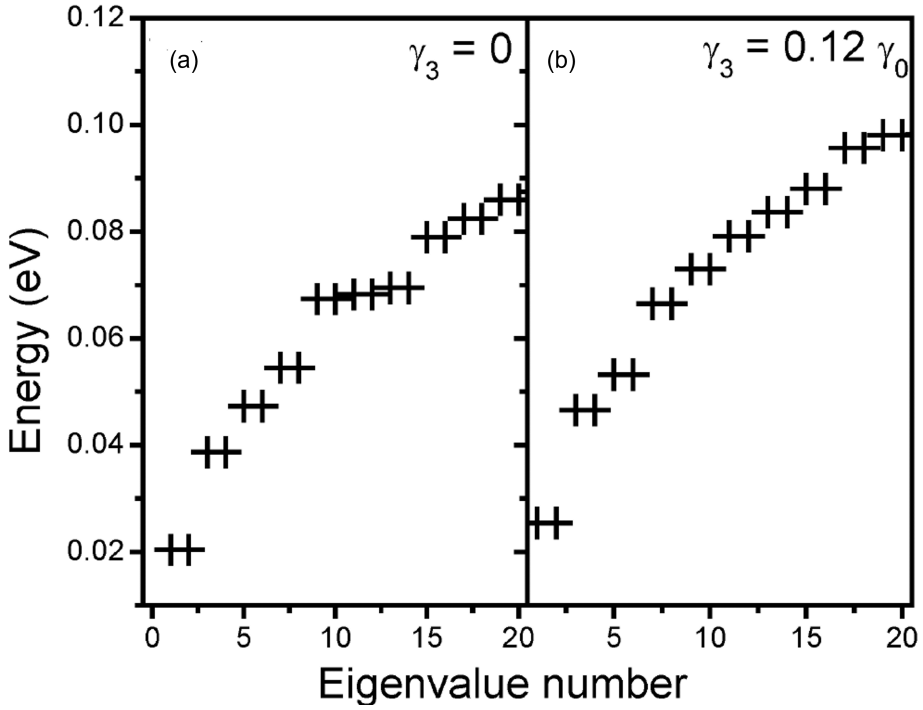

Figure 7.1: The electronic single-particle energies in the gated quantum dot without (a) and with (b) trigonal warping.

while $\sigma = \pm\frac{1}{2}$ is the electron spin. The dielectric constant κ is introduced to tune the strength of the Coulomb interactions relative to the single-particle quantization defined by the energy spacing $\Delta = E_3 - E_1$ in valley K. The small parameter controlling the importance of interactions is given by $\langle 1, 1|V|1, 1\rangle/(\kappa\Delta)$. This parameter is controlled by dielectric constant, with $\kappa \to \infty$ characterizing the system of non-interacting electrons. Lastly, V_C denotes the electron-electron interaction potential, which in this work is taken to be of the Coulomb form $V_C(\vec{r}_1, \vec{r}_2) = e^2/4\pi\epsilon_0|\vec{r}_1 - \vec{r}_2|$, with e being the electron charge, and ϵ_0 being the vacuum dielectric permittivity.

To complete the Hamiltonian (7.1), we now turn to calculating the Coulomb matrix elements $\langle p, q|V_C|r, s\rangle$. We utilize the real-space form (6.31) of the single-particle states and compute the elements defined in 6.34. In our system, $N_A \sim 1.6 \cdot 10^6$

atoms, and calculation of the above quadruple sum presents an unmanageable computational complexity of $O(N_A^4) = O(10^{24})$. We simplify the integral by including the direct-type Coulomb elements only, i.e., we set $l = i$ and $k = j$, which decreases the computational complexity to $O(10^{12})$. The Coulomb elements are generally taken as $\langle i, j|V_C|j, i\rangle = e^2/4\pi\epsilon_0|\vec{R}_i - \vec{R}_j|$. However, we consider the following special cases: if

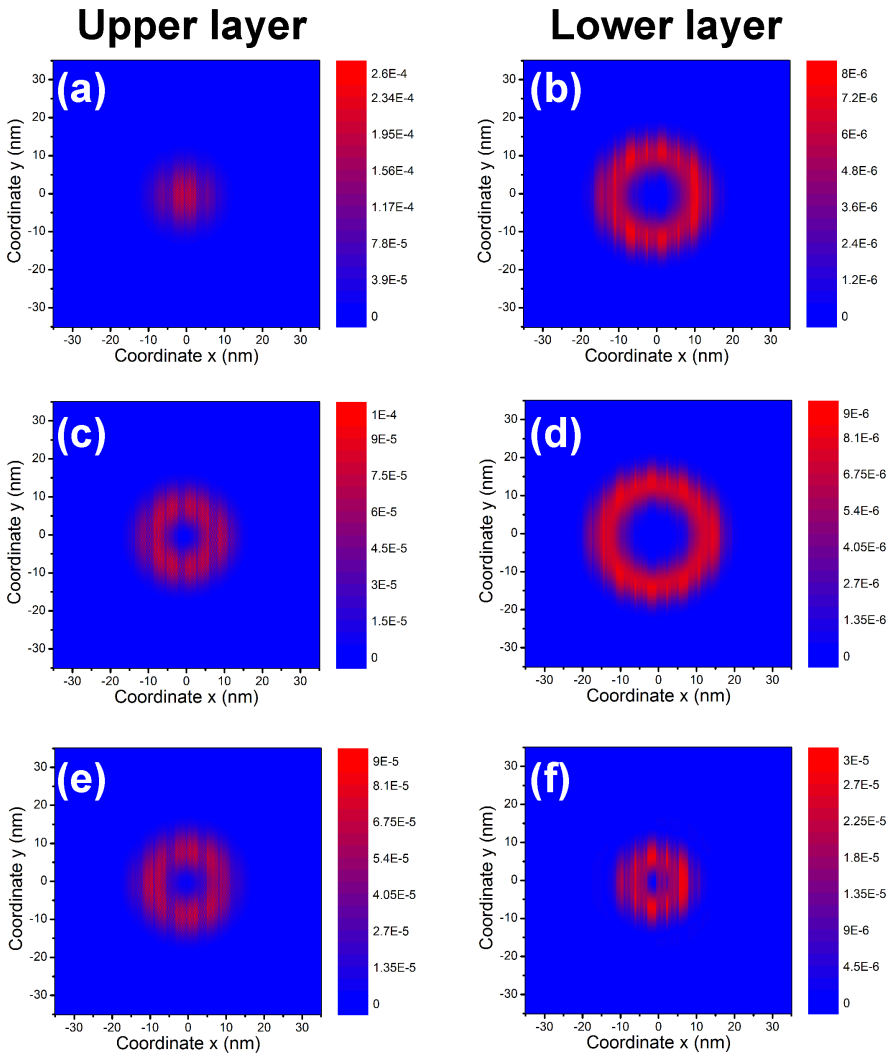

Figure 7.2: Probability densities of the confined single-particle states from the three lowest valley doublets. Panels (a), (c), and (e) show the probability densities of states 1, 3, and 5, respectively on the upper layer, while panels (b), (d), and (f) show the densities on the lower layer.

atoms i and j are identical, or are first, second, or third neighbors within the same layer, we set the values to 17.307 eV, 8.942 eV, 5.582 eV, and 4.856 eV, respectively. If atoms i and j belong to different layers, we set the element values to 4.562 eV and 4.103 eV for the relative nearest and second neighbors, respectively. These values are

obtained by direct numerical integration of the Coulomb potential with appropriately positioned p_z orbitals approximated by the Slater functional form [1] as described in section 2.5.2. We note that it is possible to obtain nonzero values of the orbitally-resolved Coulomb elements if the atoms i, j, k, l form more nontrivial configurations where indices are within NNs of each other (giving three-center or even four-center integrals). These elements are shown in table. 2.1. However, we found that the inclusion of such terms greatly increases the computational burden while contributing to the overall values of the Coulomb elements to a negligible degree.

In Table 7.1 we list selected Coulomb matrix elements computed for the single-particle orbitals corresponding to the spectrum presented in Fig. 7.1(a).

The upper part of the table shows the direct elements, while the lower part shows the exchange elements. One of the orbitals is always chosen to be 1, i.e., the lowest-energy state in the valley K. We find, in general, that the direct Coulomb elements are of order of 0.2 eV, i.e., their magnitude is larger than the splitting of single-particle levels for our dot. We find also that the values of intra-valley (involving an odd index) and inter-valley direct elements (involving an even index) are the same within the same valley manifolds. This is understandable as the direct Coulomb terms depend on the charge density, which is identical for each component of the valley doublet. On the other hand, the exchange elements discriminate between the valleys very strongly: the intra-valley exchange elements are typically two orders of magnitude larger than the inter-valley elements. Lastly, we comment on the apparent irregularity in the values of the direct elements involving the valley doublet of states 5 and 6. We find that these elements are larger than those involving the lower-energy valley doublet (states 3 and 4). That difference is not manifested in the exchange, however. Typically, one sees a systematic decrease of the magnitude of all Coulomb elements with the increase in the difference between indices. The breaking of that trend can be understood based on our discussion of the probability densities presented in Fig. 7.2. The probability of the first excited shell (state 3 and 4), shown in panels (c) and (d), is indeed different (more spread spatially) than that of the state 1, shown

Element	Value (meV)
$\langle 1,1\|V_C\|1,1\rangle$	217.94
$\langle 1,2\|V_C\|2,1\rangle$	217.94
$\langle 1,3\|V_C\|3,1\rangle$	168.22
$\langle 1,4\|V_C\|4,1\rangle$	168.22
$\langle 1,5\|V_C\|5,1\rangle$	180.15
$\langle 1,6\|V_C\|6,1\rangle$	180.15
$\langle 1,2\|V_C\|1,2\rangle$	1.02
$\langle 1,3\|V_C\|1,3\rangle$	55.70
$\langle 1,4\|V_C\|1,4\rangle$	0.49
$\langle 1,5\|V_C\|1,5\rangle$	26.58
$\langle 1,6\|V_C\|1,6\rangle$	0.42

Table 7.1: Selected Coulomb matrix elements connecting single-particle states in the quantum dot. Indices follow Fig. 7.1(a).

in panels (a) and (b). However, the probability density of the second excited shell (state 5), shown in panels (e) and (f), is again more compact, resulting in a stronger Coulomb repulsion with the ground state. The effect is only seen in the direct term, and not in the exchange, because the latter has a much more short-distance character than the former, and the compact component of the state 5 is observed on the lower layer of the system, while the ground state is more confined to the upper layer.

Having fully parametrized the Hamiltonian (7.1), we now describe the procedure of computing the eigenenergies and eigenstates of N interacting electrons confined in our dot. We utilize the configuration-interaction approach, in which we generate all possible configurations of N electrons by distributing them on N_{SP} single-particle orbitals. We compute the matrix of the Hamiltonian $\hat{H}_{MB}$ in the basis of configurations, and we diagonalize this matrix numerically. We take $N_{SP} = 16$ single-particle states (i.e., 8 valley doublets, not including spin) and N from 2 to 6. We note that $\hat{H}_{MB}$ commutes with $\hat{S}_z$, which allows us to divide the Hilbert spaces for each N into subspaces labeled by the spin polarization. Whenever possible, we diagonalize the resulting Hamiltonian using full-matrix diagonalization methods to gain access to all many-body electronic states. However, for larger electron numbers the Hilbert space sizes are of order of 10^5, and we use iterative diagonalization methods to obtain the ground and a few low-energy excited electronic states in each spin subspace.

7.2 $N = 2$ interacting electrons in the dot - half-filled lowest energy shell

Here we focus on $N = 2$ interacting electrons corresponding to a half-filled lowest energy shell. In the two-electron case we construct two Hilbert subspaces: $S_z = -1$ (holding the polarized spin triplets) and $S_z = 0$ (holding the spin singlets and unpolarized spin triplets). We perform full matrix diagonalization in each subspace as a function of the interaction parameter κ. The energies of the two-electron eigenstates are plotted in Fig. 7.3 as black (singlets) and red (triplets) bars. For each κ, we measure the energy from that of the ground state. We find that for all values of κ except $\kappa = 1$ the spin triplet is the ground state. As the effective value of κ for realistic graphene systems is expected to be larger than 1, this result is consistent with the calculations of Ref. [39,64] and the measurements of Refs. [64,196,197] in the limit of zero magnetic field. Furthermore, these prior studies indicate that the ground state is valley-unpolarized, and name it the "valley singlet, spin triplet" state $|S_v\rangle|T_s\rangle$. We confirm this by calculating the orbital-, valley-, and spin-resolved charge density $\langle GS|c^+_{\alpha,\xi,\sigma}c_{\alpha,\xi,\sigma}|GS\rangle$, where $|GS\rangle$ is the correlated ground state obtained numerically as the eigenstate of our Hamiltonian $\hat{H}_{MB}$. We find the valley-unpolarized ground state for the interaction parameter $\kappa > 3$ (i.e., sufficiently weak interactions). In Fig. 7.4(c) we plot this charge density on the ladder of the single-particle states for $\kappa = 4$. We find that this picture does not change appreciably as we increase κ.

On the other hand, for stronger interactions, $\kappa = 2$ and 3, we find that the ground state is a valley polarized triplet. We plot the ground state charge density for $\kappa = 2$ in Fig. 7.4(b), from which we see that both electrons are found in the valley K. The ground state with $S_z = -1$ is in fact doubly degenerate, and the charge density for its counterpart reveals both electrons in the valley $K' = -K$. A similar doubly-degenerate manifold corresponds to the unpolarized triplet with $S_z = 0$, and the polarized triplet with $S_z = 1$, giving altogether a six-fold degenerate state at zero magnetic field. This is in contrast with only a three-fold degeneracy of the valley-

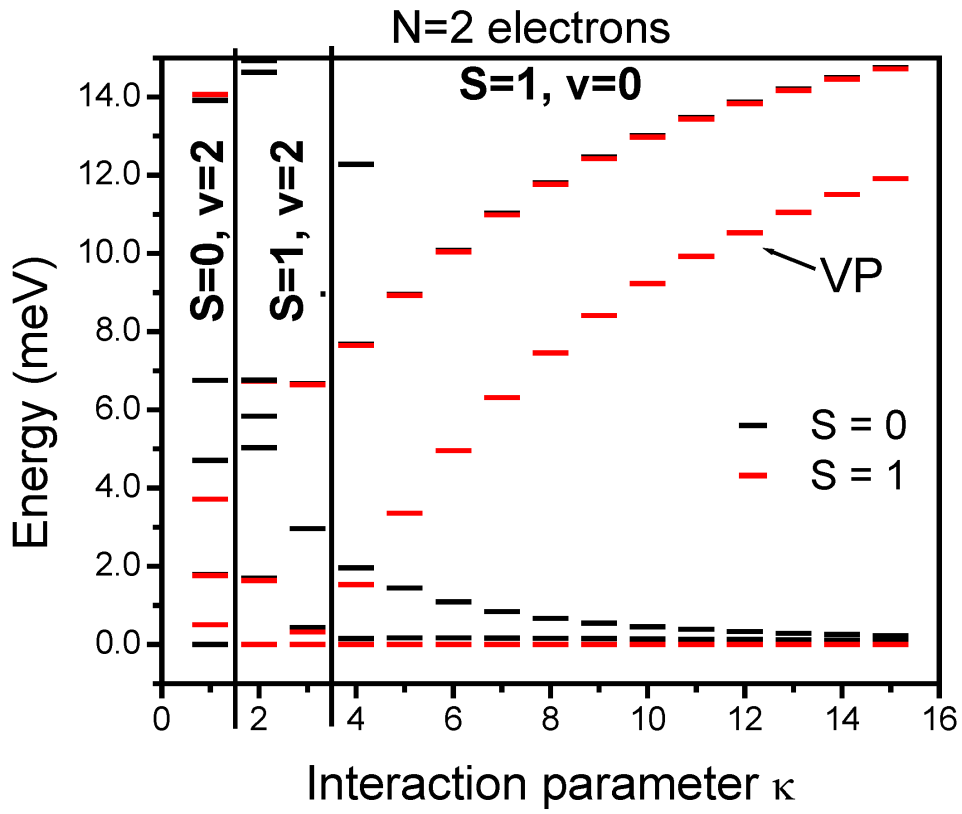

Figure 7.3: Energies of the low-energy eigenstates of the two-electron dot as a function of the interaction parameter κ. Black (red) bars correspond to the spin singlet (triplet). For each value of κ, the energies are measured from the ground state triplet level. VP corresponds to the valley-polarized triplet, and v corresponds to valley polarization.

singlet spin triplet, appearing as the ground state for weaker interactions. Finally, for the strongest interactions, $\kappa = 1$, we deal with a valley-polarized singlet, whose charge density is shown in Fig. 7.4(a). Here, both electrons are found in the valley K. We also find another singlet state, degenerate in energy with this one, with both electrons in the valley K'.

In the phase transition from the valley-unpolarized to the valley- polarized triplet, the breaking of the valley symmetry in the ground state is a clear consequence of the competition of the intra-valley exchange interaction and the single-particle energy quantization. For very weak interactions, the electronic occupation of levels is mostly determined by the single-particle energies. The valley-unpolarized triplet configuration has a lower single-particle energy than the valley-polarized one because it involves only the states from the lowest valley doublet. Owing to the Pauli exclusion princi-

ple, constructing a valley-polarized triplet requires positioning the two electrons in two different valley doublets, which costs the single-particle energy. As the interactions become stronger (κ decreases), the intra-valley exchange interaction increases in magnitude. This interaction term decreases the total energy of the two electrons, and therefore favours the valley-polarized triplet. The energy of the valley-unpolarized triplet is not renormalized in this fashion, since the inter-valley exchange is much smaller in magnitude. Eventually, the gain in the exchange energy outweighs the excess in the single-particle energy, and the valley-polarized triplet becomes the ground state. This trend can be seen in the energy diagram, Fig. 7.3 by identifying the valley-polarized triplet as the excited triplet state (labeled VP). This state descends in energy as the interactions are made stronger (κ decreases, from right to left) and changes places with the valley-unpolarized state for $3 < \kappa < 4$. As κ is further tuned from 3 to 2, the gap between the ground and first excited triplet begins to increase.

The second phase transition, from the valley-polarized triplet at $\kappa = 2$ to the valley-polarized singlet at $\kappa = 1$, appears to be driven by electronic correlations. We find that it is energetically favourable to spread the electron density among several single-particle orbitals to minimize their repulsion, even at a cost of the loss of the exchange energy. The charge density shown in Fig. 7.4(a) can only result from a correlated two-electron state, i.e., one that cannot be represented by one Slater determinant, but is a superposition of many configurations. We note that the charge density on the orbitals 5 and 6 is negligible, which is due to the large Coulomb matrix elements involving these orbitals, as discussed in the previous Section.

7.3 $N = 4$ interacting electrons - filled lowest energy shell

Next, we focus on the case of $N = 4$ electrons which corresponds to a filled lowest energy shell. From the structure of single-particle states shown in Fig. 6.2(a) we expect that, with sufficiently weak interactions, the $N = 4$ electrons will completely

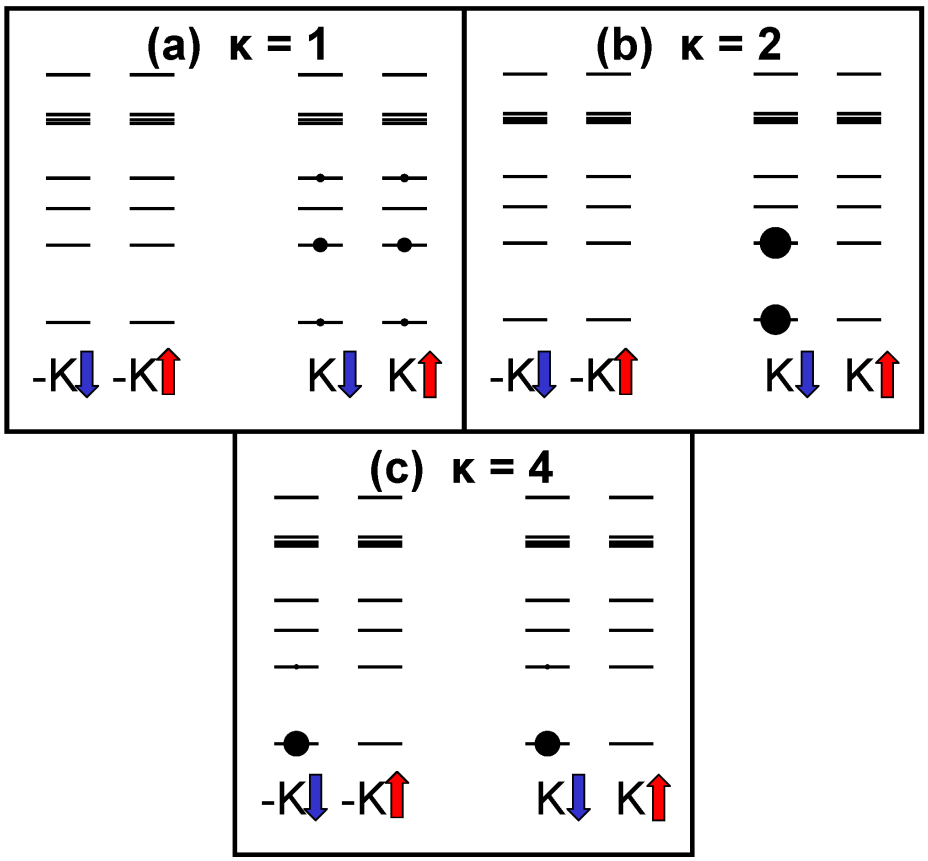

Figure 7.4: Charge density of the two-electron ground state on the single-particle orbitals for $\kappa = 1$ (a), $\kappa = 2$ (b), and $\kappa = 3$ (c). We resolve the orbitals from valley $K' = -K$ (left double ladder) and K (right double ladder), as well as spin down (left) and up (right) within each valley.

fill the lowest energy four-fold degenerate shell. However, as the interactions become stronger, we find a number of spin and valley transitions, occurring as a result of the competition of the single-particle energy quantization, intra-valley exchange, and correlations.

Together with Dr. Korkusinski, we perform the exact diagonalization study of the four-electron system in the subspaces $S_z = 0$, $S_z = 1$, and $S_z = 2$. The sizes of the Hilbert spaces generated with these spin polarization constraints on the 16 single-particle orbitals are 14400, 8960, and 1820, respectively. By tracking the degeneracies resulting from the commutativity of the total spin operator $\hat{S}$ with the Hamiltonian $\hat{H}_{MB}$, we deal therefore with 1820 states with total spin $S = 2$, 7140 states with $S = 1$, and 5440 states with $S = 0$ within the $S_z = 0$ subspace. Figure 7.5 shows

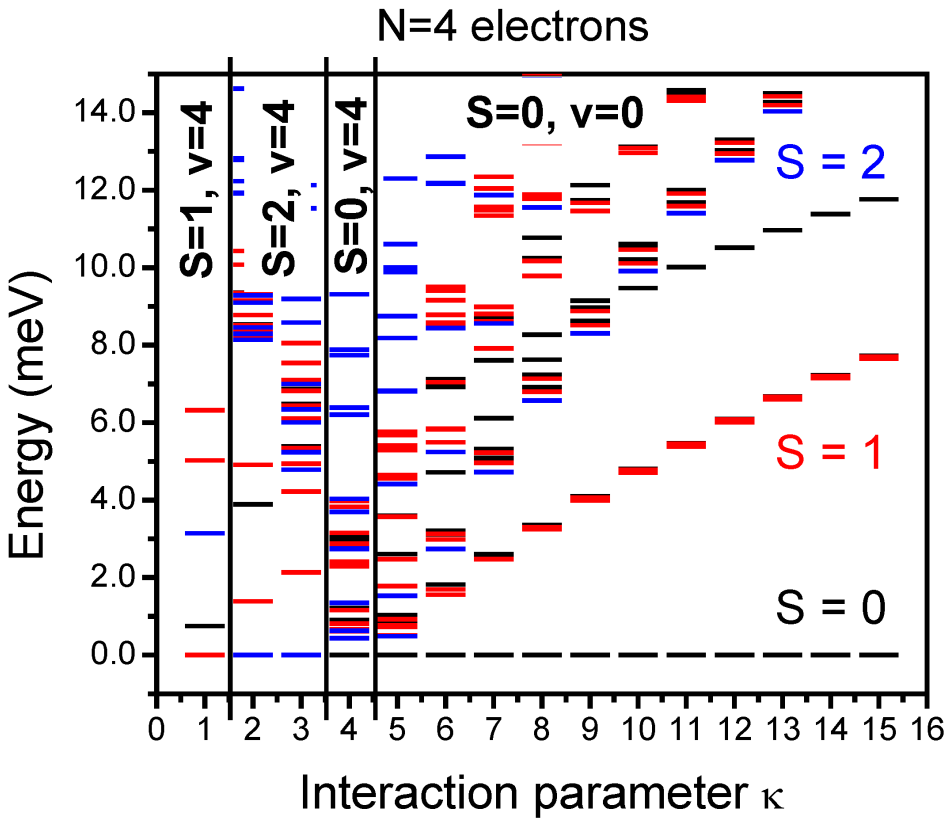

Figure 7.5: Energies of the five lowest-energy correlated states of four electrons as a function of the interaction parameter κ. Black, red, and blue bars show the energies for total spin $S = 0$, 1, and 2 respectively. Black vertical lines show the phase transition points in the four-electron phase diagram, labeled by the total spin S and total valley number v of the ground state.

the energies of the five lowest-energy states from each S_z subspace as a function of the dielectric constant κ. For each κ we set the ground state energy as the reference level. The states with $S = 0$, 1, and 2 are shown with black, red, and blue lines, respectively. As expected, for weak interactions (large κ) we find the spin singlet ground state. However, as we decrease κ (interactions become stronger), we find a series of spin transitions. For $\kappa = 4$ the ground state remains a singlet, but becomes valley-polarized. Further, for $\kappa = 3$ and 2 the ground state is fully spin and valley polarized, and for $\kappa = 1$ the state remains valley polarized, but its total spin decreases to $S = 1$.

The valley polarization is identified by examining the valley-, spin-, and orbital-resolved ground-state charge densities. Figure 7.6 shows the charge densities for $\kappa = 1$

(a), 2 (b), 4 (c), and 5 (d). For the largest κ (the weakest interactions) we are in the regime of the spin- and valley-unpolarized ground state similar to that of the noninteracting electrons. Introducing the valley number $v = N_K - N_{-K}$, where N_ξ is the number of electrons in the valley ξ, we can describe this distribution of electrons by the valley number $v = 0$, since as many electrons are in the valley $K' = -K$ as there are in the valley $+K$. After the first phase transition, i.e., for $\kappa = 4$, we find that the four electrons form an unpolarized state, but they gather in one valley i.e., $v = 4$, as shown in Fig. 7.6 (c). We find another singlet state at the same energy, whose valley quantum number $v = -4$. This is why in Fig. 7.5 we labeled the $\kappa = 4$ case by $S = 0, v = 4$. Further, for $\kappa = 3$ as well as $\kappa = 2$ the four electrons become fully polarized as well as being confined only in one valley K, i.e., $v = 4$. This valley symmetry broken state for $\kappa = 2$ is shown in Fig. 7.6(b). This state is one of the two degenerate configurations, the other one being $v = -4$, with all electrons in the valley $-K$. Consequently, in Fig. 7.5 we identified the $\kappa = 3$ and $\kappa = 2$ cases by $S = 2, v = 4$. Finally, for $\kappa = 1$ (Fig. 7.6(a)) we find a partially spin-polarized, but fully valley-polarized system, in this case, $S = 1, v = 4$. The configuration presented here is degenerate with its companion with $v = -4$, and the quantum number $v = 4$ is used in the label for $\kappa = 1$ in Fig. 7.5.

Let us now discuss the progression of spin and valley phases in terms of the competition of different energy scales. Starting with large values of κ (weak interactions), the only relevant energy scale is the single-particle one. The system will therefore form the valley- and spin-unpolarized ground state as it can fill completely the lowest valley manifold. As κ decreases (interactions become stronger), the intra-valley exchange increases and begins to favour spin-polarized states. First, as is evident in Fig. 7.6(c) for $\kappa = 4$, it will cause the electrons to gather in one valley. Here, without changing the spin polarization, the contribution of the exchange energy is markedly increased, as the pairs of like-spin electrons begin to interact, which was not the case in the valley-unpolarized configuration. This energy gain is greater than the increase of the single-particle energy needed to satisfy the Pauli exclusion. For

even stronger interactions, $\kappa = 3$ and 2, the full spin polarization brings a gain in the exchange energy which is sufficiently large to outweigh the population of even higher single-particle orbitals, as shown in Fig. 7.6(b). However, the final spin transition, to $S = 1$ for $\kappa = 1$, does not appear to follow this trend. It can be understood if we account for the fact that with the decrease of κ the direct repulsive interactions increase as well. As a result, the electrons redistribute to be as far apart as possible.

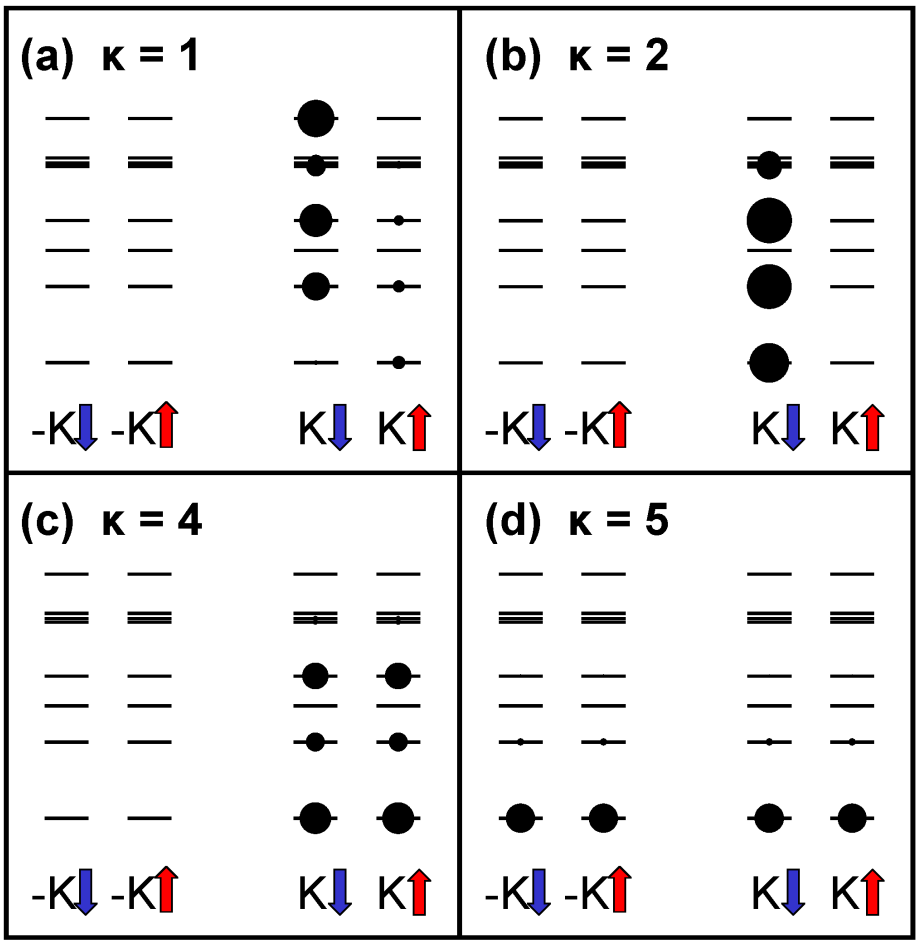

Figure 7.6: Charge density of the four-electron ground state on the single-particle orbitals for $\kappa = 1$ (a), $\kappa = 2$ (b), $\kappa = 4$ (c), and $\kappa = 5$ (d). We resolve the orbitals from valley $K' = -K$ (left double ladder) and K (right double ladder), as well as spin down (left) and up (right) within each valley.

This is realized by creating a complex, correlated state, in which most of the orbitals are fractionally occupied, as shown in Fig. 7.6(a). It appears that the $S = 1$ configurations can realize this redistribution of the charge density more efficiently than the higher-spin configurations with this choice of the single-particle basis owing

to the Pauli exclusion principle. We should note though that these calculations are carried out for fixed basis of 16 single-particle states. Correlations in different total spin subspaces may differently respond to finite basis and results presented here may depend on the basis size [198].

7.4 Spin and valley phases for two to six interacting electrons

In addition to the cases with $N = 2$ and 4, we performed exact diagonalization studies in all relevant S_z subspaces for $N = 3$, 5, and 6. We focus here on $N = 6$ which corresponds to a filled lowest energy shell with 4 electrons and a half-filled second energy shell with $N = 2$ electrons. In this most challenging case of $N = 6$, the Hilbert space sizes were 313600 configurations for $S_z = 0$, 218400 for $S_z = 1$, 69888 for $S_z = 2$, and 8008 configurations for $S_z = 3$. For each electron number we extract the total spin S of the ground state, as well as the valley number v. As in the case of $N = 4$, for the valley-polarized states we always find the ground states in the form of doublets with $\pm v$, which we label simply by the magnitude $|v|$. Figure 7.7 shows the spin (a) and valley (b) phase diagram of N electrons as a function of the interaction parameter κ. In both degrees of freedom we find a rich stability map of different spin and valley polarizations. For the weakest interactions (largest κ) the ground-state configuration follows that of noninteracting electrons, and typically results in a phase with the relatively low spin and without any valley polarization. However, as interactions grow stronger (as one moves to the left of both diagrams) we observe generally an increase in total spin and a breaking of the valley symmetry, revealed by the increase of the valley quantum number v. The spin-flip transitions do not necessarily coincide with the valley-flip transitions, as discussed above for the case $N = 4$. The principle underlying these transitions is the competition of the exchange and single-particle quantization in the total energy of the system. States with low single-particle energy are usually not polarized, while

subsequent spin flips increase the single-particle energy because of the Pauli principle. On the other hand, the increasing spin and valley polarization allows to maximize the intra-valley exchange energy, which lowers the total energy of the system. The gain

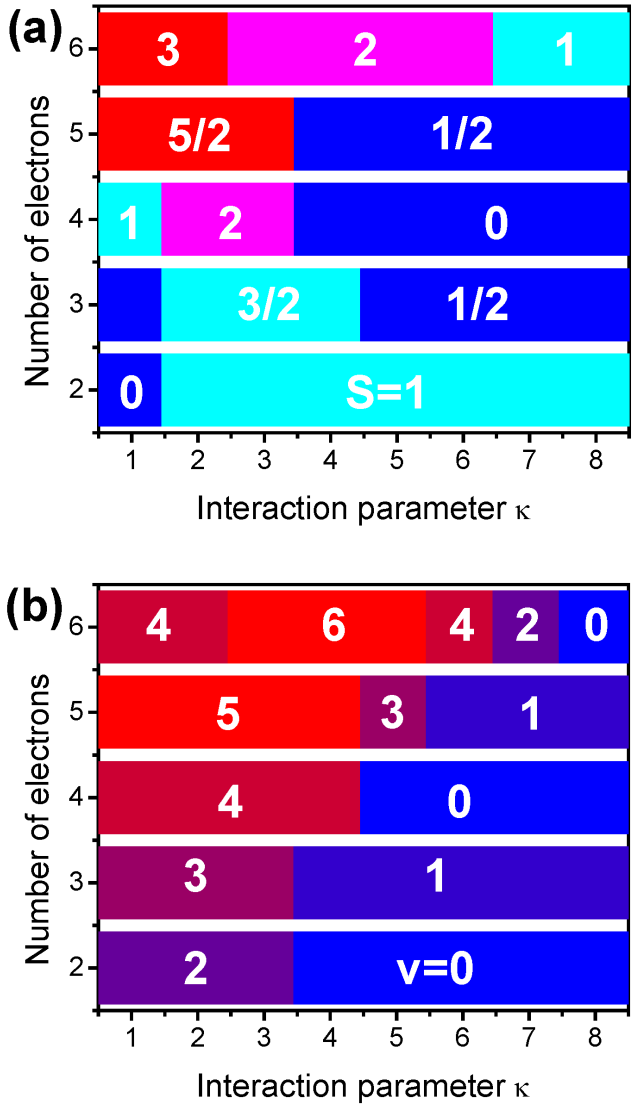

Figure 7.7: Phase diagram for $N = 2$ to 6 electrons showing the stability regions for ground states with spin S (a) and valley number v (b) as a function of the interaction parameter κ.

in exchange exceeds the single-particle energy loss for sufficiently strong interactions, particularly if the electrons form a symmetry broken, valley-polarized state. However, for very strong interactions ($\kappa = 1$) the electronic ground state may actually be of low spin polarization (such as for $N = 2$, 3, and 4) or may exhibit a lower valley polarization than maximal (such as for $N = 6$). This is the result of the increase

of direct electron-electron repulsion, which begins to dominate the total interaction energy of the electrons. To decrease this repulsion, the system organizes itself in a correlated state, as discussed for $N = 4$, in which the electrons increase their average distance by lowering their total spin and/or total valley polarization.

By comparing the spin and valley phase of the two-electron system computed here to the recent experimental results [64, 196] we find that the current experimental conditions correspond to the relatively weakly interacting regime. In order to explore the phase diagrams presented here one therefore needs to increase the effect of interactions. The means of tuning the small parameter varying the interaction strength with respect to the single-particle quantization proposed here is via the effective dielectric constant κ. An alternative is to vary quantum dot size and depth of confining potential. This can be done, e.g., by increasing the radius of the quantum dot, which effectively decreases the single-particle energy scale Δ relative to the interaction strength. A theoretical analysis of the phase diagram of 2 and 6 electrons in the monolayer MoS_2 quantum dot was recently reported using precisely this way of relative tuning of the energy scales [33]. A theoretical and computational estimation of the realistic dielectric constant for a given sample geometry requires one to consider the dynamical screening of the Coulomb interactions both by the valence-band electrons in the bilayer graphene and by the metallic gates defining the lateral quantum dot. Results of this self-consistent approach will be reported at a later date.

7.5 Conclusion

In conclusion, using the atomistic approach and exact diagonalization tools we have predicted theoretically the spin and valley phase diagram of $N = 2$ to $N = 6$ electrons confined in the bilayer graphene quantum dot as a function of the strength of Coulomb interactions. We found a rich phase diagram both for the spin and valley degree of freedom. In the regime of weak Coulomb interactions, the electrons are arranged in the lowest-single-particle energy configurations with low total spin and a valley-unpolarized state. As the interactions are made stronger, the single-particle energy

quantization competes with the direct and exchange Coulomb terms, leading to an increasing spin and valley polarization. The degree of spin and valley polarization, which can be interpreted as a spontaneous valley symmetry breaking, is mitigated by correlation effects in the regime of strongest interactions.

Chapter 8

Conclusions

In this thesis, we have conducted a study of the electronic and optical properties of 2D materials, with a particular focus on graphene-based nanostructures. The understanding of these materials is important because of their potential in shaping future technology.

In Chapter 2, we introduced the methods and tools used throughout this thesis in order to compute the electronic and optical properties of materials. We began by introducing the tight-binding model, and applied it to graphene nanostructures. We then introduced the many-body Hamiltonian and discussed various ways to solve the Hamiltonian by either exact diagonalization approaches or mean-field approaches. The bulk of the calculations in this thesis were a result of numerical simulations, and as such numerical methods were also discussed in this section.

In Chapter 3, we studied the electronic properties of hexagonal graphene quantum dots with different edge types using a tight-binding approach. Our focus was on understanding the origin of the bandgap in zigzag and armchair edged quantum dots. By decomposing the quantum dots into concentric rings that either contain or do not contain a Lieb cluster, we found that the gap can be attributed to states of the concentric ring or to zero-energy states of the Lieb cluster. This leads to an oscillation of the energy gap as a function of size for different quantum dot edges.

In Chapter 4, we described how to construct a quantum simulator of an extended bipartite Hubbard model with broken sublattice symmetry using a structured lateral

gate confining two dimensional electrons in a quantum well into artificial minima arranged in a hexagonal lattice. The sublattice symmetry breaking was generated by forming an artificial triangular graphene quantum dot with zigzag edges. We demonstrated that in artificial graphene quantum dots, by tuning U/t, we can reach two distinct regimes, a semi-metallic and antiferromagnetic. We showed for small systems that in both the metallic and AF regimes, the system at half-filling is partially spin polarized in agreement with Lieb's theorem. The addition or removal of an electron in both regimes collapses the energy gap and spin polarization. Such a simulator would allow simulation of larger systems, verification of results presented here and potential discovery of new phases resulting from strong electron-electron interactions in hexagonal lattice systems inherent in graphene and transition metal dichalcogenites. The expectation of new phases arises from the analogy of the degenerate zero energy shell with the lowest Landau level and the resulting many phases of the fractional quantum Hall effect.

In Chapter 5, we examined the edge states in HgTe quantum dots with a focus on square and circular geometries. We used a four-band $\vec{k} \cdot \vec{p}$ Bernevig-Hughes-Zhang Hamiltonian to describe the system and studied both the topologically trivial and non-trivial regimes. In the non-trivial regime, we found that the edge states are equally spaced within the bulk gap and localized at the edges of the circular and square quantum dots. We also investigated the effects of strain, which we modeled using a Bir-Pikus Hamiltonian. By tuning the strain, we were able to transition between the trivial and non-trivial topological regimes. Our findings provide new insights into the behavior of edge states in HgTe quantum dots and have potential implications for strain driven sensors.

In Chapters 6 and 7, we investigated the electronic and optical properties of gated bilayer graphene quantum dots. In Chapter 6, we used a tight-binding approach to obtain the single-particle spectrum, and then solved the BSE to predict excitons in AB-stacked biased bilayer graphene quantum dots. We found that the two lowest energy transition dipole matrix elements between quantum dot states were negligibly

small, while the third lowest energy transition had a large non-zero value. This was due to spin, valley, conservation of angular momentum, and the radial overlap of the single-particle wavefunctions. We computed excitons in this quantum dot by including electron-electron interactions and solving the BSE, and observed a band of dark low-energy excitonic states. In Chapter 7, we explored the N-electron ground state of bilayer graphene quantum dots as a function of interaction strength and identified a complex phase diagram for $N = 2 - 6$ electrons. We found that the ground state as a function of strength of interaction for different number of electrons underwent many different phase transitions which was a consequence of the competition between the single-particle energy level spacing, with interaction strength. For very strong interactions, correlations began to play a role in the complex nature of the phase diagram.

Chapter 9

Bibliography

[1] Alev Devrim Guclu, Pawel Potasz, Marek Korkusinski, and Pawel Hawrylak. *Graphene Quantum Dots*. Springer Verlag, Berlin Heidelberg, 2014.

[2] Philip Richard Wallace. The band theory of graphite. *Physical Review*, 71(9):622, 1947.

[3] Kostya S Novoselov, Andre K Geim, Sergei Vladimirovich Morozov, Dingde Jiang, Michail I Katsnelson, IVa Grigorieva, SVb Dubonos, and AA Firsov. Two-dimensional gas of massless Dirac Fermions in graphene. *Nature*, 438(7065):197–200, 2005.

[4] Yuanbo Zhang, Yan-Wen Tan, Horst L Stormer, and Philip Kim. Experimental observation of the quantum Hall effect and Berry's phase in graphene. *Nature*, 438(7065):201–204, 2005.

[5] AH Castro Neto, Francisco Guinea, Nuno MR Peres, Kostya S Novoselov, and Andre K Geim. The electronic properties of graphene. *Reviews of Modern Physics*, 81(1):109, 2009.

[6] Kostya S Novoselov, Andre K Geim, Sergei V Morozov, De-eng Jiang, Yanshui Zhang, Sergey V Dubonos, Irina V Grigorieva, and Alexandr A Firsov. Electric field effect in atomically thin carbon films. *Science*, 306(5696):666–669, 2004.

[7] SY Zhou, G-H Gweon, J Graf, AV Fedorov, CD Spataru, RD Diehl, Y Kopelevich, D-H Lee, Steven G Louie, and A Lanzara. First direct observation of Dirac Fermions in graphite. *Nature Physics*, 2(9):595–599, 2006.

[8] Johannes Güttinger, T Frey, C Stampfer, T Ihn, and K Ensslin. Spin states in graphene quantum dots. *Physical Review Letters*, 105(11):116801, 2010.

[9] Shiyong Wang, Liang Z Tan, Weihua Wang, Steven G Louie, and Nian Lin. Manipulation and characterization of aperiodical graphene structures created in a two-dimensional electron gas. *Physical Review Letters*, 113(19):196803, 2014.

[10] Andre K Geim and Konstantin S Novoselov. The rise of graphene. *Nature Materials*, 6(3):183–191, 2007.

[11] Eduardo V Castro, Kostya S Novoselov, Sergey V Morozov, NMR Peres, JMB Lopes Dos Santos, Johan Nilsson, F Guinea, AK Geim, and AH Castro Neto. Electronic properties of a biased graphene bilayer. *Journal of Physics: Condensed Matter*, 22(17):175503, 2010.

[12] Paolo E Trevisanutto, Christine Giorgetti, Lucia Reining, Massimo Ladisa, and Valerio Olevano. Ab initio g w many-body effects in graphene. *Physical Review Letters*, 101(22):226405, 2008.

[13] DM Hoffman, PC Eklund, RE Heinz, P Hawrylak, and KR Subbaswamy. Effect of c-axis dispersion on the optical properties of acceptor-type graphite intercalation compounds. *Physical Review B*, 31(6):3973, 1985.

[14] Yafis Barlas, T Pereg-Barnea, Marco Polini, Reza Asgari, and AH MacDonald. Chirality and correlations in graphene. *Physical Review Letters*, 98(23):236601, 2007.

[15] Edward McCann and Vladimir I Fal'ko. Landau-level degeneracy and quantum hall effect in a graphite bilayer. *Physical Review Letters*, 96(8):086805, 2006.

[16] E. McCann, D. S.L. Abergel, and V. I. Fal'ko. The low energy electronic band structure of bilayer graphene. *Eur. Phys. J. Special Topics*, 148(1):91–103, 2007.

[17] Edward McCann and Mikito Koshino. The electronic properties of bilayer graphene. *Reports on Progress in Physics*, 76(5):056503, 2013.

[18] Yuanbo Zhang, Tsung-Ta Tang, Caglar Girit, Zhao Hao, Michael C. Martin, Alex Zettl, Michael F. Crommie, Y. Ron Shen, and Feng Wang. Direct observation of a widely tunable bandgap in bilayer graphene. *Nature*, 459(7248):820–823, June 2009.

[19] Feng Wang, Yuanbo Zhang, Chuanshan Tian, Caglar Girit, Alex Zettl, Michael Crommie, and Y Ron Shen. Gate-variable optical transitions in graphene. *Science*, 320(5873):206–209, 2008.

[20] Hongki Min, Bhagawan Sahu, Sanjay K Banerjee, and AH MacDonald. Ab initio theory of gate induced gaps in graphene bilayers. *Physical Review B*, 75(15):155115, 2007.

[21] Masato Aoki and Hiroshi Amawashi. Dependence of band structures on stacking and field in layered graphene. *Solid State Communications*, 142(3):123–127, April 2007.

[22] Paola Gava, Michele Lazzeri, A. Marco Saitta, and Francesco Mauri. Ab initio study of gap opening and screening effects in gated bilayer graphene. *Phys. Rev. B*, 79(16):165431, April 2009. Publisher: American Physical Society.

[23] L. A. Falkovsky. Gate-tunable bandgap in bilayer graphene. *Journal of Experimental and Theoretical Physics*, 110(2):319–324, February 2010.

[24] Taisuke Ohta, Aaron Bostwick, Thomas Seyller, Karsten Horn, and Eli Rotenberg. Controlling the Electronic Structure of Bilayer Graphene. *Science*, 313(5789):951–954, August 2006. Publisher: American Association for the Advancement of Science.

[25] Kin Fai Mak, Chun Hung Lui, Jie Shan, and Tony F Heinz. Observation of an electric-field-induced band gap in bilayer graphene by infrared spectroscopy. *Physical Review Letters*, 102(25):256405, 2009.

[26] Eduardo V Castro, KS Novoselov, SV Morozov, NMR Peres, JMB Lopes Dos Santos, Johan Nilsson, F Guinea, AK Geim, and AH Castro Neto. Biased bilayer graphene: semiconductor with a gap tunable by the electric field effect. *Physical Review Letters*, 99(21):216802, 2007.

[27] A. B. Kuzmenko, L. Benfatto, E. Cappelluti, I. Crassee, D. van der Marel, P. Blake, K. S. Novoselov, and A. K. Geim. Gate tunable infrared phonon anomalies in bilayer graphene. *Phys. Rev. Lett.*, 103(11):116804, September 2009. Publisher: American Physical Society.

[28] Jeroen B. Oostinga, Hubert B. Heersche, Xinglan Liu, Alberto F. Morpurgo, and Lieven M. K. Vandersypen. Gate-induced insulating state in bilayer graphene devices. *Nature Materials*, 7(2):151–157, February 2008.

[29] K. S. Novoselov, E. McCann, S. V. Morozov, V. I. Fal'ko, M. I. Katsnelson, U. Zeitler, D. Jiang, F. Schedin, and A. K. Geim. Unconventional quantum Hall effect and Berry's phase of 2π in bilayer graphene. *Nature Physics*, 2(3):177–180, March 2006.

[30] Cheol-Hwan Park and Nicola Marzari. Berry phase and pseudospin winding number in bilayer graphene. *Physical Review B*, 84(20):205440, 2011.

[31] Marius Eich, František Herman, Riccardo Pisoni, Hiske Overweg, Annika Kurzmann, Yongjin Lee, Peter Rickhaus, Kenji Watanabe, Takashi Taniguchi, Manfred Sigrist, et al. Spin and valley states in gate-defined bilayer graphene quantum dots. *Physical Review X*, 8(3):031023, 2018.

[32] Abdulmenaf Altıntaş, Maciej Bieniek, Amintor Dusko, Marek Korkusiński, Jarosław Pawłowski, and Paweł Hawrylak. Spin-valley qubits in gated quantum

dots in a single layer of transition metal dichalcogenides. *Physical Review B*, 104(19):195412, 2021.

[33] Ludmiła Szulakowska, Moritz Cygorek, Maciej Bieniek, and Paweł Hawrylak. Valley-and spin-polarized broken-symmetry states of interacting electrons in gated MoS2 quantum dots. *Physical Review B*, 102(24):245410, 2020.

[34] Luca Banszerus, Alexander Rothstein, Thomas Fabian, S Moller, Eike Icking, Stefan Trellenkamp, Florian Lentz, Daniel Neumaier, Kenji Watanabe, Takashi Taniguchi, et al. Electron–hole crossover in gate-controlled bilayer graphene quantum dots. *Nano Letters*, 20(10):7709–7715, 2020.

[35] Luca Banszerus, Benedikt Frohn, Alexander Epping, Daniel Neumaier, Kenji Watanabe, Takashi Taniguchi, and Christoph Stampfer. Gate-defined electron–hole double dots in bilayer graphene. *Nano Letters*, 18(8):4785–4790, 2018.

[36] Marius Eich, Riccardo Pisoni, Alessia Pally, Hiske Overweg, Annika Kurzmann, Yongjin Lee, Peter Rickhaus, Kenji Watanabe, Takashi Taniguchi, Klaus Ensslin, et al. Coupled quantum dots in bilayer graphene. *Nano Letters*, 18(8):5042–5048, 2018.

[37] Annika Kurzmann, Hiske Overweg, Marius Eich, Alessia Pally, Peter Rickhaus, Riccardo Pisoni, Yongjin Lee, Kenji Watanabe, Takashi Taniguchi, Thomas Ihn, et al. Charge detection in gate-defined bilayer graphene quantum dots. *Nano Letters*, 19(8):5216–5221, 2019.

[38] J Milton Pereira, P Vasilopoulos, and FM Peeters. Tunable quantum dots in bilayer graphene. *Nano Letters*, 7(4):946–949, 2007.

[39] M Zarenia, B Partoens, T Chakraborty, and FM Peeters. Electron-electron interactions in bilayer graphene quantum dots. *Physical Review B*, 88(24):245432, 2013.

[40] Y. Arakawa and H. Sakaki. Multidimensional quantum well laser and temperature dependence of its threshold current. *Applied Physics Letters*, 40(11):939–941, 1982.

[41] S Fafard, K Hinzer, S Raymond, M Dion, J McCaffrey, Y Feng, and S Charbonneau. Red-emitting semiconductor quantum dot lasers. *Science*, 274(5291):1350–1353, 1996.

[42] M Bayer, Pawel Hawrylak, K Hinzer, S Fafard, Marek Korkusinski, ZR Wasilewski, O Stern, and A Forchel. Coupling and entangling of quantum states in quantum dot molecules. *Science*, 291(5503):451–453, 2001.

[43] M Ciorga, AS Sachrajda, Pawel Hawrylak, C Gould, Piotr Zawadzki, S Jullian, Y Feng, and Zbigniew Wasilewski. Addition spectrum of a lateral dot from Coulomb and spin-blockade spectroscopy. *Physical Review B*, 61(24):R16315, 2000.

[44] Oliver Benson, Charles Santori, Matthew Pelton, and Yoshihisa Yamamoto. Regulated and entangled photons from a single quantum dot. *Physical Review Letters*, 84:2513–2516, Mar 2000.

[45] I. Schwartz, D. Cogan, E. R. Schmidgall, Y. Don, L. Gantz, O. Kenneth, N. H. Lindner, and D. Gershoni. Deterministic generation of a cluster state of entangled photons. *Science*, 354(6311):434–437, 2016.

[46] Patrick Laferrière, Edith Yeung, Marek Korkusinski, Philip J Poole, Robin L Williams, Dan Dalacu, Jacob Manalo, Moritz Cygorek, Abdulmenaf Altintas, and Pawel Hawrylak. Systematic study of the emission spectra of nanowire quantum dots. *Applied Physics Letters*, 118(16):161107, 2021.

[47] C Stampfer, E Schurtenberger, F Molitor, J Guttinger, T Ihn, and K Ensslin. Tunable graphene single electron transistor. *Nano Letters*, 8(8):2378–2383, 2008.

[48] ZZ Zhang, Kai Chang, and FM Peeters. Tuning of energy levels and optical properties of graphene quantum dots. *Physical Review B*, 77(23):235411, 2008.

[49] D Subramaniam, F Libisch, Y Li, C Pauly, V Geringer, R Reiter, T Mashoff, M Liebmann, J Burgdörfer, C Busse, et al. Wave-function mapping of graphene quantum dots with soft confinement. *Physical Review Letters*, 108(4):046801, 2012.

[50] Florian Libisch, Christoph Stampfer, and Joachim Burgdörfer. Graphene quantum dots: Beyond a dirac billiard. *Physical Review B*, 79(11):115423, 2009.

[51] Fereshte Ghahari, Daniel Walkup, Christopher Gutiérrez, Joaquin F Rodriguez-Nieva, Yue Zhao, Jonathan Wyrick, Fabian D Natterer, William G Cullen, Kenji Watanabe, Takashi Taniguchi, et al. An on/off Berry phase switch in circular graphene resonators. *Science*, 356(6340):845–849, 2017.

[52] Christopher D Simpson, J Diedrich Brand, Alexander J Berresheim, Laurence Przybilla, Hans Joachim Räder, and Klaus Müllen. Synthesis of a giant 222 carbon graphite sheet. *Chemistry–A European Journal*, 8(6):1424–1429, 2002.

[53] M Wießner, NS Rodríguez Lastra, J Ziroff, F Forster, P Puschnig, L Dössel, Klaus Müllen, A Schöll, and F Reinert. Different views on the electronic structure of nanoscale graphene: aromatic molecule versus quantum dot. *New Journal of Physics*, 14(11):113008, 2012.

[54] Björn Trauzettel, Denis V Bulaev, Daniel Loss, and Guido Burkard. Spin qubits in graphene quantum dots. *Nature Physics*, 3(3):192–196, 2007.

[55] Motohiko Ezawa. Coulomb blockade in graphene nanodisks. *Physical Review B*, 77(15):155411, 2008.

[56] Wei L Wang, Sheng Meng, and Efthimios Kaxiras. Graphene nanoflakes with large spin. *Nano Letters*, 8(1):241–245, 2008.

[57] Joaquín Fernández-Rossier and J_ J Palacios. Magnetism in graphene nanoislands. *Physical Review Letters*, 99(17):177204, 2007.

[58] AD Güçlü, P Potasz, O Voznyy, M Korkusinski, and P Hawrylak. Magnetism and correlations in fractionally filled degenerate shells of graphene quantum dots. *Physical Review Letters*, 103(24):246805, 2009.

[59] Pawel Hawrylak, François Peeters, and Klaus Ensslin. Carbononics-integrating electronics, photonics and spintronics with graphene quantum dots. *Phys. Status Solidi RRL*, 10:11–12, 2016.

[60] Shiyong Wang, Neerav Kharche, Eduardo Costa Girão, Xinliang Feng, Klaus Mullen, Vincent Meunier, Roman Fasel, and Pascal Ruffieux. Quantum dots in graphene nanoribbons. *Nano Letters*, 17(7):4277–4283, 2017.

[61] Sumit Ghosh and Udo Schwingenschlögl. Hexagonal graphene quantum dots. *Physica Status Solidi (RRL)–Rapid Research Letters*, 11(1):1600226, 2017.

[62] Shen Zhao, Julien Lavie, Loïc Rondin, Lucile Orcin-Chaix, Carole Diederichs, Philippe Roussignol, Yannick Chassagneux, Christophe Voisin, Klaus Müllen, Akimitsu Narita, et al. Single photon emission from graphene quantum dots at room temperature. *Nature Communications*, 9(1):1–5, 2018.

[63] A. Rycerz, J. Tworzydlo, and C. W. J. Beenakker. Valley filter and valley valve in graphene. *Nature Physics*, 3(3):172–175, March 2007. arXiv: cond-mat/0608533.

[64] Annika Kurzmann, Marius Eich, Hiske Overweg, M Mangold, František Herman, Peter Rickhaus, Riccardo Pisoni, Yongjin Lee, Rebekka Garreis, Chuyao Tong, et al. Excited states in bilayer graphene quantum dots. *Physical Review Letters*, 123(2):026803, 2019.

[65] Immanuel Bloch. Ultracold quantum gases in optical lattices. *Nature physics*, 1(1):23–30, 2005.

[66] Marco Gibertini, Achintya Singha, Vittorio Pellegrini, Marco Polini, Giovanni Vignale, Aron Pinczuk, Loren N Pfeiffer, and Ken W West. Engineering artificial graphene in a two-dimensional electron gas. *Physical Review B*, 79(24):241406, 2009.

[67] Carlos Forsythe, Xiaodong Zhou, Kenji Watanabe, Takashi Taniguchi, Abhay Pasupathy, Pilkyung Moon, Mikito Koshino, Philip Kim, and Cory R Dean. Band structure engineering of 2d materials using patterned dielectric superlattices. *Nature nanotechnology*, 13(7):566–571, 2018.

[68] Cheol-Hwan Park and Steven G Louie. Making massless Dirac Fermions from a patterned two-dimensional electron gas. *Nano letters*, 9(5):1793–1797, 2009.

[69] Achintya Singha, M Gibertini, B Karmakar, S Yuan, M Polini, Giovanni Vignale, MI Katsnelson, A Pinczuk, LN Pfeiffer, KW West, et al. Two-dimensional Mott-Hubbard electrons in an artificial honeycomb lattice. *Science*, 332(6034):1176–1179, 2011.

[70] Yutao Li, Scott Dietrich, Carlos Forsythe, Takashi Taniguchi, Kenji Watanabe, Pilkyung Moon, and Cory R Dean. Anisotropic band flattening in graphene with one-dimensional superlattices. *Nature Nanotechnology*, 16(5):525–530, 2021.

[71] Or Peleg, Guy Bartal, Barak Freedman, Ofer Manela, Mordechai Segev, and Demetrios N Christodoulides. Conical diffraction and gap solitons in honeycomb photonic lattices. *Physical Review Letters*, 98(10):103901, 2007.

[72] Kenjiro K Gomes, Warren Mar, Wonhee Ko, Francisco Guinea, and Hari C Manoharan. Designer Dirac Fermions and topological phases in molecular graphene. *Nature*, 483(7389):306–310, 2012.

[73] Thomas Uehlinger, Gregor Jotzu, Michael Messer, Daniel Greif, Walter Hofstetter, Ulf Bissbort, and Tilman Esslinger. Artificial graphene with tunable interactions. *Physical Review Letters*, 111(18):185307, 2013.

[74] Li-kun Shi, Jing Ma, and Justin CW Song. Gate-tunable flat bands in Van der Waals patterned dielectric superlattices. *2D Materials*, 7(1):015028, 2019.

[75] E Räsänen, CA Rozzi, S Pittalis, and G Vignale. Electron-electron interactions in artificial graphene. *Physical Review Letters*, 108(24):246803, 2012.

[76] Ilkka Kylänpää, Fulvio Berardi, Esa Räsänen, Pablo García-González, Carlo Andrea Rozzi, and Angel Rubio. Stability of the Dirac cone in artificial graphene formed in quantum wells: a computational many-electron study. *New Journal of Physics*, 18(8):083014, 2016.

[77] Robert Drost, Teemu Ojanen, Ari Harju, and Peter Liljeroth. Topological states in engineered atomic lattices. *Nature Physics*, 13(7):668–671, 2017.

[78] Marlou R Slot, Thomas S Gardenier, Peter H Jacobse, Guido CP Van Miert, Sander N Kempkes, Stephan JM Zevenhuizen, Cristiane Morais Smith, Daniel Vanmaekelbergh, and Ingmar Swart. Experimental realization and characterization of an electronic Lieb lattice. *Nature Physics*, 13(7):672–676, 2017.

[79] TO Wehling, E Şaşıoğlu, C Friedrich, AI Lichtenstein, MI Katsnelson, and S Blügel. Strength of effective Coulomb interactions in graphene and graphite. *Physical Review Letters*, 106(23):236805, 2011.

[80] Tim O Wehling, Annica M Black-Schaffer, and Alexander V Balatsky. Dirac materials. *Advances in Physics*, 63(1):1–76, 2014.

[81] Sandro Sorella and Erio Tosatti. Semi-metal-insulator transition of the Hubbard model in the honeycomb lattice. *EPL (Europhysics Letters)*, 19(8):699, 1992.

[82] J Salfi, JA Mol, R Rahman, G Klimeck, MY Simmons, LCL Hollenberg, and S Rogge. Quantum simulation of the Hubbard model with dopant atoms in silicon. *Nature Communications*, 7(1):1–6, 2016.

[83] O Voznyy, AD Güçlü, P Potasz, and P Hawrylak. Effect of edge reconstruction and passivation on zero-energy states and magnetism in triangular graphene quantum dots with zigzag edges. *Physical Review B*, 83(16):165417, 2011.

[84] Y Saleem, L Najera Baldo, A Delgado, L Szulakowska, and P Hawrylak. Oscillations of the bandgap with size in armchair and zigzag graphene quantum dots. *Journal of Physics: Condensed Matter*, 31(30):305503, July 2019.

[85] Yasser Saleem, Amintor Dusko, Moritz Cygorek, Marek Korkusinski, and Pawel Hawrylak. Quantum simulator of extended bipartite hubbard model with broken sublattice symmetry: Magnetism, correlations, and phase transitions. *Physical Review B*, 105(20):205105, 2022.

[86] Benjamin Puzantian, Yasser Saleem, Marek Korkusinski, and Pawel Hawrylak. Edge states and strain-driven topological phase transitions in quantum dots in topological insulators. *Nanomaterials*, 12(23):4283, 2022.

[87] Yasser Saleem, Katarzyna Sadecka, Marek Korkusinski, Daniel Miravet, Amintor Dusko, and Pawel Hawrylak. Theory of excitons in gated bilayer graphene quantum dots. *Nano Letters*, 2023.

[88] Bernard J Ransil. Studies in molecular structure. ii. lcao-mo-scf wave functions for selected first-row diatomic molecules. *Reviews of Modern Physics*, 32(2):245, 1960.

[89] Di Xiao, Wang Yao, and Qian Niu. Valley-contrasting physics in graphene: magnetic moment and topological transport. *Physical Review Letters*, 99(23):236809, 2007.

[90] S Das Sarma, Shaffique Adam, EH Hwang, and Enrico Rossi. Electronic transport in two-dimensional graphene. *Reviews of Modern Physics*, 83(2):407, 2011.

[91] Matthew Yankowitz, Shaowen Chen, Hryhoriy Polshyn, Yuxuan Zhang, K Watanabe, T Taniguchi, David Graf, Andrea F Young, and Cory R Dean.

Tuning superconductivity in twisted bilayer graphene. *Science*, 363(6431):1059–1064, 2019.

[92] Grigory Tarnopolsky, Alex Jura Kruchkov, and Ashvin Vishwanath. Origin of magic angles in twisted bilayer graphene. *Physical Review Letters*, 122(10):106405, 2019.

[93] Amol Nimbalkar and Hyunmin Kim. Opportunities and challenges in twisted bilayer graphene: a review. *Nano-Micro Letters*, 12(1):1–20, 2020.

[94] Yuan Cao, Daniel Rodan-Legrain, Oriol Rubies-Bigorda, Jeong Min Park, Kenji Watanabe, Takashi Taniguchi, and Pablo Jarillo-Herrero. Tunable correlated states and spin-polarized phases in twisted bilayer–bilayer graphene. *Nature*, 583(7815):215–220, 2020.

[95] Alexander Kerelsky, Leo J McGilly, Dante M Kennes, Lede Xian, Matthew Yankowitz, Shaowen Chen, K Watanabe, T Taniguchi, James Hone, Cory Dean, et al. Maximized electron interactions at the magic angle in twisted bilayer graphene. *Nature*, 572(7767):95–100, 2019.

[96] Pilkyung Moon and Mikito Koshino. Optical absorption in twisted bilayer graphene. *Physical Review B*, 87(20):205404, 2013.

[97] Alev Devrim Güçlü, P Potasz, and P Hawrylak. Zero-energy states of graphene triangular quantum dots in a magnetic field. *Physical Review B*, 88(15):155429, 2013.

[98] Isil Ozfidan, Marek Korkusinski, and Pawel Hawrylak. Electronic properties and electron–electron interactions in graphene quantum dots. *Physica Status Solidi (RRL)–Rapid Research Letters*, 10(1):13–23, 2016.

[99] Isil Ozfidan, Anna H Trojnar, Marek Korkusinski, and Pawel Hawrylak. Geometry, chirality, topology and electron–electron interactions in the quadruple quantum dot molecule. *Solid State Communications*, 172:15–19, 2013.

[100] Isil Ozfidan, Milos Vladisavljevic, Marek Korkusinski, and Pawel Hawrylak. Electron-electron interactions, topological phase, and optical properties of a charged artificial benzene ring. *Physical Review B*, 92(24):245304, 2015.

[101] Valeri N Kotov, Bruno Uchoa, Vitor M Pereira, F Guinea, and AH Castro Neto. Electron-electron interactions in graphene: Current status and perspectives. *Reviews of Modern Physics*, 84(3):1067, 2012.

[102] Marco Polini, Reza Asgari, Giovanni Borghi, Yafis Barlas, T Pereg-Barnea, and AH MacDonald. Plasmons and the spectral function of graphene. *Physical Review B*, 77(8):081411, 2008.

[103] John Hubbard. Electron correlations in narrow energy bands. *Proceedings of the Royal Society of London. Series A. Mathematical and Physical Sciences*, 276(1365):238–257, 1963.

[104] Elliott H Lieb. Two theorems on the Hubbard model. *Physical Review Letters*, 62(10):1201, 1989.

[105] Gian-Carlo Wick. The evaluation of the collision matrix. *Physical Review*, 80(2):268, 1950.

[106] P Potasz, AD Güçlü, A Wójs, and P Hawrylak. Electronic properties of gated triangular graphene quantum dots: Magnetism, correlations, and geometrical effects. *Physical Review B*, 85(7):075431, 2012.

[107] Vicente Hernandez, Jose E. Roman, and Vicente Vidal. SLEPc: A scalable and flexible toolkit for the solution of eigenvalue problems. *ACM Trans. Math. Software*, 31(3):351–362, 2005.

[108] László Babai. Monte-carlo algorithms in graph isomorphism testing. *Université tde Montréal Technical Report, DMS*, (79-10), 1979.

[109] Mark Galassi, Jim Davies, James Theiler, Brian Gough, Gerard Jungman, Patrick Alken, Michael Booth, Fabrice Rossi, and Rhys Ulerich. *GNU scientific library*. Network Theory Limited Godalming, 2002.

[110] M. Korkusinski, Y. Saleem, D. Miravet, A. Dusko, and P. Hawrylak. Spontaneously broken spin and valley states in bilayer graphene quantum dots. *To Be Published*, 2023.

[111] Weidong Sheng, Shun-Jen Cheng, and Pawel Hawrylak. Multiband theory of multi-exciton complexes in self-assembled quantum dots. *Physical Review B*, 71(3):035316, 2005.

[112] Michał Zieliński, M Korkusiński, and P Hawrylak. Atomistic tight-binding theory of multiexciton complexes in a self-assembled inas quantum dot. *Physical Review B*, 81(8):085301, 2010.

[113] Y Saleem, L Najera Baldo, A Delgado, L Szulakowska, and P Hawrylak. Oscillations of the bandgap with size in armchair and zigzag graphene quantum dots. *Journal of Physics: Condensed Matter*, 31(30):305503, 2019.

[114] AD Güçlü, Pawel Potasz, and Pawel Hawrylak. Excitonic absorption in gate-controlled graphene quantum dots. *Physical Review B*, 82(15):155445, 2010.

[115] Jeil Jung, Tami Pereg-Barnea, and AH MacDonald. Theory of interedge superexchange in zigzag edge magnetism. *Physical Review Letters*, 102(22):227205, 2009.

[116] Gabriel Kotliar and Dieter Vollhardt. Strongly correlated materials: Insights from dynamical mean-field theory. *Physics today*, 57(3):53–60, 2004.

[117] Christie S Chiu, Geoffrey Ji, Annabelle Bohrdt, Muqing Xu, Michael Knap, Eugene Demler, Fabian Grusdt, Markus Greiner, and Daniel Greif. String patterns in the doped hubbard model. *Science*, 365(6450):251–256, 2019.

[118] Ehud Altman, Kenneth R Brown, Giuseppe Carleo, Lincoln D Carr, Eugene Demler, Cheng Chin, Brian DeMarco, Sophia E Economou, Mark A Eriksson, Kai-Mei C Fu, et al. Quantum simulators: Architectures and opportunities. *PRX Quantum*, 2(1):017003, 2021.

[119] Jacob Smith, Aaron Lee, Philip Richerme, Brian Neyenhuis, Paul W Hess, Philipp Hauke, Markus Heyl, David A Huse, and Christopher Monroe. Many-body localization in a quantum simulator with programmable random disorder. *Nature Physics*, 12(10):907–911, 2016.

[120] Iulia Buluta and Franco Nori. Quantum simulators. *Science*, 326(5949):108–111, 2009.

[121] Seth Lloyd. Universal quantum simulators. *Science*, 273(5278):1073–1078, 1996.

[122] Dieter Jaksch and Peter Zoller. The cold atom Hubbard toolbox. *Annals of physics*, 315(1):52–79, 2005.

[123] M Ortner, A Micheli, G Pupillo, and P Zoller. Quantum simulations of extended Hubbard models with dipolar crystals. *New Journal of Physics*, 11(5):055045, 2009.

[124] Anton Mazurenko, Christie S Chiu, Geoffrey Ji, Maxwell F Parsons, Márton Kanász-Nagy, Richard Schmidt, Fabian Grusdt, Eugene Demler, Daniel Greif, and Markus Greiner. A cold-atom Fermi–Hubbard antiferromagnet. *Nature*, 545(7655):462–466, 2017.

[125] Stefan Kuhr. Quantum-gas microscopes: a new tool for cold-atom quantum simulators. *National Science Review*, 3(2):170–172, 2016.

[126] Hendrik Weimer, Markus Müller, Igor Lesanovsky, Peter Zoller, and Hans Peter Büchler. A Rydberg quantum simulator. *Nature Physics*, 6(5):382–388, 2010.

[127] Julio T Barreiro, Markus Müller, Philipp Schindler, Daniel Nigg, Thomas Monz, Michael Chwalla, Markus Hennrich, Christian F Roos, Peter Zoller, and

Rainer Blatt. An open-system quantum simulator with trapped ions. *Nature*, 470(7335):486–491, 2011.

[128] Cornelius Hempel, Christine Maier, Jonathan Romero, Jarrod McClean, Thomas Monz, Heng Shen, Petar Jurcevic, Ben P Lanyon, Peter Love, Ryan Babbush, et al. Quantum chemistry calculations on a trapped-ion quantum simulator. *Physical Review X*, 8(3):031022, 2018.

[129] R Islam, EE Edwards, K Kim, S Korenblit, C Noh, H Carmichael, G-D Lin, L-M Duan, C-C Joseph Wang, JK Freericks, et al. Onset of a quantum phase transition with a trapped ion quantum simulator. *Nature communications*, 2(1):1–6, 2011.

[130] Daniel Leykam, Alexei Andreanov, and Sergej Flach. Artificial flat band systems: from lattice models to experiments. *Advances in Physics: X*, 3(1):1473052, 2018.

[131] Alán Aspuru-Guzik and Philip Walther. Photonic quantum simulators. *Nature physics*, 8(4):285–291, 2012.

[132] Hannes Bernien, Sylvain Schwartz, Alexander Keesling, Harry Levine, Ahmed Omran, Hannes Pichler, Soonwon Choi, Alexander S Zibrov, Manuel Endres, Markus Greiner, et al. Probing many-body dynamics on a 51-atom quantum simulator. *Nature*, 551(7682):579–584, 2017.

[133] Jianming Cai, Alex Retzker, Fedor Jelezko, and Martin B Plenio. A large-scale quantum simulator on a diamond surface at room temperature. *Nature Physics*, 9(3):168–173, 2013.

[134] Amintor Dusko, Alain Delgado, André Saraiva, and Belita Koiller. Adequacy of si: P chains as Fermi–Hubbard simulators. *npj Quantum Information*, 4(1):1–5, 2018.

[135] S Klembt, TH Harder, OA Egorov, K Winkler, R Ge, MA Bandres, M Emmerling, L Worschech, TCH Liew, M Segev, et al. Exciton-polariton topological insulator. *Nature*, 562(7728):552–556, 2018.

[136] Thibaut Jacqmin, Iacopo Carusotto, Isabelle Sagnes, Marco Abbarchi, DD Solnyshkov, Guillaume Malpuech, Elisabeth Galopin, Aristide Lemaître, Jacqueline Bloch, and Alberto Amo. Direct observation of Dirac cones and a flatband in a honeycomb lattice for polaritons. *Physical Review Letters*, 112(11):116402, 2014.

[137] Ignacio Piquero-Zulaica, Jorge Lobo-Checa, Ali Sadeghi, Zakaria M Abd El-Fattah, Chikahiko Mitsui, Toshihiro Okamoto, Rémy Pawlak, Tobias Meier, Andrés Arnau, J Enrique Ortega, et al. Precise engineering of quantum dot array coupling through their barrier widths. *Nature Communications*, 8(1):1–6, 2017.

[138] AD Güçlü, P Potasz, and P Hawrylak. Electric-field controlled spin in bilayer triangular graphene quantum dots. *Physical Review B*, 84(3):035425, 2011.

[139] Isil Ozfidan, Marek Korkusinski, A Devrim Güçlü, John A McGuire, and Pawel Hawrylak. Microscopic theory of the optical properties of colloidal graphene quantum dots. *Physical Review B*, 89(8):085310, 2014.

[140] Boris A. Volkov and Oleg A. Pankratov. Two-dimensional massless electrons in an inverted contact. *Pisma Zh. Eksp. Teor. Fiz.*, 42:145–148, 1985.

[141] B. Andrei Bernevig, Taylor L. Hughes, and Shou-Cheng Zhang. Quantum spin hall effect and topological phase transition in HgTe quantum wells. *Science*, 314(5806):1757–1761, Dec 2006.

[142] Markus Konig, Steffen Wiedmann, Christoph Brune, Andreas Roth, Hartmut Buhmann, Laurens W. Molenkamp, Xiao-Liang Qi, and Shou-Cheng Zhang. Quantum spin hall insulator state in HgTe quantum wells. *Science*, 318(5851):766–770, Nov 2007.

[143] Christoph Brüne, Andreas Roth, Hartmut Buhmann, Ewelina M Hankiewicz, Laurens W Molenkamp, Joseph Maciejko, Xiao-Liang Qi, and Shou-Cheng Zhang. Spin polarization of the quantum spin hall edge states. *Nature Physics*, 8(6):485–490, 2012.

[144] Xiao-Liang Qi and Shou-Cheng Zhang. Topological insulators and superconductors. *Rev. Mod. Phys.*, 83:1057–1110, Oct 2011.

[145] M. Z. Hasan and C. L. Kane. Colloquium: Topological insulators. *Rev. Mod. Phys.*, 82:3045–3067, Nov 2010.

[146] Yoichi Ando. Topological insulator materials. *Journal of the Physical Society of Japan*, 82(10):102001, Oct 2013.

[147] B Andrei Bernevig. *Topological insulators and topological superconductors*. Princeton university press, 2013.

[148] Joseph Maciejko, Taylor L. Hughes, and Shou-Cheng Zhang. The quantum spin hall effect. *Annual Review of Condensed Matter Physics*, 2(1):31–53, 2011.

[149] A. Pertsova, C. M. Canali, and A. H. MacDonald. Quantum hall edge states in topological insulator nanoribbons. *Physical Review B*, 94:121409, Sep 2016.

[150] Peter Schüffelgen, Daniel Rosenbach, Chuan Li, Tobias W Schmitt, Michael Schleenvoigt, Abdur R Jalil, Sarah Schmitt, Jonas Kölzer, Meng Wang, Benjamin Bennemann, et al. Selective area growth and stencil lithography for in situ fabricated quantum devices. *Nature Nanotechnology*, 14(9):825–831, 2019.

[151] B. A. Levitan, L. Goutte, and T. Pereg-Barnea. Surface theory of a second-order topological insulator beyond the Dirac approximation. *Physical Review B*, 104:125105, Sep 2021.

[152] Lucjan Jacak, Pawel Hawrylak, and Arkadiusz Wojs. *Quantum Dots*. Springer Verlag, 1998.

[153] Dieter Bimberg, Marius Grundmann, and Nikolai N. Ledentsov. *Quantum Dot Heterostructures*. John Wiley & Sons, 1999.

[154] Pawel Hawrylak and Marek Korkusiński. *Electronic properties of self-assembled quantum dots*. Springer, 2003.

[155] Eva Izquierdo, Adrien Robin, Sean Keuleyan, Emmanuel L'huillier, and Sandrine Ithurria. Strongly confined HgTe 2d nanoplatelets as narrow near-infrared emitters. *Journal of the American Chemical Society*, 138(33):10496–10501, 2016.

[156] Nicolas Moghaddam, Charlie Greboval, Junling Qu, Audrey Chu, Prachi Rastogi, Clément Livache, Adrien Khalili, Xiang Zhen Xu, Benoit Baptiste, Stefan Klotz, et al. The strong confinement regime in HgTe two-dimensional nanoplatelets. *The Journal of Physical Chemistry C*, 124(42):23460–23468, 2020.

[157] Sean Keuleyan, Emmanuel Lhuillier, and Philippe Guyot-Sionnest. Synthesis of colloidal HgTe quantum dots for narrow mid-IR emission and detection. *Journal of the American Chemical Society*, 133(41):16422–16424, 2011.

[158] Sean Keuleyan, Emmanuel Lhuillier, Vuk Brajuskovic, and Philippe Guyot-Sionnest. Mid-infrared HgTe colloidal quantum dot photodetectors. *Nature Photonics*, 5(8):489–493, 2011.

[159] R De Picciotto, HL Stormer, Amnon Yacoby, LN Pfeiffer, KW Baldwin, and KW West. 2d-1d coupling in cleaved edge overgrowth. *Physical Review Letters*, 85(8):1730, 2000.

[160] Liang Fu and C. L. Kane. Topological insulators with inversion symmetry. *Physical Review B*, 76:045302, Jul 2007.

[161] Kai Chang and Wen-Kai Lou. Helical quantum states in HgTe quantum dots with inverted band structures. *Physical Review Letters*, 106:206802, May 2011.

[162] Jian Li, Wen-Kai Lou, Dong Zhang, Xiao-Jing Li, Wen Yang, and Kai Chang. Single- and few-electron states in topological-insulator quantum dots. *Physical Review B*, 90:115303, Sep 2014.

[163] Wen-Kai Lou, Wen Yang, and Kai Chang. Helical conducting edge states in narrow-gap semiconductors without band inversion. *Physical Review B*, 105:045305, Jan 2022.

[164] Fan Liu, Jian Li, and Jia-Ji Zhu. The single and coupled BHZ quantum dots with spin-orbit interaction. *Solid State Communications*, 330:114275, 2021.

[165] J. Li, S. Zhang, Jian, and Jia-Ji Zhu. Electronic structure of rectangular HgTe quantum dots. *Phys. E*, 93:58–62, 2017.

[166] Marek Korkusinski and Pawel Hawrylak. Quantum strain sensor with a topological insulator HgTe quantum dot. *Scientific Reports*, 4(1):1–6, 2014.

[167] M.T. Czyzyk and M. Podgorny. Energy bands and optical properties of HgTe and cdte calculated on the basis of the tight-binding model with spin-orbit interaction. *Phys. Stat. Solidi. B*, 98:507, 1980.

[168] Dušan B Topalović, Vladimir V Arsoski, Milan Ž Tadić, and François M Peeters. Confined electron states in two-dimensional HgTe in magnetic field: Quantum dot versus quantum ring behavior. *Physical Review B*, 100:125304, Sep 2019.

[169] Guy Allan and Christophe Delerue. Tight-binding calculations of the optical properties of HgTe nanocrystals. *Physical Review B*, 86:165437, Oct 2012.

[170] Witold Trzeciakowski. Effective-mass approximation in semiconductor heterostructures: One-dimensional analysis. *Physical Review B*, 38:12493–12507, Dec 1988.

[171] Witold Trzeciakowski. Boundary conditions and interface states in heterostructures. *Physical Review B*, 38:4322–4325, Aug 1988.

[172] E. G. Novik, A. Pfeuffer-Jeschke, T. Jungwirth, V. Latussek, C. R. Becker, G. Landwehr, H. Buhmann, and L. W. Molenkamp. Band structure of semimagnetic $Hg_{1-y}Mn_yTe$ quantum wells. *Physical Review B*, 72:035321, Jul 2005.

[173] Chris G. Van de Walle. Band lineups and deformation potentials in the model-solid theory. *Physical Review B*, 39:1871–1883, Jan 1989.

[174] Jason Alicea. New directions in the pursuit of Majorana Fermions in solid state systems. *Reports on progress in physics*, 75(7):076501, 2012.

[175] Chang-Yu Hsieh, Yun-Pil Shim, Marek Korkusinski, and Pawel Hawrylak. Physics of lateral triple quantum-dot molecules with controlled electron numbers. *Reports on Progress in Physics*, 75(11):114501, 2012.

[176] Guido Burkard, Thaddeus D Ladd, John M Nichol, Andrew Pan, and Jason R Petta. Semiconductor spin qubits. *arXiv preprint arXiv:2112.08863*, 2021.

[177] F Pelayo García de Arquer, Dmitri V Talapin, Victor I Klimov, Yasuhiko Arakawa, Manfred Bayer, and Edward H Sargent. Semiconductor quantum dots: Technological progress and future challenges. *Science*, 373(6555):eaaz8541, 2021.

[178] M Bayer, O Stern, P Hawrylak, S Fafard, and A Forchel. Hidden symmetries in the energy levels of excitonic 'artificial atoms'. *Nature*, 405(6789):923–926, 2000.

[179] P Hawrylak, GA Narvaez, M Bayer, and A Forchel. Excitonic absorption in a quantum dot. *Physical Review Letters*, 85(2):389, 2000.

[180] Ido Schwartz, Dan Cogan, Emma R Schmidgall, Yaroslav Don, Liron Gantz, Oded Kenneth, Netanel H Lindner, and David Gershoni. Deterministic generation of a cluster state of entangled photons. *Science*, 354(6311):434–437, 2016.

[181] Patrick Laferrière, Edith Yeung, Marek Korkusinski, Philip J Poole, Robin L Williams, Dan Dalacu, Jacob Manalo, Moritz Cygorek, Abdulmenaf Altintas, and Pawel Hawrylak. Systematic study of the emission spectra of nanowire quantum dots. *Applied Physics Letters*, 118(16):161107, 2021.

[182] J Blinowski, Nguyen Hy Hau, C Rigaux, JP Vieren, R Le Toullec, G Furdin, A Herold, and J Melin. Band structure model and dynamical dielectric function in lowest stages of graphite acceptor compounds. *Journal de Physique*, 41(1):47–58, 1980.

[183] D.M. Hoffman, P.C. Eklund, R.E. Heinz, P. Hawrylak, and K.R. Subbaswamy. Effect of c axis dispersion on the optical properties of acceptor graphite intercalation compounds. *Phys. Rev. B*, 31:6592, 1985.

[184] L. M. Zhang, Z. Q. Li, D. N. Basov, M. M. Fogler, Z. Hao, and M. C. Martin. Determination of the electronic structure of bilayer graphene from infrared spectroscopy. *Phys. Rev. B*, 78:235408, Dec 2008.

[185] Long Ju, Lei Wang, Ting Cao, Takashi Taniguchi, Kenji Watanabe, Steven G Louie, Farhan Rana, Jiwoong Park, James Hone, Feng Wang, et al. Tunable excitons in bilayer graphene. *Science*, 358(6365):907–910, 2017.

[186] Denis A Bandurin, Dmitry Svintsov, Igor Gayduchenko, Shuigang G Xu, Alessandro Principi, Maxim Moskotin, Ivan Tretyakov, Denis Yagodkin, Sergey Zhukov, Takashi Taniguchi, et al. Resonant terahertz detection using graphene plasmons. *Nature Communications*, 9(1):1–8, 2018.

[187] Cheol-Hwan Park and Steven G. Louie. Tunable Excitons in Biased Bilayer Graphene. *Nano Letters*, 10(2):426–431, February 2010. Publisher: American Chemical Society.

[188] J. C. G. Henriques, Itai Epstein, and N. M. R. Peres. Absorption and optical selection rules of tunable excitons in biased bilayer graphene. *Phys. Rev. B*, 105(4):045411, January 2022. Publisher: American Physical Society.

[189] Fan Zhang, Jeil Jung, Gregory A Fiete, Qian Niu, and Allan H MacDonald. Spontaneous quantum hall states in chirally stacked few-layer graphene systems. *Physical Review Letters*, 106(15):156801, 2011.

[190] Luca Banszerus, Samuel Möller, Corinne Steiner, Eike Icking, Stefan Trellenkamp, Florian Lentz, Kenji Watanabe, Takashi Taniguchi, Christian Volk, and Christoph Stampfer. Spin-valley coupling in single-electron bilayer graphene quantum dots. *Nature Communications*, 12(1):1–7, 2021.

[191] Jia Ning Leaw, Ho-Kin Tang, Pinaki Sengupta, Fakher F Assaad, Igor F Herbut, and Shaffique Adam. Electronic ground state in bilayer graphene with realistic Coulomb interactions. *Physical Review B*, 100(12):125116, 2019.

[192] Pawel Hawrylak. Single-electron capacitance spectroscopy of few-electron artificial atoms in a magnetic field: Theory and experiment. *Physical Review Letters*, 71(20):3347, 1993.

[193] S Raymond, S Studenikin, A Sachrajda, Z Wasilewski, Shun-Jen Cheng, W Sheng, P Hawrylak, A Babinski, M Potemski, G Ortner, et al. Excitonic energy shell structure of self-assembled InGaAs/GaAs quantum dots. *Physical Review Letters*, 92(18):187402, 2004.

[194] Rebekka Garreis, Angelika Knothe, Chuyao Tong, Marius Eich, Carolin Gold, Kenji Watanabe, Takashi Taniguchi, Vladimir Fal'ko, Thomas Ihn, Klaus Ensslin, et al. Shell filling and trigonal warping in graphene quantum dots. *Physical Review Letters*, 126(14):147703, 2021.

[195] Anastasia Varlet, Marcin Mucha-Kruczyński, Dominik Bischoff, Pauline Simonet, Takashi Taniguchi, Kenji Watanabe, Vladimir Fal'ko, Thomas Ihn, and Klaus Ensslin. Tunable Fermi surface topology and Lifshitz transition in bilayer graphene. *Synthetic Metals*, 210:19–31, 2015.

[196] Annika Kurzmann, Yaakov Kleeorin, Chuyao Tong, Rebekka Garreis, Angelika Knothe, Marius Eich, Christopher Mittag, Carolin Gold, Folkert Kor-

nelis de Vries, Kenji Watanabe, Takashi Taniguchi, Vladimir Fal'ko, Yigal Meir, Thomas Ihn, and Klaus Ensslin. Kondo effect and spin–orbit coupling in graphene quantum dots. *Nature Communications*, 12(1):6004, 2021.

[197] Samuel Möller, Luca Banszerus, Angelika Knothe, Corinne Steiner, Eike Icking, Stefan Trellenkamp, Florian Lentz, Kenji Watanabe, Takashi Taniguchi, Leonid I Glazman, et al. Probing two-electron multiplets in bilayer graphene quantum dots. *Physical Review Letters*, 127(25):256802, 2021.

[198] M. Korkusinski, W. Sheng, and P. Hawrylak. Designing quantum systems in self-assembled quantum dots. *Phys. Stat. Solidi (b)*, 238:246, 2003.